

Dissertation

Surface Acoustic Wave Magnetic Field Sensors for Biomagnetic Applications

submitted by **Viktor Schell**

in partial fulfillment of the requirements for the degree of Doctor of
Engineering (Dr.-Ing.)



Kiel University
December 2022

First Examiner: Prof. Dr.-Ing. Eckhard Quandt
Second Examiner: Prof. Dr. rer. nat. Franz Faupel

Date of Examination: 08.12.2022

Eidesstattliche Erklärung

Ich, Viktor Schell, versichere an Eides statt durch meine untenstehende, dass ich die vorstehende Arbeit selbständig und ohne unzulässige fremde Hilfe angefertigt und alle Stellen, die ich wörtlich oder dem Sinne nach aus Veröffentlichungen entnommen habe, als solche kenntlich gemacht habe und mich auch keiner anderen als der angegebenen Literatur oder sonstiger Hilfsmittel bedient habe.

Ich versichere an Eides statt, dass ich die vorgenannten Angaben nach bestem Wissen und Gewissen gemacht habe und dass die Angaben der Wahrheit entsprechen und ich nichts verschwiegen habe.

Die Strafbarkeit einer falschen eidesstattlichen Versicherung ist mir bekannt, namentlich die Strafandrohung gemäß § 156 StGB bis zu drei Jahren Freiheitsstrafe oder Geldstrafe bei vorsätzlicher Begehung der Tat bzw. gemäß § 163 Abs.1 StGB bis zu einem Jahr Freiheitsstrafe oder Geldstrafe bei fahrlässiger Begehung. Ich versichere, dass mir bisher kein akademischer Grad entzogen wurde. Weiterhin erkläre ich hiermit, dass diese Arbeit unter Einhaltung der Regeln guter wissenschaftlicher Praxis der Deutschen Forschungsgemeinschaft entstanden ist und die Doktorarbeit in dieser Form weder vollständig noch in Teilen in einem anderen Prüfungsverfahren bereits vorgelegen hat, veröffentlicht wurde oder zur Veröffentlichung eingereicht wurde.

Ort, Datum

Viktor Schell

Abstract

Biomagnetic signals, which are magnetic fields generated by the electric currents in the human body, have very low amplitudes at very low frequencies. In case of the human heart the signal components are in the range of $<1 \text{ pT}/\sqrt{\text{Hz}}$ to $30 \text{ pT}/\sqrt{\text{Hz}}$ at frequencies of 0.1 Hz to 100 Hz. These conditions make their detection a challenging task, while at the same time it is highly desirable for diagnosis in areas such as cardiography to be able to detect these signals in real time. Another medical application where the detection of magnetic fields of low amplitude is of high interest is the localization of implanted deep brain stimulation electrodes. While the amplitudes of the stimulation signals are one order of magnitude higher than the smallest signal components of the heart, it is beneficial to measure the harmonic signals in a rather large frequency bandwidth of 10 kHz to achieve a higher total signal amplitude.

Only few magnetic field sensors can match all these requirements. As for magnetostrictive film-based magnetic field sensors soft magnetic properties and high magnetostriction are required. Matching these requirements will lead to high sensitivities, but often high sensitivity comes at the cost of an increase of magnetically generated noise. Hence, finding a compromise between low noise and high sensitivity, or ideally maintaining high sensitivity while reducing noise, is a main task in magnetic film-based sensing to obtain a low limit of detection (LOD). One promising approach is using surface acoustic wave (SAW) devices which are coated with a magnetostrictive material. The magnetostrictive material will change its effective stiffness upon the application of a magnetic field inducing a change of magnetization. This phenomenon is called the ΔE effect. The change in stiffness causes a change of velocity of the acoustic wave, which is propagating through the magnetostrictive material. This velocity change results in a measurable phase change. The effect on the magnetic material is severely increased if the piezoelectric material which generates shear horizontal waves is coated with a guiding layer which confines the acoustic wave to the device's surface.

The deposition and characterization of the magnetostrictive alloy $(\text{Fe}_{90}\text{Co}_{10})_{78}\text{Si}_{12}\text{B}_{10}$ on quartz-based SAW sensors, as well as the fabrication of the SAW sensors is a main focus of this work. Since all piezoelectric materials have anisotropic thermal expansion coefficients, the deposition of soft magnetic materials bears to be a challenge, because the anisotropic expansion causes uniaxial strain acting on the film. The precise control of the magnetic anisotropy is a key parameter in achieving good LODs with the presented devices. With a single layer of FeCoSiB the LOD is as low as $70 \text{ pT}/\sqrt{\text{Hz}}$ at 10 Hz and $25 \text{ pT}/\sqrt{\text{Hz}}$ at 100 Hz. Additionally, it is shown that SAW sensors with DC magnetron sputtered FeCoSiB provide similar results in terms of sensor performance

compared to sensors with RF magnetron sputtered films under the same circumstances. Furthermore, the performance of the first AlScN thin film based SAW magnetic field sensors from cooperation partners from Fraunhofer ISIT was evaluated. Finally, top pinning exchange bias multilayers are applied to the quartz based sensors, which leads to a reduction of magnetically generated phase noise in the sensors and brings SAW magnetic field sensors closer towards biomagnetic field detection with LODs as low as $28 \text{ pT}/\sqrt{\text{Hz}}$ at 10 Hz and $10 \text{ pT}/\sqrt{\text{Hz}}$ at 100 Hz.

Zusammenfassung

Biomagnetische Signale, also Magnetfelder die durch die elektrischen Ströme im menschlichen Körper erzeugt werden, weisen geringe Amplituden bei niedrigen Frequenzen auf. Im Falle des menschlichen Herzens sind diese Amplituden im Bereich von unter $1 \text{ pT}/\sqrt{\text{Hz}}$ bis $30 \text{ pT}/\sqrt{\text{Hz}}$ bei Frequenzen von 0.1 Hz bis 100 Hz. Diese Voraussetzungen machen deren Detektion zu einer herausfordernden Aufgabe, obwohl es für Einsatzgebiete wie die Kardiografie höchst erstrebenswert ist diese Signale in Echtzeit zu messen. Eine weitere medizinische Anwendung bei der die Detektion von schwachen Magnetfeldern von Interesse ist, ist die Lokalisierung von implantierten Elektroden zur tiefen Hirnstimulation. Während die Amplituden der Anregungssignale bis zu einer Größenordnung über den kleinsten Signalkomponenten des Herzens liegen, ist es in diesem Fall von Vorteil die erzeugten harmonischen Signale bis zu einer Frequenz von 10 kHz zu erfassen, um die größtmögliche Signalamplitude zu erreichen.

Nur wenige Magnetfeldsensoren genügen diesen Ansprüchen. Bei Magnetfeldsensoren basierend auf magnetostriktiven Dünnschichten sind weichmagnetische Eigenschaften notwendig, bei gleichzeitig hoher Magnetostriktion. Das Erfüllen dieser Voraussetzungen führt zu hohen Sensitivitäten, allerdings generieren hohe Sensitivitäten häufig magnetisierungsinduziertes Rauschen. Daher ist das Finden eines Kompromisses zwischen geringem Rauschen und einer hohen Sensitivität, oder im Optimalfall eine Reduzierung des Rauschens bei gleichzeitiger Beibehaltung der Sensitivität, eine der Hauptaufgaben in der dünnfilmbasierten Magnetfeldsensorik. Ein vielversprechender Ansatz ist die Anwendung von Oberflächenwellenbauteilen (SAW, engl. surface acoustic wave), die mit einem magnetostriktiven Material beschichtet sind. Das magnetostriktive Material ändert bei einer magnetfeldinduzierten Änderung der Magnetisierung seine effektive Steifigkeit. Dieses Phänomen wird als ΔE -Effekt bezeichnet. Die Änderung der Steifigkeit führt zu einer Änderung der Geschwindigkeit der akustischen Welle, die sich durch den magnetostriktiven Film fortbewegt und daher zur einer messbaren Phasenänderung. Der Einfluss des magnetischen Materials wird stark erhöht, wenn das piezoelektrische Substrat, welches horizontale Scherwellen erzeugt, zuvor mit einer akustischen Führungsschicht beschichtet wurde, die die akustische Welle an deren Oberfläche und somit im magnetostriktiven Material lokalisiert.

Die Herstellung der SAW-Sensoren, sowie die Abscheidung und Charakterisierung der magnetostriktiven Legierung $(\text{Fe}_{90}\text{Co}_{10})_{78}\text{Si}_{12}\text{B}_{10}$ auf quarzbasierten SAW-Sensoren, sind ein Hauptaugenmerk dieser Arbeit. Da die thermische Ausdehnungskoeffizienten aller piezoelektrischer Materialien anisotrop sind, stellt die Abscheidung von weichmagnetischen Materialien eine Herausforderung dar, da die anisotrope Ausdehnung

eine uniaxiale Dehnung des Films hervorruft. Die genaue Kontrolle der magnetischen Anisotropie ist ein Schlüsselparameter im Erreichen eines guten Detektionslimits (LOD, engl. limit of detection) mit den zugrunde liegenden Sensoren. Mit einer Einzellage FeCoSiB beträgt das LOD $70 \text{ pT}/\sqrt{\text{Hz}}$ bei 10 Hz und $25 \text{ pT}/\sqrt{\text{Hz}}$ bei 100 Hz. Desweiteren wird gezeigt, dass SAW Sensoren mit FeCoSiB-Schichten die mittels DC Magnetron-sputtern abgeschieden wurden, vergleichbare Ergebnisse bezüglich Sensorperformance erreicht wie solche, die mit FeCoSiB beschichtet sind mittels RF Magnetron-sputtern, unter den gleichen Umständen. In Kooperation mit dem Fraunhofer ISIT, wird zudem die Performance der ersten AlScN dünn-schichtbasierten SAW Magnetfeldsensoren ausgewertet. Schließlich wurden sogenannte "top pinning" Exchange Bias Multilagen auf quarzbasierten Sensoren etabliert, welche zu einer Reduktion des magnetisch erzeugten Phasenrauschen in den Sensoren führt und SAW Magnetfeldsensoren näher in Richtung biomagnetischer Felddetektion bringt mit LODs von $28 \text{ pT}/\sqrt{\text{Hz}}$ bei 10 Hz und $10 \text{ pT}/\sqrt{\text{Hz}}$ bei 100 Hz.

Contents

1	Introduction	1
1.1	Motivation	2
1.2	SAW Principle and Devices	5
1.2.1	Love Wave SAWs	7
1.2.2	Design Considerations	8
1.3	Underlying Magnetic Phenomena	12
1.3.1	Magnetic Anisotropy	14
1.3.2	Magnetoelastic Coupling	16
1.3.3	Exchange Bias	18
1.4	SAW Sensing Mechanism and Noise	20
1.4.1	Sensitivity	20
1.4.2	Phase Noise and Limit of Detection	21
1.5	State-of-the-art Magnetic Field Sensors	24
1.5.1	Magnetometers for Biomagnetic Sensing	24
1.5.2	SAW Magnetic Field Sensors	29
2	SAW Sensor Fabrication	33
2.1	IDTs	34
2.2	Guiding Layer	37
2.3	Magnetostrictive Film	42
3	Publications	49
3.1	Magnetic Anisotropy Controlled FeCoSiB Thin Films	50
3.2	Sputter Deposited Magnetostrictive Layers	56
3.3	Thin-Film-Based SAW Magnetic Field Sensors	74
3.4	Exchange Biased SAW Magnetic Field Sensors	83

4 Summary and Outlook	99
4.1 Summary	100
4.2 Outlook	103
Full List of Publications	107
Bibliography	111
Acknowledgments	125

Introduction

This chapter lays the groundwork for the results presented in this thesis. In the first section a motivation is given on why the detection of biomagnetic signals is relevant for a society, while also providing a historical context on the monitoring of bodily functions. Herein, also the challenges which accompany the task of sensing magnetic fields of human origin are discussed. On this basis, arguments will be pointed out on why SAW sensors specifically are potentially promising to approach this challenge. In the following sections the theoretical background of this work is provided. First, a general explanation of the SAW principle and an outline of the varieties of SAW designs and mechanisms are offered as well as an introduction to the SAW sensor used in this work. Then, a section is dedicated to the basic principles of magnetism and magnetic materials relevant for understanding the underlying mechanisms and effects in SAW magnetic field sensors. Subsequently, the principle of magnetic field sensing with SAW delay line devices will be explained, as well as the phase noise occurring in these devices. Finally, a broad overview of competing magnetic sensing mechanisms is given and the SAW magnetic field sensor is ranked within these different approaches.

1.1 Motivation

For most of their existence humans had very little knowledge about the relation between basic functions of their body and electromagnetic signals. In 18th century France, for example, it was even considered that magnetism, as proclaimed by cult leader Dr. Franz Mesmer, could heal diseases [Coh75a]. The term *mesmerized* survived until today. It needed people like the Italian physician Luigi Galvani and Italian physicist Carlo Matteucci to shed a little light on the dark. Galvani discovered that the muscle movement and contraction in frogs is somehow related to electrical currents within the muscles and later Matteucci was able to observe and measure this same phenomenon in a frog's heart [Mat42, AL12]. These early discoveries and many others since Matteucci's work lead to the invention of the first electrocardiograph in the beginning of the 20th century, which is one of the most common and essential diagnostics tools in cardiology to this day [Fye94]. While electrocardiography (ECG) provides valuable information about the cardiovascular system and unarguably contributed immensely to the increase in life expectancy around the world, it still comes with some limitations. The main one is the need for permanent attachment to the body through electrodes. This requirement makes it difficult to conduct long term studies on patients, as wearing these electrodes creates an unnatural environment for the patient and hence might affect the outcome of the study. Although approaches for measuring ECGs with capacitive electrodes have been demonstrated [LKP07] the lack of flexibility is still prevailing. Additionally, permanent monitoring of patients at risk of cardiac arrest or those suffering from arrhythmia is not possible. It was found that before heart failure in about 30 % of cases a so-called prolongation of the QRS complex occurs. The QRS complex is a characteristic sequence of waves which appear in the time domain of a cardiogram. The prolongation of the QRS complex could be diagnosed in an early stage through the long term monitoring of the patients heart function and hence prevent the failure through appropriate treatment [KB05, BCM⁺07]. Another major limitation is the spatial resolution of ECG since the currents can only be measured along certain directions because of the anisotropy in the conductive paths in the body and the current amplitudes depend on the resistivity of the tissue they flow through. Given these limitations, alterations and even falsification of the obtained signals from the inverse problem modeling can occur [ND02].

As per Ampère's circuital law all electric currents create a magnetic field and so do the currents in the human body. Therefore, to overcome the limitations of ECG the measurement of the magnetic fields instead of the currents was suggested. For the

first time such measurements were performed by Baule and McFee [BM63] and Cohen [Coh67]. They both used rather large pick up coils with up to a million windings, thus no spatial distributions could be obtained from those, as the sensors in this case are larger than the heart itself. Additionally, the detection limit of these coils was still not sufficient enough and the obtained signals were noisy and therefore not suitable for diagnosis. At the same time the first superconducting quantum interference devices (SQUIDs) were introduced to the market, which are still the most sensitive magnetometers with a noise level of only a few $\text{fT}/\sqrt{\text{Hz}}$ [SB06]. As for the insufficient performance of pick up coils Cohen switched to the superior SQUID magnetometers to measure heart and brain signals and consequently paved the way for magnetocardiography (MCG) and magnetoencephalography (MEG) as it is known today [Coh75b]. For MCG and MEG no direct contact to the body is necessary. Additionally, the human body is transparent to magnetic fields, hence the magnetic fields are independent from the conductivity of different body tissues such as skull, bones and body fat. However, the field strengths of biomagnetic signals are in the range of 10^{-11} Tesla to 10^{-14} Tesla at frequencies far below 1 kHz and therefore several orders of magnitude below the earth's static magnetic field [KLPY13]. Current state-of-the-art sensors for biomagnetic diagnosis such as SQUIDs can only detect such small signals if they are operated in a magnetically shielded environment, which limits their wide spread use. Besides the naturally occurring biomagnetic signals there are also electric signals in the body which are generated artificially. For example, such artificial signals are generated by deep brain stimulation (DBS) electrodes implanted into patient's brains which suffer from neurological diseases including tremors through Parkinson's disease, dystonia or Tourette's syndrom. The DBS electrodes stimulate regions in the brain such as the subthalamic nucleus by periodic electrical pulses and through these stimulations the patients' symptoms are reduced or even disappear [DSBK⁺06, KK07]. The electrical pulses of commercial DBS systems are characteristic square signals with pulse widths of up to $100 \mu\text{s}$ [YTM⁺20]. They exhibit a typical fundamental frequency of 130 Hz (or similar depending on the patient, but not higher than 160 Hz) but also contain a multitude of harmonics of 130 Hz in the range of up to 10 kHz. The precise localization of the activated brain volume and rotational orientation detection of the implanted DBS electrodes is of high diagnostic value. Until now a typical localization procedure consists of magnetic resonance imaging (MRI) performed before the implantation and computer tomography (CT) after the implantation [YSM⁺21]. However, these procedures are time and cost intensive, require harmful contrast agents and are often not accurate (enough) [ETA18]. Additionally, the localization and rotation detection through CT is always a postoperative observation, but it would be much more bene-

ficial for surgeons and patients to do this during the surgical intervention to allow for immediate corrective procedures and constant monitoring. Hence, there is a demand for magnetometers which are able to detect the small amplitudes and as much of the harmonics over the range of 10 kHz as possible.

Magnetic field sensors which potentially can combine the demands of magneto-cardiography and deep brain stimulation in terms of required noise level and especially frequency bandwidth are surface acoustic wave (SAW) magnetic field sensors. In preceding work Kittmann et al. [KDZ⁺18] adapted a SAW concept well known from biosensing [SGT⁺04] and applied it to magnetic field sensing by the implementation of the magnetoelastic alloy FeCoSiB in these sensors. It was demonstrated that the combination of a Love wave sensor with a magnetoelastic material yields a sensor which is very sensitive to slowly varying magnetic fields and provides a low noise level at the same time. While this first work already provided promising results in terms of limit of detection, frequency bandwidth and dynamic range, this approach also opened the door for a multitude of new questions and ways to improve the performance of these sensors. Consequently, this work presents ways on how magnetic films should be deposited to achieve high performing sensors. Another main focus of this work is the implementation of magnetic multilayers incorporating the exchange bias effect to further reduce the magnetically generated noise in these sensors and consequently lower the limit of detection of those further towards biomagnetic signals, as it has been done on silicon based sensors [RYU⁺15].

The results of this work were all obtained within the collaborative research center (CRC) 1261, which is a combined research project of different disciplines, such as materials science (Institute for Materials Science at Kiel University, Fraunhofer ISIT in Itzehoe), electrical engineering (Institute of Electrical and Information Engineering at Kiel University) and medicine (University Hospital Schleswig-Holstein UKSH) with the common goal to develop low noise magnetoelectric and magnetoelastic magnetic fields sensors and establish them for a multitude of medical and biomedical applications and diagnostics tools.

1.2 SAW Principle and Devices

Acoustic waves are elastic waves and in contrast to electromagnetic waves they require a medium to propagate. In general, they can be distinguished into two types of waves, depending on the way they propagate through the medium. Longitudinal waves create displacements parallel to their propagation direction, while transverse waves, also called shear waves, propagate with displacements perpendicular to their propagation direction. Both types of waves are illustrated in Figure 1.1. The general velocity ν with which acoustic waves propagate depends on the mechanical properties of the medium i.e. its stiffness and its density ρ as given by

$$\nu = \sqrt{\frac{c_{ij}}{\rho}} \quad (1.1)$$

where c_{ij} is a stiffness constant and depends on the axis along which the displacement from the acoustic wave takes place [Has00, p. 1 ff.].

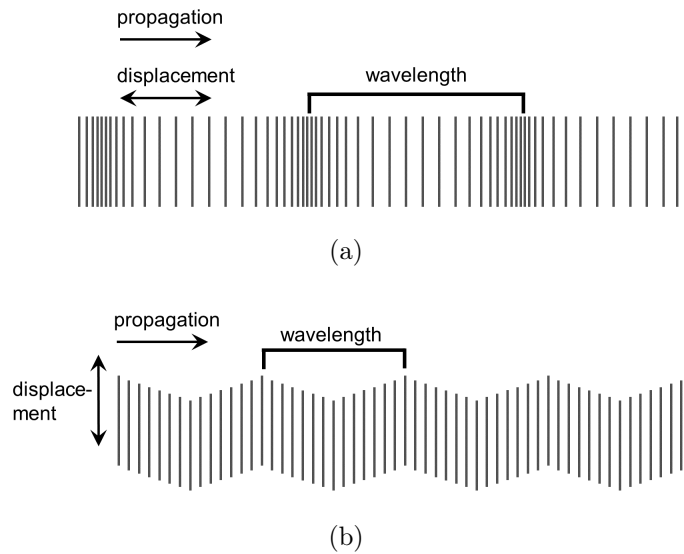


Figure 1.1: Two types of acoustic waves. (a) Longitudinal and (b) transverse waves. Adapted from [Kin87, p. 2].

Acoustic waves can also exist predominantly at the surface of the solid material. These surface acoustic waves (SAW) were first mathematically described by Rayleigh in 1885 [Ray85]. He described seismic waves with out-of-plane shear displacements, which later were named after him as Rayleigh waves. Later Love described a similar phenomenon with in-plane shear displacement observed inside layered structures [Mor07, p. 3]. These waves were later named Love waves. The difference between Rayleigh and Love waves is illustrated in Figure 1.2.

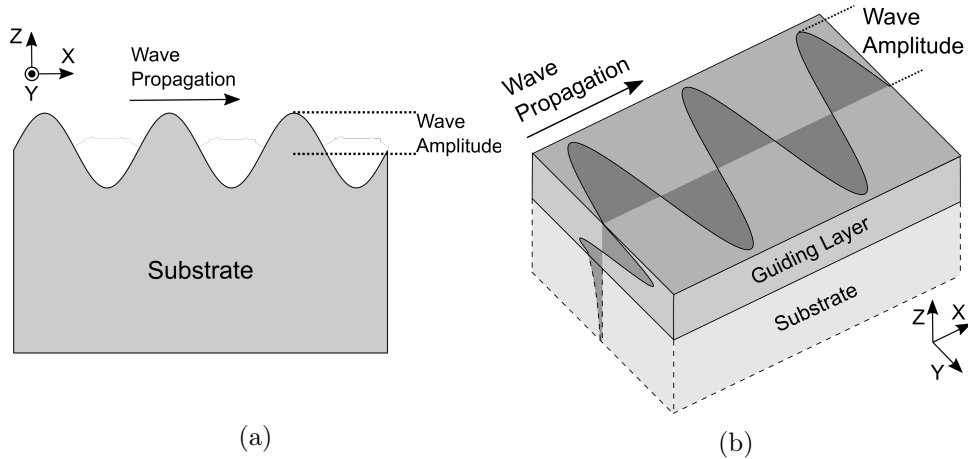


Figure 1.2: Two types of surface acoustic waves. (a) Rayleigh wave and (b) Love wave. Adapted from [RD99, p. 267 ff.].

Through the invention of interdigital transducers (IDTs) it was possible to utilize SAWs technologically, as they could be generated on piezoelectric substrates by the IDTs [WV65]. Since then SAW devices found their way into science and industry as SAW sensors, SAW filters and delay lines [Cam89, p. 407 ff.]. In this approach, SAWs are excited by applying a high frequency voltage to IDTs which have been deposited onto a piezoelectric substrate. Utilizing the inverse piezoelectric effect the electric energy is transformed into mechanical energy in form of a high frequency surface acoustic wave. If a second pair of IDTs are placed within a defined distance from the input IDTs, the acoustic wave can be picked up again through the direct piezoelectric effect. This setup is called a delay line, since acoustic waves are slower than electromagnetic waves and the input signal gets delayed by a delay time τ_d , which is determined by

$$\tau_d = \frac{L}{\nu_p} \quad (1.2)$$

where L is the center-to-center transducer distance and ν_p the phase velocity of the acoustic wave [FMM95, p. 142]. The phase velocity depends on the mechanical properties of the used substrate and its orientation as shown in Equation 1.1. The acoustic wave can also be picked-up by the same IDTs if grating-like reflectors are placed along the propagation path. As piezoelectric substrates are highly anisotropic the orientation of the IDTs with respect to the crystallographic orientation of the substrate not only determines the velocity of the wave but also the type of wave which is generated. For example on ST-cut quartz, which is a rotated quartz where the crystallographic Y-axis is rotated by 42.75° with respect to the surface normal (see Figure 1 in section 3.1) Rayleigh as well as Love waves can be excited. If the IDTs are orientated in a way

that the propagation direction is parallel to the crystallographic X-axis Rayleigh waves are excited [FMM95, p. 141]. If the IDT orientation is chosen to be 90° with regard to the crystallographic X-axis Love waves are excited if using an appropriate guiding layer [RJAA13].

1.2.1 Love Wave SAWs

Love waves can only be excited if a substrate is used that allows for shear horizontal waves to propagate. A selection of substrates suitable for Love wave generation is given in Table 1.1 combined with their respective electromechanical coupling coefficients K^2 , which quantifies how much of the electrical input energy is transformed into mechanical energy. The higher this value is, the lower the insertion loss of the SAW device will be. However, another important parameter is also given in Table 1.1 which is the linear temperature coefficient of frequency (TCF). It describes how much the center frequency of the SAW device will change with temperature.

As piezoelectric substrates are anisotropic with regard to most of their properties, they need specific crystallographic orientations to provide specific properties. This is also the case for the generation of surface acoustic waves and specifically for shear horizontal waves. The orientation of the single crystal substrates in the field of SAW devices is denoted by the axes X,Y and Z in which Z is e.g. the c-axis of a trigonal crystal such as quartz [Bot82, p. 14 ff.]. By rotating the crystallographic orientation of the piezoelectric substrate with respect to its surface normal and consequently the propagation direction of the SAW, different surface acoustic waves and phase velocities can be generated [Has00, p. 184 f.]. Hence, the rotation angle around the specific axis and the propagation direction are denoted in the name of the substrate as well. For example, 36° YX LiTaO₃ means that the Y axis of the LiTaO₃ single crystal is tilted by 36° with respect to the surface normal and the wave propagation direction is along the X axis.

Table 1.1: A selection of common substrates used for Love wave devices and their properties. From [RJAA13].

Substrate	Prop. direction	ν_p [m/s]	ρ [kg/m ³]	K^2 [%]	TCF [ppm/°C]
ST-cut quartz	90° X	5050	2650	1.9	40
AT-cut quartz	90° X	5099	2650	1.4	0 to 1
36° Y-cut LiNbO ₃	X	4800	4628	16	-75 to -80
36° Y-cut LiTaO ₃	X	4200	7454	5	-35 to -45

Love waves only propagate in an additional layer on top of the piezoelectric substrate. A prerequisite for this is that the phase velocity of the acoustic wave in the

additional layer is lower than in the substrate. This way the acoustic wave will only propagate on the surface of the additional layer as it is reflected from the interface of the two media. In fact, the higher the difference in phase velocity between the two layers is the more will the wave be focused to the surface of the additional layer. Hence, this layer has been termed guiding layer. A list of some materials which have been used in Love wave devices is given in Table 1.2. Also listed are the materials' shear modulus G_L , density ρ_L and the from Equation 1.1 resulting phase velocity of the guiding layer ν_L .

Table 1.2: A selection of common guiding layer materials used for Love wave devices and their properties. From [RJAA13].

Guiding Layer Material	G_L [GPa]	ρ_L [kg/m ³]	ν_L [m/s]
SiO ₂	17.9	2200	2850
ZnO	40.2	5720	2650
Polyimide	0.87	1420	781
PDMS	$250 \cdot 10^{-6}$	965	16
PMMA	1.7	1180	1200

The most common and established guiding layer material is amorphous silicon dioxide (SiO₂) [JV97, KVH⁺94, WXC⁺15]. It can be grown with quite high deposition rates by plasma enhanced chemical vapor deposition (see Section 2.2) and the phase velocity is nearly half of quartz, providing a good confinement of the acoustic wave on the guiding layers surface. Judging by the difference of phase velocity only polymers seem to be better suited to serve as a guiding layer, as the velocities are sufficiently smaller than in piezoelectric substrates. However, it was shown with e.g. PMMA that the insertion losses drastically increase with increasing polymer thickness, although providing higher sensitivities than SiO₂ [HD97]. Since polymers are typically deposited by spin coating the surface roughness is potentially too high for the deposition of soft magnetic materials. Based on these arguments (SiO₂) is also used as the guiding layer in this work.

1.2.2 Design Considerations

Many of the parameters of SAW devices such as operation frequency, insertion loss or even sensitivity can be controlled through their structural design. For SAW filters a well defined frequency bandpass is desired, in SAW sensors the frequency response is not as important as sensitivity. Most of these characteristics such as frequency and insertion loss are determined by the IDTs. The synchronous frequency f_0 of a delay

line SAW sensor is given by

$$f_0 = \frac{v_p}{\lambda} \quad (1.3)$$

in which λ is the wave length of the excited acoustic wave. The wavelength, on the other hand, is determined by the IDT pitch which is the distance between two fingers (pairs) of same polarity as shown in Figure 1.3. In case of Love waves one additionally has to consider that the phase velocity is not simply determined by the substrate, but by the combination of guiding layer and substrate and in case of SAW magnetic field sensors also the magnetoelastic film [MDH⁺22]. The thicker the guiding layer becomes the slower the Love wave and the lower the frequency will be [RJAA13]. The

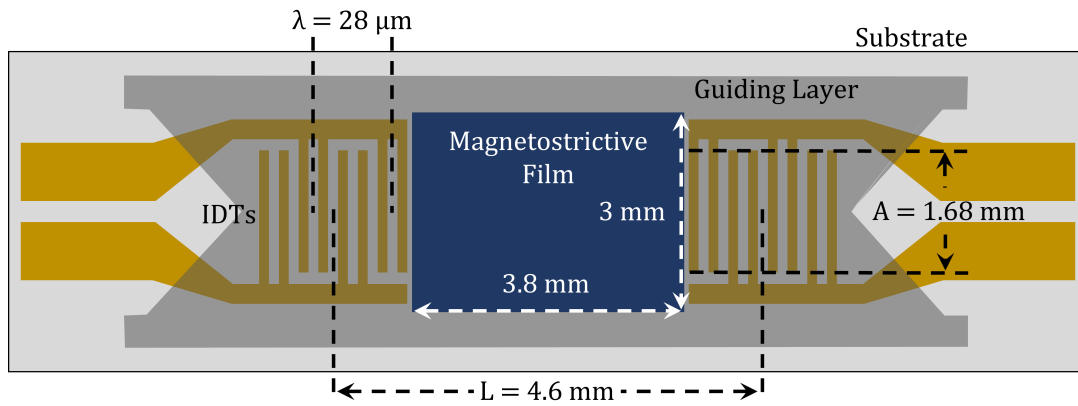


Figure 1.3: Schematic of the SAW Love wave device used in this work. λ is the wavelength of the generated acoustic wave given by the IDT pitch, A is the acoustic aperture, which determines the width of acoustic wave front and L is the center-to-center distance of the IDTs. The number of double finger pairs is $N = 25$. The edges of the guiding layer have angles of 120° to reflect back scattered waves away from the delay line.

number of finger pairs N determines the excitation frequency bandwidth of the SAW device. In general, the larger the number of finger pairs the narrower the frequency response will be, as more destructive interference of non-synchronous waves occurs if more waves are generated. However, owing to more waves being involved in the constructive interference at the synchronous frequency, the insertion losses will be lower the larger N is [Cam89, p. 40 f.]. The influence on the bandwidth is illustrated in Figure 1.4a in which the insertion losses (transmission) are normalized. This work's SAW device consists of 25 double finger pairs and the correlated frequency response of such a Love wave device is shown in Figure 1.4b. It shows the transmission coefficients S_{21} and S_{12} . Due to the double finger structure the reflected waves from the IDTs do not add up in phase as they are shifted by $\pi/4$ causing constructive interference of the incoming SAW waves with reflected waves [Mor07].

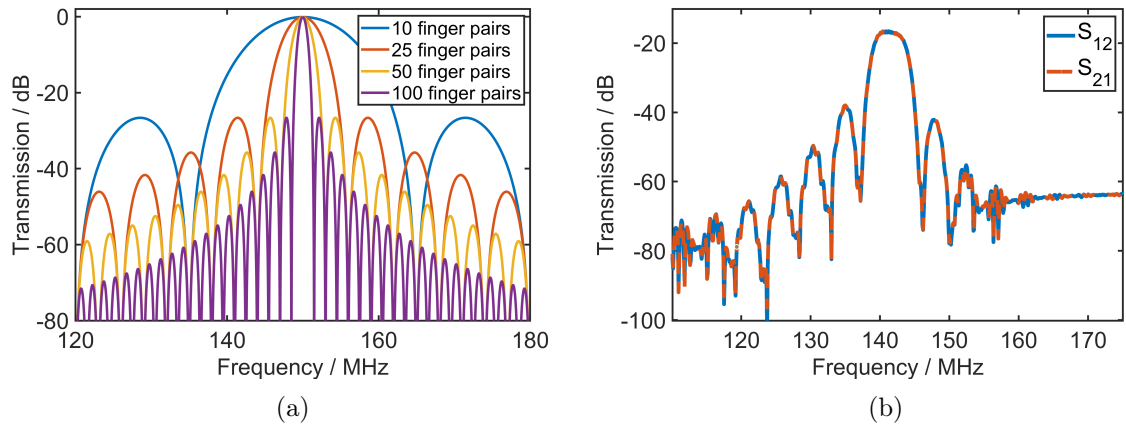


Figure 1.4: Frequency responses. (a) Normalized frequency response for different numbers of finger pairs. As the number of finger pairs increases the bandwidth becomes narrower. Insertion losses are not included. Calculated after [Cam89, p. 40 f.]. (b) Measured scattering parameters S_{21} and S_{12} of a SAW Love wave device with 25 double finger pairs IDTs.

The acoustic aperture A gives the width of the wavefront of the acoustic wave which is determined by the overlap of the IDT finger pairs. Only when the IDTs of opposite polarity overlap acoustic waves are excited. It should be chosen to be several multiples of the wavelength, because diffraction of the wave can occur if the aperture is too narrow [Has00, p. 103]. If aperture and wavelength are on the same order of magnitude the IDTs can act as a point source and excite waves with curved wavefronts. All the characteristic dimensions of the fabricated IDTs are listed in Table 1.3.

Table 1.3: Characteristic dimensions and parameters of the IDTs used in this work.

Parameter	Value	Unit
Material	Cr/Au/Cr	
Thickness	8/200-300/8	nm
Finger pairs	25	
Number of double fingers	50	
Total number of fingers	100	
Finger width	3.5	μm
Finger distance	3.5	μm
Pitch	28	μm
Acoustic aperture	1.68	mm
Delay line length	4.62	mm

Acoustic waves generated by IDTs travel in both directions of the IDT, not only into the sensing area direction. To prevent that these waves are reflected back into the sensing area from the sensors edges, the edges of the guiding layer are structured with

an angle along the propagation axis (see Figure 1.3). This way all waves coming in along this direction are reflected away from the sensing area arbitrarily. Waves reflected from the output IDTs are scattered the same way at these edges.

The magnetostrictive delay line is structured on top of the guiding layer. It is not overlapping with the IDTs, as it was shown that covering the IDTs with a metallic film (with the guiding layer in-between) leads to capacitive electromagnetic cross-talk, which reduces the sensor performance [Sch03, p. 95 f.]. The width of the magnetic film was chosen to be larger than the acoustic aperture of the wave to prevent additional interactions of the wave with edges parallel to the propagation direction.

1.3 Underlying Magnetic Phenomena

The magnetism of materials is determined by the rotational motion of their electrons. Electrons perform two rotations, an orbital movement around the nucleus and a rotation around their own axis, termed the spin of the electron. As a consequence of the orbital angular momentum and the spin momentum electrons possess a net magnetic moment. In ferromagnetic materials a spontaneous magnetization is present, which means that via their exchange interaction the magnetic moments are aligned along the same direction. The requirement for spontaneous magnetization are half-filled orbitals, such that only spins with one polarization direction exist. The spontaneous magnetization along one direction only exists in specific regions in the materials. These regions of same polarization are called domains. Domains of different polarizations are separated by domain walls, in which the magnetization rotates from one direction into the other. Upon the application of an external magnetic field the orientation of the domains changes, as they align along the magnetic field as a means of energy minimization. This alignment of magnetization along the direction of an applied magnetic field or any directional force acting on the magnetization opens up a broad field of potential technological applications. Some of them are magnetic sensing, magnetic recording, loudspeaker magnets or cores of transformers and motors [CG09, p. 439, p. 477, p. 505].

The properties of the ferromagnetic material are one of the most influential factors in SAW magnetic field sensors. For high sensitivities large magnetostriction is necessary. Additionally, the magnetic film should have a low total anisotropy energy, while the anisotropy should be still uniaxial. Moreover, magnetic domains, domain walls and their dynamic behaviour play a significant role in SAW magnetic field sensors, as they are the origin of loss-associated phase noise induced by various domain wall mechanisms [Ber98, p. 411 ff.]. To minimize this phase noise the magnetic film should, ideally, consist of a single domain. In case of a single domain state, the remagnetization process is governed by a magnetization rotation only and not by domain wall movement, which is a well known origin of noise [Ber98]. The driving force for the formation of domains is the minimization of the total free energy E_{tot} which is comprised of several energy contributions along several energy terms which sum up to

$$E_{\text{tot}} = E_{\text{ex}} + E_{\text{aniso}} + E_{\text{d}} + E_{\text{ze}} + E_{\sigma} + E_{\text{ms}} \quad (1.4)$$

where E_{ex} is the exchange energy, E_{aniso} the anisotropy energy, E_{d} the demagnetization energy, E_{ze} the Zeeman or external field energy, E_{σ} the stress energy and E_{ms} the magnetostriction energy [Coe10, p. 234]. The exchange energy describes the interaction

of the magnetic moments of a particular material. E_{ex} additionally contributes to the total free energy in case of two materials being coupled at an interface. If these two materials show different spin structures such as a ferromagnet and an antiferromagnet an exchange bias is invoked between the layers, which will be discussed in more detail in Section 1.3.3. The formation of domains and domain walls is illustrated in Figure 1.5. The single domain state as shown in Figure 1.5a creates a large stray field H_{stray} and requires additional energy which is larger than E_{d} to uphold this state. In this case the magnetic anisotropy is unidirectional, since the complete specimen is already magnetized into the direction of spontaneous magnetization M . By introducing a domain wall which rotates the magnetization by 180° between two domains, H_{stray} and hence E_{d} are reduced as shown in Figure 1.5b. The axis along which M is orientated is the easy axis of magnetization. In Figure 1.5c the domains are separated by 90° domain walls, which means that the magnetization rotates by 90° inside the domain wall. Stray fields do not form, since all magnetic poles are compensated by a directly adjacent opposite pole. However, the anisotropy is isotropic, or in this specific case slightly anisotropic due to the shape of the specimen.

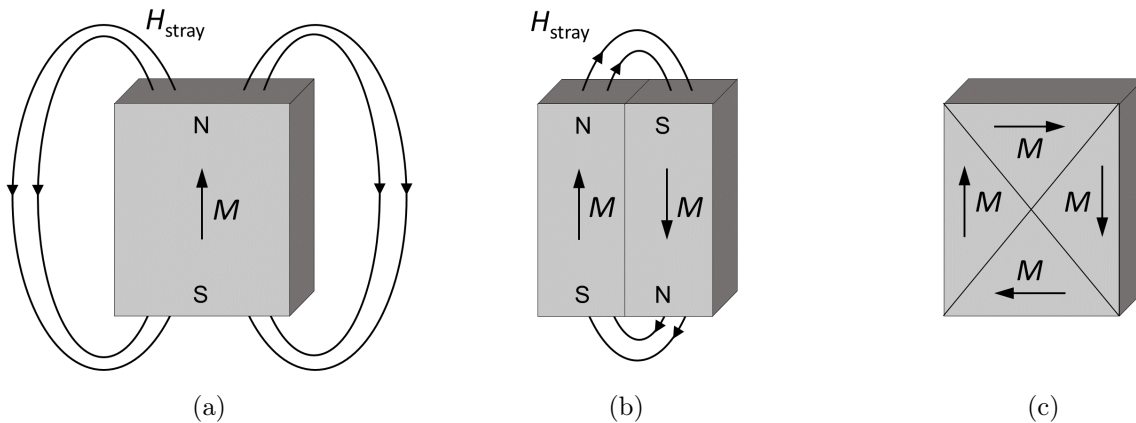


Figure 1.5: Formation of domain walls as a means to reduce stray field energy. (a) A single domain with a large stray field H_{stray} . The anisotropy is unidirectional. (b) Two domains separated by a 180° domain wall, which reduces H_{stray} . The magnetic easy axis is along the two spontaneous magnetization directions M . (c) Complete flux closure by the formation of 90° domain walls. In this case the anisotropy is determined by the shape (excluding all other contributions). Partially adapted from [CG09, p. 293].

Relevant contributions to the anisotropy energy of amorphous materials will be discussed in Section 1.3.1 and the contributions to the total free energy through stress and magnetostriction are summarized in Section 1.3.2. In the following the different anisotropy contributions are discussed individually.

1.3.1 Magnetic Anisotropy

In general, contributions to magnetic anisotropy can be distinguished between shape anisotropy, magnetocrystalline anisotropy, stress anisotropy and induced anisotropy, the exchange bias discussed in Section 1.3.3 being an additional type of magnetic anisotropy. Anisotropy in this context means that the magnetic material can be magnetized easier in certain geometric directions than in others. As a consequence of one or more of the mentioned contributions an easy and a hard axis of magnetization forms. The ratio of the easy and hard axis of magnetization is quantified through the anisotropy constant K_u .

Shape Anisotropy As the name suggests the shape of the material determines the hard and easy axis of magnetization. In a sphere all dimensions are equal hence no shape anisotropy exists. As soon as the ratio of dimensions changes the directions of preferred magnetization become anisotropic. The reason for shape anisotropy lies in the demagnetization field H_d induced by poles forming within the shape of the material given by

$$H_d = -\vec{N}_d M \quad (1.5)$$

with \vec{N}_d as the demagnetization factor and the result of the demagnetization along all directions of a specimen and depends on the shape of the material and M the magnetization [CG09, p. 53]. Hence the shape anisotropy is determined by the ratio of the different dimensions of a specimen as long as the magnetization is constant.

Magnetocrystalline Anisotropy The crystal structure of a material will cause magnetic anisotropy, since along certain crystallographic directions magnetization is preferred. Therefore, the anisotropy coefficients are given by the crystal structure, e.g. whether the material grows in a cubic or hexagonal structure and is constant for a given material and temperature [CG09, p. 201]. In crystalline materials this anisotropy is dominant, but in amorphous ferromagnetic materials it is neglectable, since they possess only a short range order. Therefore, the exchange interaction of magnetic moments is not inherited by a long range order as it is in crystalline materials.

Stress Anisotropy Stress σ acting on a positive magnetostrictive material induces additional anisotropy and aligns the magnetization axes along the directions of the external strain. Figure 1.6 illustrates that the alignment of anisotropy depends on the direction of the strain. With increasing tensile strain the anisotropy aligns with the strain axis. An additional magnetic field parallel to the strain axis will then saturate the film in the direction of the field. Applying compressive strain will align the

easy axis of magnetization perpendicular to the strain axis. Applying a magnetic field parallel to the strain axis will rotate the magnetization towards the field direction, if the anisotropy induced by the magnetic field is larger than the strain anisotropy.

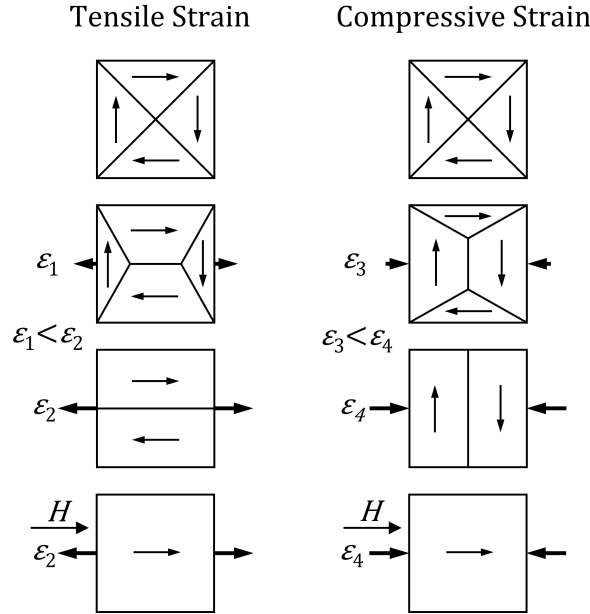


Figure 1.6: Schematic of the magnetization of a material with positive magnetostriction under tensile strain on the left and compressive strain on the right. With tensile strain a weak magnetic field H along the same axis will magnetically saturate the material. With compressive strain the energy from H needs to be larger than the energy from the strain to magnetize the material along the field direction/strain axis. Adapted from Cullity and Graham [CG09, p. 263 ff.].

Stress anisotropy is a consequence of Joule magnetostriction. Magnetostriction describes the ability of ferromagnetic materials to change their dimensions upon a change in magnetization. The process described in Figure 1.6 is a result of inverse magnetostriction as the magnetization changes upon the application of strain. The relation between isotropic magnetostriction, stress and the stress induced anisotropy K_σ is given by

$$K_u = K_\sigma = \frac{3}{2} \lambda_s \sigma \quad (1.6)$$

with λ_s being the isotropic saturation magnetostriction and σ the acting stress in the sample [CG09, p. 264]. In this work the magnetic material is deposited on piezoelectric quartz. Quartz exhibits anisotropic thermal expansion coefficients and will also induce stress and consequently stress induced anisotropy in the magnetic thin film if temperature is applied. This additional anisotropy in FeCoSiB was studied in Section 3.1.

Induced Anisotropy In some materials anisotropy cannot only be induced by aligning the magnetisation via stress but also by applying a magnetic field. This anisotropy can be preserved in the material if an additional temperature below the material's Curie temperature is applied to the sample inside the magnetic field and then cooled to room temperature [CG09, p. 336 f.]. Likewise, anisotropy can be induced by applying the magnetic field during the growth of the film, for example during magnetron sputtering [SSB91]. The induced anisotropy through annealing or magnetic field deposition can be estimated by

$$K_u = \frac{1}{2} H_k \mu_0 M_s \quad (1.7)$$

with the anisotropy field H_k , and saturation magnetization M_s [Coe10, p. 171]. The anisotropy field describes the field difference between the easy and hard axis of magnetization. For amorphous magnetostrictive materials it is essential to induce an uniaxial anisotropy to achieve maximum magnetostriction [LQ00]. The influence of the induced anisotropy on the performance of SAW sensors is discussed in Section 3.1.

1.3.2 Magnetoelastic Coupling

The mechanical and magnetic properties of a material are correlated by magnetostriction. The relation between stress and strain, which influence the mechanical properties and magnetization is termed magnetoelastic coupling. The direct coupling of stress and magnetization is termed ΔE effect. ΔE , since the Young's modulus or elastic modulus E changes with a change in magnetization through the generation of additional magnetostrictive stress [Coe10, p. 178]. The change of Young's modulus of a positive magnetostrictive material can be estimated by

$$\frac{\Delta E}{E_s} = \frac{E(H) - E_s}{E_s} = \frac{9\lambda_s^2 E(H) H^2}{M_s H_{k,\sigma}^3} \quad (1.8)$$

where $E(H)$ is the Young's modulus at a constant magnetic field, E_s the Young's modulus in saturation, H the applied magnetic field and $H_{k,\sigma}$ the reduced anisotropy field by the additional stress [Liv82] given by:

$$H_{k,\sigma} = \frac{K_u - K_\sigma}{M_s} \quad (1.9)$$

Therefore, to achieve a large ΔE effect a high magnetostriction λ_s and a small but defined and unidirectional anisotropy are necessary.

In SAW magnetic field sensors a phase change is induced by magnetomechanical

coupling through the ΔE effect. The manner in which the Young's modulus changes as a function of an applied DC magnetic field depends on the anisotropy of the magnetoelastic film, the magnetic field direction and the type of stress generated by the acoustic wave. Therefore, depending on all these contributions $H_{k,\sigma}$ in Equation 1.8 will change accordingly, which significantly determines ΔE . Different types of waves generate different stresses depending on their displacement axis. In the film plane, Rayleigh waves generate a tensile stress, while Love waves cause shear stress (more on different wave types in Section 1.2). Figure 1.7 shows measurements of three different sensors using either Love waves in 1.7a and 1.7b or Rayleigh waves in 1.7c. In the Love wave sen-

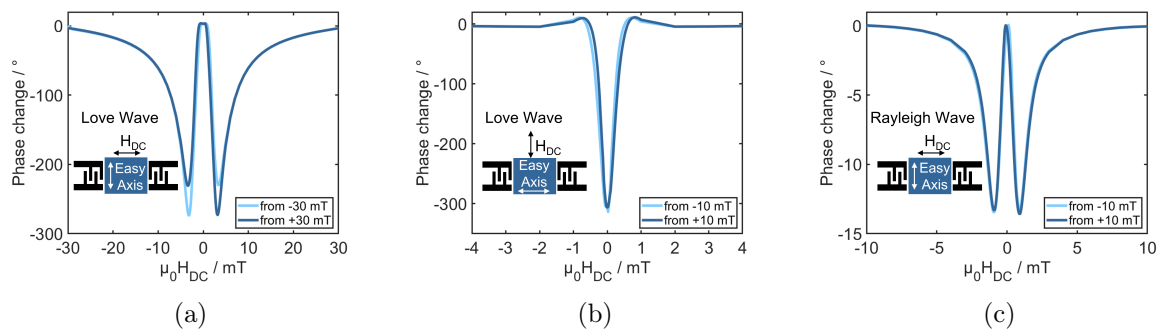


Figure 1.7: Phase response as a function of applied DC bias field for different SAW sensors. (a) A sensor on a 64° Y-cut LiNbO_3 substrate exhibiting Love waves with a $4.5 \mu\text{m}$ SiO_2 guiding layer and 200 nm FeCoSiB . The easy axis of magnetization was induced perpendicular to the SAW propagation direction. (b) A sensor on a ST-cut quartz substrate with a $4.5 \mu\text{m}$ SiO_2 guiding layer and 200 nm FeCoSiB . In this case Love waves are excited 90° to the crystallographic X-axis. The easy axis of magnetization was induced parallel to the SAW propagation direction. (c) A sensor on a ST-cut quartz substrate with 200 nm FeCoSiB . In this case Rayleigh waves are excited along the X-axis. The easy axis of magnetization was induced perpendicular to the SAW propagation direction. In all three cases the measurement field was applied perpendicular to the easy axis. The insets show the orientations of anisotropy and applied fields with respect to the IDT orientation.

sors also different anisotropy configurations were set during film growth. In 1.7a the easy axis of magnetization is perpendicular to the SAW propagation direction and in 1.7b parallel to the SAW propagation direction. The phase change of the Love wave devices under shear strain follows the characteristic change of shear modulus or stiffness coefficient C_{66} as theoretically predicted by Zabel [Zab19, p. 17] and Mazzamurro et al. [MDP⁺20]. The phase change in the Rayleigh wave device follows the change of the stiffness coefficients C_{11} or C_{22} according to the calculations of Mazzamurro et al. [MDP⁺20]. Squire demonstrated that the change in shear modulus is higher than the change in Young's modulus in magnetostrictive wires [SAA95]. Additionally, the

required DC bias field at which the slope of the curves is maximum i.e., the point of highest sensitivity is different for each configuration.

1.3.3 Exchange Bias

A different type of magnetic anisotropy is the so-called exchange bias which unidirectional [MB56]. Forming an interface with materials which exhibit some kind of spontaneous magnetization leads to exchange coupling between these two materials. The coupling of a ferromagnetic material with an antiferromagnetic material creates a magnetization bias in the ferromagnetic material, in which the magnetic moments are aligned along the same direction as the magnetic moments of the antiferromagnet at the interface. Moreover, the antiferromagnet's magnetic moments can be aligned by the ferromagnet. Biasing a ferromagnetic material in such a manner induces an unidirectional anisotropy. It is called exchange bias, as the ferromagnet is biased via exchange coupling [NS99, BT99]. Since in the remanent state of such an exchange biased system all magnetic moments are aligned in one direction the hysteresis loop is shifted on the magnetic field axis against the exchange bias field H_{EB} as illustrated in Figure 1.8.

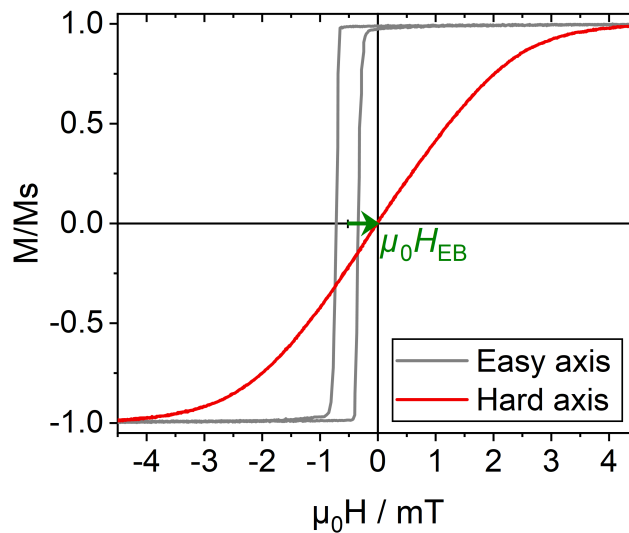


Figure 1.8: Easy and hard axis magnetization loops of the stack Ta (5 nm)/FeCoSiB (100 nm)/NiFe (3 nm)/MnIr (8 nm)/Ta (5 nm). The easy axis loop is shifted against the exchange bias field H_{EB} .

The quantity being a measure for the magnitude of the exchange coupling at the interface of the two materials is the exchange bias energy density J_{EB} and its relation

to the exchange bias field H_{EB} is given by

$$H_{\text{EB}} = \frac{J_{\text{EB}}}{t_{\text{FM}}\mu_0 M_s} \quad (1.10)$$

with M_s being the saturation magnetization of the ferromagnetic material and t_{FM} the thickness of the ferromagnetic layer [NS99]. With increasing thickness t_{FM} the exchange bias field decreases since the exchange bias is an interfacial effect.

Exchange bias can be induced by annealing, for which the specimen is brought to a temperature which is above the Neél temperature of the antiferromagnet but below the Curie temperature of the ferromagnet inside a magnetic field and then cooled down to room temperature [NS99]. A system in which the ferromagnetic layer is deposited onto the antiferromagnetic layer is referred to as bottom pinned. In reverse order, top pinning exchange bias can also be induced by aligning the magnetization during thin film growth via a magnetic field. In this case the ferromagnetic layer is magnetized in one direction, which aligns the magnetic moments of the antiferromagnetic layer [LYJ⁺00, FC99, YXZ⁺12]. More information regarding exchange bias and results and discussion on exchange bias for SAW magnetic field sensors can be found in Section 3.4.

1.4 SAW Sensing Mechanism and Noise

1.4.1 Sensitivity

The sensing mechanism of SAW magnetic field sensors is based on the ΔE effect, as described in Section 1.3.2. Applying a magnetic field H will cause a change of magnetization M . The change of M changes the shear modulus G of the magnetic layer due to the ΔE effect. The change in G causes a change of acoustic wave velocity ν which results in a measurable phase change of the SAWs input signal φ . Consequently, the sensitivity S of a SAW delay line sensor is defined as the change of phase φ with applied magnetic field H given by

$$S = \frac{\partial \varphi}{\partial H} = \frac{\partial M}{\partial H} \cdot \frac{\partial G}{\partial M} \cdot \frac{\partial \nu}{\partial G} \cdot \frac{\partial \varphi}{\partial \nu} \quad (1.11)$$

for delay line sensors typically given in units of $^\circ/\text{T}$ or $\text{rad}(\text{radian})/\text{T}$ with $2\pi\text{rad} = 360^\circ$ [DMK⁺21].

The readout schemes for sensitivity and noise in this work have been developed and established by Dr. Phillip Durdaut from Prof. Reinhard Knöchel's and later Prof. Michael Höft's chair of Microwave Engineering at Kiel University [Dur19]. The measurement setup to measure the sensitivity of the SAW delay line sensors of this work is shown in Figure 1.9. Within a magnetically shielded μ -metal cylinder the sensor is

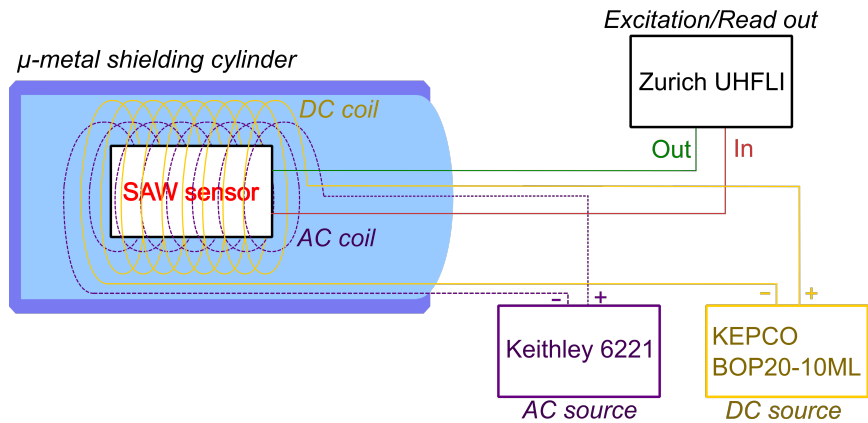


Figure 1.9: Schematic of the readout scheme used in this work to measure the sensitivity of the SAW delay line sensors. In and output are connected to the SAW sensors IDTs, respectively.

placed within two coils/solenoids. One is used to generate DC magnetic fields while the other generates AC magnetic fields. Accordingly, the currents for the coils are provided by an AC and a DC current source. The excitation of the SAW sensor at

its synchronous frequency is realized by using a lock-in amplifier, which also detects the change of the phase. To measure only the total phase change of the SAW sensor a DC magnetic field is swept from one saturation direction to the other and vice versa. Simultaneously, the phase and the amplitude of the SAW signal are read out. To measure the sensitivity an additional sinusoidal AC magnetic field H_{AC} of $f = 10 \text{ Hz}$ and $\mu_0 H_{AC} = 1 \text{ }\mu\text{T}$ is applied. For every DC magnetic bias field a frequency spectrum of the demodulated phase is recorded and the signal peak at 10 Hz is recorded and divided by H_{AC} .

1.4.2 Phase Noise and Limit of Detection

Phase noise is the frequency-dependent statistically random fluctuation of the phase of an oscillating device. When referring to phase noise in this work the power spectral density of phase fluctuations $S_\varphi(f)$ is meant in units of rad^2/Hz [Rub09, p. 22]. It is typically plotted on a dB scale over the logarithmic frequency relative to the center frequency of the SAW device i.e., the carrier signal. A typical phase noise spectrum is shown in Figure 1.10. It exhibits two regions in which the frequency dependency of the phase noise is different. At lower frequencies up to a few kHz the noise decreases proportionally with $1/f$ i.e., the noise drops by one order of magnitude (10 dB) every order of magnitude of frequency. This type of noise is also referred to as $1/f$ noise or pink noise. At higher frequencies the noise is frequency independent and referred to as white noise. The level of the white noise regime of a SAW magnetic field sensor

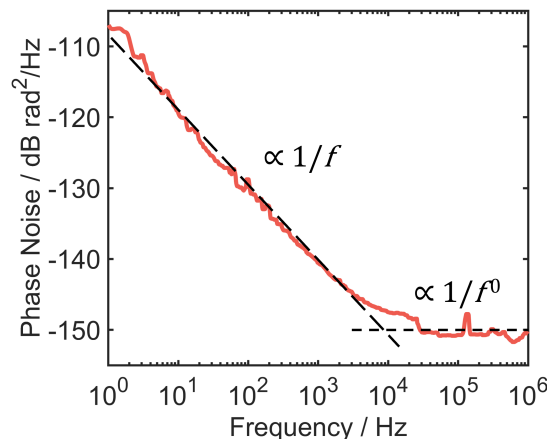


Figure 1.10: A typical phase noise spectrum of a SAW magnetic field delay line sensor at 0 dBm and a defined bias field which is not magnetically saturating the sensor.

is determined by the input power of the SAW sensor P_{SAW} and its insertion loss IL , which is dependent on the magnetic state and hence on the applied magnetic field H_{DC}

and is given by

$$S_{\varphi,\text{white}}(f) = 10 \cdot \log_{10} \left(\frac{IL(H_{\text{DC}}) \cdot k_B \cdot T}{P_{\text{SAW}}} \right) \frac{\text{dB}}{\text{Hz}} \quad (1.12)$$

where k_B is Boltzmann's constant and T the absolute temperature [DMK⁺21], hence the origin of white noise is thermal fluctuations. Consequently, $S_{\varphi,\text{white}}$ can be understood as the power amplitudes of thermal fluctuations relative to the carrier signal's power amplitude. Hence, the smaller the excitation amplitude is, determined by P_{SAW} and $IL_{H_{\text{DC}}}$, the closer it is to the thermal noise.

$1/f$ noise can be understood as the variation of the phase from the phase of the carrier signal. The further away the frequency is from the carrier frequency the less likely it is that an amplitude of that frequency is appearing randomly. At high frequencies $1/f$ noise decreases even below white noise but in the high frequency region thermal fluctuations are more likely to happen than deviations of the carrier signal, consequently the high frequency region is dominated by thermal noise. The phase noise in the $1/f$ regime of a SAW magnetic field sensor is given by

$$S_{\varphi,1/f}(f) = 10 \cdot \log_{10} \left(S^2 \cdot \frac{4k_B T}{2\pi f V} \cdot \frac{\mu_0 \mu_r''}{(\mu_r')^2} \right) \frac{\text{dB}}{\text{Hz}} \quad (1.13)$$

where S is the sensor's sensitivity, f the frequency of the magnetic field, V the magnetic volume and μ_r' and μ_r'' the real and imaginary part of the relative magnetic permeability, respectively [DMK⁺21]. As most parameters are more or less constant $1/f$ noise is determined by μ_r' and μ_r'' , hence the magnetic properties and the magnetic state.

The measurement setup to measure the phase noise of the SAW delay line sensors is shown in Figure 1.11. As commercial current sources do not provide phase noise levels below the sensor's noise, the DC bias fields for noise measurements are provided by an in-house built low-noise current source, which is based on a potentiometer controlled battery set-up developed by Phillip Durdaut [Dur19]. The excitation and read-out of the SAW sensor's phase noise is done with an commercial phase noise analyzer.

The limit of detection (LOD) gives the smallest potentially measurable magnetic field by the sensor as an amplitude spectral density in units of T/ $\sqrt{\text{Hz}}$. The LOD is the quotient of the phase noise $S_{\varphi}(f)$ and the sensitivity S at a specific frequency, thus given by

$$\text{LOD} = \frac{\sqrt{S_{\varphi}}}{S} \quad (1.14)$$

with S_{φ} given in linear units of rad²/Hz and S given in units of rad/T. In previous work it was shown that the sensitivity of the sensors of this work does not change up to

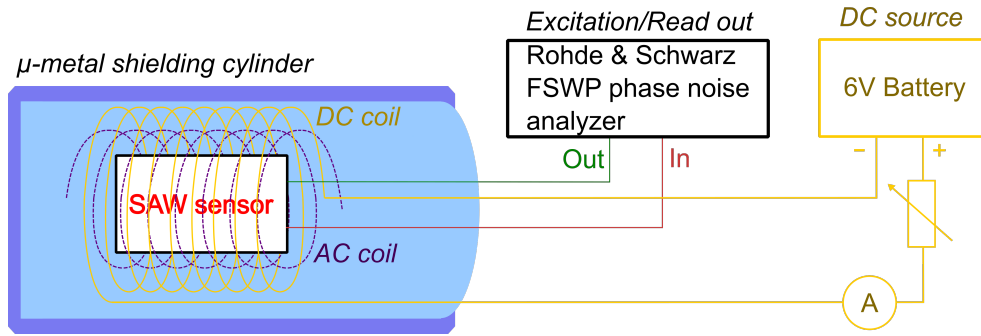


Figure 1.11: Schematic of the read-out scheme used in this work to measure the phase noise of the SAW delay line sensors. In and output are connected to the SAW sensors IDTs, respectively.

a frequency of 10 kHz [LBD⁺19]. Therefore, it is considered frequency independent for the field of application relevant for this work. It can be seen from Equation 1.14 that the best LOD in terms of applied DC bias field does not necessarily coincide with the point of highest sensitivity, but it is a trade-off between noise and sensitivity [DMK⁺21].

1.5 State-of-the-art Magnetic Field Sensors

1.5.1 Magnetometers for Biomagnetic Sensing

Depending on the magnetic field source of the biomagnetic application, different requirements are demanded from the sensor used for magnetic field detection. Whether it is the measurement of the heart's signals (magnetocardiography, MCG), the brain's signals (magnetoencephalography, MEG), signals of muscles (magnetomyography, MMG), signals of nerves (magnetoneurography, MNG) or artificial signals from a deep brain stimulation (DBS) electrode, all of them consist of different amplitudes over different frequency ranges, as shown in Figure 1.12. From this, it becomes evident that for these applications sensors are required that can detect very small amplitudes in the pT (picotesla) to fT (femtotesla) or even aT (attotesla) range.

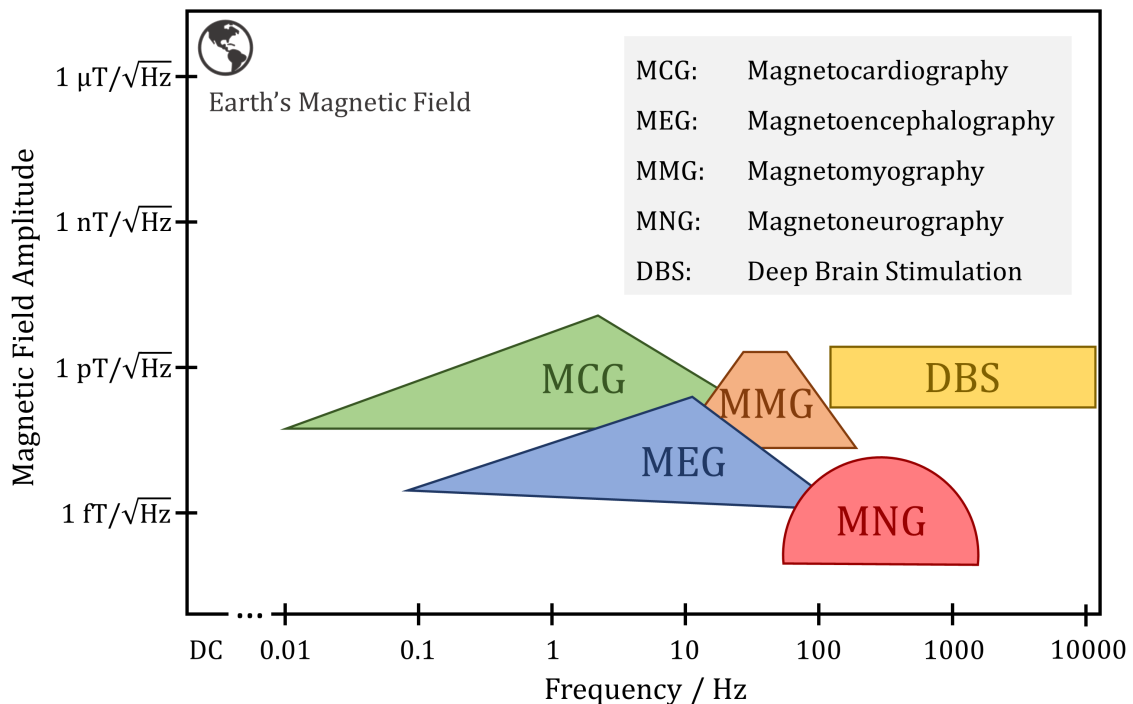


Figure 1.12: Overview of biomagnetic applications. Shown are the amplitudes and frequencies of different biomagnetic signals and the signals of deep brain stimulation electrodes. Both axes are logarithmic. Adapted from Zou et al. [ZHFN20] and extended with DBS range.

SQUID

The whole range of small amplitudes in biomagnetic sensing is only matched by superconducting quantum interference devices (SQUID) which require cryogenic cooling and

magnetic shielding but can detect noise levels even in the $\text{aT}/\sqrt{\text{Hz}}$ range [SHHK19, Fag06]. Nowadays, SQUID MEG systems are established as a reliable and precise clinical diagnosis tool, mostly in combination with MEGs electrical counterpart electroencephalography (EEG) [AM19]. While SQUID-based MEG systems provide excellent localization and time resolution the operation efforts and costs are high. These systems require a complex cooling system which makes them bulky and static. This artificial environment for patients limits the accessibility of this method as well as the number of possible diagnostics. A demand for MEG and MCG systems arises, which allows physically unconstrained movement of the patient’s head or allows for a more natural environment and therefore for a more precise diagnosis. An overview of various magnetic sensors (potentially) capable of biomagnetic sensing is presented in Figure 1.13.

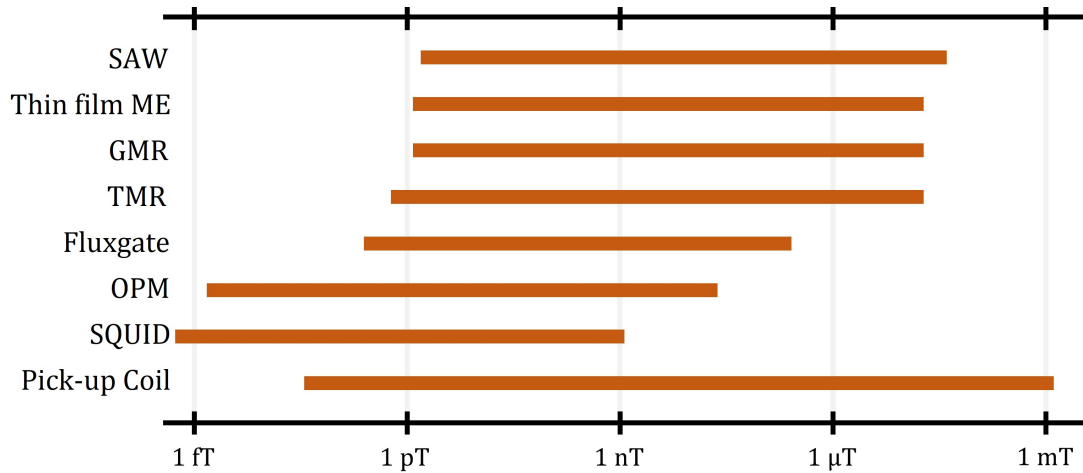


Figure 1.13: Overview of potential sensors for biomagnetic applications showing the detection limits at frequencies relevant for biomagnetic sensing of different magnetic field sensors over a logarithmic scale. SQUIDs and OPMs which can detect fields below 1 pT require strong magnetic shielding to operate. Adapted from Tuman-ski [Tum11] and updated with values partially from Murzin [MML⁺20]. Ranges for thin film ME from [Hay20] and SAW from this work and [KDZ⁺18].

Optically Pumped Magnetometer

A very promising approach are optically pumped magnetometers (OPMs) [BHL⁺18]. These devices consist of a chamber incorporating an alkali metal vapor, e.g. rubidium, which is brought to an elevated temperature (150 °C to 180 °C) [KST19]. The atoms in this vapor chamber are then additionally spin polarized, ‘pumped’, by a laser which is transmitted through the chamber and its intensity is detected by a photo diode [KKAR03]. Upon the application of a magnetic field the polarization direction of the magnetic moments is altered from the polarization of the laser. This

misalignment of laser and magnetic moments leads to a reduction of the light transmission through the chamber and thus the magnetic field strength can be deduced from this alteration. A multichannel whole-head OPM MEG system provides a similar signal-to-noise ratio (SNR) as SQUID systems, while it benefits from a smaller scalp-to-sensor distance [BHL⁺18]. The smallest possible distance in SQUID systems is limited by the required vacuum/cooling system. The room temperature operation of OPMs, as well as their low magnetic noise level (<15 fT/ $\sqrt{\text{Hz}}$) and frequency bandwidth (0.1 Hz – 100 Hz) [QuS22b] make them a very promising alternative to SQUIDs. The magnitude of the magnetic fields from the brain decreases with $1/d^2$ from the source and therefore lead to a significant reduction of SNR for varying head sizes or motion of the head, since the distance of SQUIDs in MEG systems cannot be altered [BBK⁺16]. Due to the reduced distance when using a OPM-based whole head system the brain's signal amplitudes are about 5 times higher compared to SQUID-based systems [SJWH⁺20]. OPMs also have been applied successfully for the recording of magnetocardiograms [SJWH⁺20, MCF⁺17, LFK⁺20]. However, due to their large size, the benefit in terms of mobility and spatial resolution of OPMs compared to classical ECG is questionable. Also, the life time of the laser used for polarization is limited, hence OPMs need to be replaced after a certain time, which is a significant cost factor. As shown in Figure 1.13 OPMs are saturated by fields sufficiently smaller than earth's magnetic field. Therefore, without field compensation they only can be operated within a strong magnetically shielded environment. OPMs which can be operated inside earth's magnetic field significantly suffer from a reduced detectivity with detection limits of about 1 pT/ $\sqrt{\text{Hz}}$ [QuS22a].

Pick-up Coil

While pick-up coils provide a large frequency and measurement range (see Figure 1.13), they are not suited for biomagnetism as they need a large number of windings to achieve the required induction to pick-up very small fields. The large number of windings increases the dimensions of the coil and consequently limit the spatial resolution. However, in nuclear magnetic resonance imaging (MRI) gradient coils are the state-of-the-art as the signals (e.g. hydrogen within a human body) are induced within the coils and the signal increases with sample volume. But also within the field of MRI miniaturization is desired [KMBJ19].

Fluxgate Magnetometer

Another sensor concept providing $\text{pT}/\sqrt{\text{Hz}}$ detectivity is the fluxgate magnetometer [JBD⁺20]. Noise limits as low as $300 \text{ fT}/\sqrt{\text{Hz}}$ at 8 Hz have been achieved with orthogonal fluxgates by improving the read-out electronics [DJB21]. For this concept a high permeability material is immersed into two solenoids and this magnetic material is periodically saturated by applying an excitation current to one of the solenoids [Rip03]. Applying a sensing magnetic field leads to alteration of the dynamic remagnetization process. The modulation of the sensing field induces a voltage in the second solenoid. Fluxgate magnetometers show a frequency bandwidth of about 5 kHz, as shown in Table 1.4, which make them applicable for most biomagnetic applications. MCG measurements were performed with a fluxgate 32-channel array, in which the authors were able to observe the QRS-complex and T-wave (which is another characteristic wave in a cardiogram) of a patient after 120-130 times averaging [KS15]. Later Janosek et al. were able to perform similar MCG measurements with improved fluxgate magnetometers with which they only required 30 averages to measure the T-wave and QRS complex [JBD⁺20].

Magnetoresistance

A further set of sensors is based on different magnetoresistive effects. Namely, these are anisotropic magnetoresistance (AMR), giant magnetoresistance (GMR) and tunnel magnetoresistance (TMR) effects. Those devices already have been implemented successfully into commercial applications as read heads in computer hard drives [Pri98] and the discovery of giant magnetoresistance has even been awarded with the Nobel prize [Nob22]. All three effects are based on the change of the resistance of different materials through which a current flows. In AMR the current is flowing through the magnetic material itself and changes with a change of the magnetic anisotropy direction [MP75]. In GMR a pinned ferromagnetic material is separated from a free ferromagnetic material by a conductive but non-magnetic material. The current amplitude through the non-magnetic material changes upon a change of magnetization of the free layer with respect to the pinned layer. Hence, depending on the orientation of magnetization of the free layer, the non-magnetic layer will show high or low resistance, therefore these devices are also called spin valves [FFCC07]. In TMR the separating layer is an insulating material and the current which changes with magnetization is a tunnel current in the insulating layer [MML⁺20]. In contrast to AMR and GMR where the current flows in-plane, in TMR the tunnel current is flowing through the thin film tunnel barrier, i.e. out of the film plane. Devices based on this effect are termed

magnetic tunnel junctions. Recently, TMR based magnetometers have been presented which show sub-pT detectivity by using thick CoFeSiB layers in combination with magnetic flux concentration [OFK⁺21]. Using similar TMR devices MCG and MEG has been performed [FOK⁺18]. In their work, Fujiwara et al. were able to observe the R-peak without averaging and the QRS-wave with only 16 times averaging. Also MEG signals were observed but with several thousands of averages. Commercially available magnetoresistive sensors have already been used for MCG, too [SHS⁺19].

Magnetoelectric Composite

Magnetoelectric (ME) composites, which consist of mechanically coupled magnetostrictive and piezoelectric materials have again gained more interest during the last decade [SF05, Fie05] as they can also be very sensitive magnetometers [VWMQ18]. ME composite-based magnetic field sensors are often shaped in the form of cantilevers and utilize the resonance frequencies of these cantilevers for sensing. Adhesive bonded ME resonators consisting of bulk piezoelectric bars and ribbons of metallic glass can reach limits of detection as low as $100 \text{ fT}/\sqrt{\text{Hz}}$ [TVK⁺18]. Such low detection limits are only achieved in mechanical resonance of the sensor structure with frequencies in the kHz range with a limited frequency bandwidth. These resonant frequencies are far off the frequencies required for biomagnetic signals and do not provide the required bandwidth. Off-resonance the detection limit of these sensors is more than four orders of magnitude higher. Thin film-based ME composites can reach detection limits as low as $400 \text{ fT}/\sqrt{\text{Hz}}$ in mechanical resonance [YSH⁺16]. These ME composites consist of piezoelectric and magnetostrictive materials which are deposited by thin film techniques such as magnetron sputtering on silicon substrates. As their dimensions are dramatically smaller than the bulk ME composites, thin film ME composites can potentially provide a better spatial resolution and integrability in biomagnetic applications.

The requirement for the dependence of the magnetic field on mechanical resonance can be omitted by applying frequency conversion techniques, but this requires additional equipment such as coils for magnetic frequency conversion [RYU⁺15, SYH⁺22]. Moreover magnetic frequency conversion generates additional noise in the magnetostrictive phase of the sensors limiting their performance [UGR⁺20]. Another form of frequency conversion is using the converse magnetoelectric effect in which the piezoelectric material is excited at a higher order mechanical mode [HJT⁺19]. The oscillation of the magnetic material of the ME composite is then picked up by a coil around the composite through a change of magnetic flux in the coil. A sensing field is modulated

by that flux change and creates a side band in the frequency spectrum of the pick-up coil. In combination with antiparallel exchange biased multilayers [JTR⁺19] converse ME resonators can reach detection limits as low as $17 \text{ pT}/\sqrt{\text{Hz}}$ at biomagnetically relevant frequencies. With this, it was possible to perform MCG in which the QRS complex could be measured after averaging 60 heart beats [Hay20].

Table 1.4: Frequency bandwidths of different magnetic field sensors. Adapted and extended from [ZHFN20].

Principle	Frequency Bandwidth
Pick-up Coil	GHz (no DC)
SQUID	100 kHz
OPM	100 Hz
Fluxgate	5 kHz
xMR	several MHz
Thin film ME [Hay20]	1 kHz
SAW [LBD ⁺ 19]	1 MHz

1.5.2 SAW Magnetic Field Sensors

The SAW sensor's operation in this work is based on the phase shift of Love waves through magnetoelastic coupling in a magnetic material attached to the delay line. The idea of magnetically shifting the phase of the input signal of SAW devices has been introduced already in the 1970s by coating a SAW device with a Nickel film [GDW⁺75]. Mathematically, magnetoelastic coupling with Love waves was even introduced earlier [Mv69]. As Nickel is a quite hard magnetic material and Rayleigh waves are not comprised at the surface as strongly as Love waves (a description of different wave modes is given in Section 1.2) the phase shift was very low with a maximum of 82° at high fields of 120 mT. The first amorphous magnetostrictive thin film on a SAW device has been used in 1978 [FVWD78]. Using the material FeB, which was deposited by co-evaporation, the required magnetic field to achieve the maximum phase shift was reduced by more than two orders of magnitude compared to Ni [WFGV79]. Magnetic field sensing with such devices was first proposed by Hanna [Han87]. For this a ZnO film for SAW generation was sputtered on top of a magnetic garnet film. The SAW delay line oscillator achieved a sensitivity of 700 Hz/mT and could detect $1 \text{ }\mu\text{T}$ changes in a field of 120 mT. Yokokawa et al. also used ZnO films for SAW excitation with which they excited Love waves [YTFI92]. Love wave excitation was possible in this case, because the ZnO film was grown with the c-axis of the Wurtzite structure being in-plane and the propagation direction perpendicular to the c-axis. In combination with amorphous magnetostrictive FeB with isolating SiO_x layers in-between FeB

layers they achieved very high phase changes of $2300^\circ/\text{cm}$. After that several other designs and structures have been investigated, such as IDTs made of magnetostrictive material [KII⁺11], different layer combinations [EEPW⁺16], a combination of SAW devices and giant magnetoimpedance sensors [LYK15], exchange biased magnetic layers [PDL⁺17] or patterning of the magnetoelastic film [WJX⁺18].

In all of the aforementioned works noise or detection limits, which are crucial parameters in biomagnetic sensing or magnetic sensing in general, have not been investigated. As Yokokawa et al. [YTFI92] have shown and which is also known from biological and chemical sensing, Love modes provide higher sensitivities than other wave modes such as Rayleigh modes [JV97, ZRD⁺02]. Hence, prior to this work Kittmann et al. adapted a Love wave sensor on ST-cut quartz with an $4.5\ \mu\text{m}$ thick SiO_2 guiding layer from biosensing [SGT⁺04] for magnetic field sensing [KDZ⁺18]. A $200\ \text{nm}$ thick FeCoSiB layer was deposited on the delay line and limits of detection of $250\ \text{pT}/\sqrt{\text{Hz}}$ at $10\ \text{Hz}$ and $80\ \text{pT}/\sqrt{\text{Hz}}$ at $100\ \text{Hz}$ were achieved. Also it was shown that up to a magnetic field strength of $100\ \mu\text{T}$ the sensor's response is linear. Furthermore, the frequency dependency of the sensor's sensitivity [LBD⁺19] and the dependency of the sensor's performance on the thickness of the magnetostrictive layer [KMD⁺20] were studied. It was shown the sensitivity of the SAW sensors decreases by $3\ \text{dB}$ at a magnetic field frequency of $250\ \text{kHz}$ and drops to nearly zero at $1\ \text{MHz}$. The study on the thickness dependency of the magnetoelastic layer showed that in a range of $100\ \text{nm}$ to $300\ \text{nm}$ the detection limits are virtually the same and the performance mainly depends on the magnetic properties of the layer.

Furthermore, Love wave devices have been investigated with regard to the sensitivity of Love wave resonator structures [LTOY⁺18], the influence of different wave modes on the sensitivity [MDP⁺20, SKD⁺20], other materials as guiding layer for temperature compensation in SAW resonators [MSH⁺20] and different read out methods and their influence on sensor performance [DKR⁺19]. Durdaut et al. studied the phase noise in SAW delay line magnetic field sensors extensively [DMK⁺21], where it was demonstrated that the noise is strongly dependent on the magnetic domain and anisotropy configuration and thus also on the external bias field as shown in Figure 1.14a. There exists a bias field region where the noise is small while exhibiting the lowest possible LOD. It was shown that the noise depends on the excitation power of the SAW sensor as shown in Figure 1.14b. In general, the phase noise decreases with increasing excitation power as the hysteresis losses expressed through the complex part of the relative permeability μ_r'' are decreasing. This is denoted as Region A in Figure 1.14b. At higher excitation powers, however, random Barkhausen domain wall jumps occur which lead to increased so-called random walk of phase noise. This is denoted as Region B in

Figure 1.14b. Through time-resolved magneto-optical Kerr effect microscopy, it was shown that there are strong interactions of the in-plane acoustic waves with magnetic domain walls. These interactions lead to reflections and interference of the waves which potentially leads to phase noise [MDH⁺22]. Therefore a reduction of magnetic domain walls has been identified as a way to further reduce phase noise in these SAW sensors.

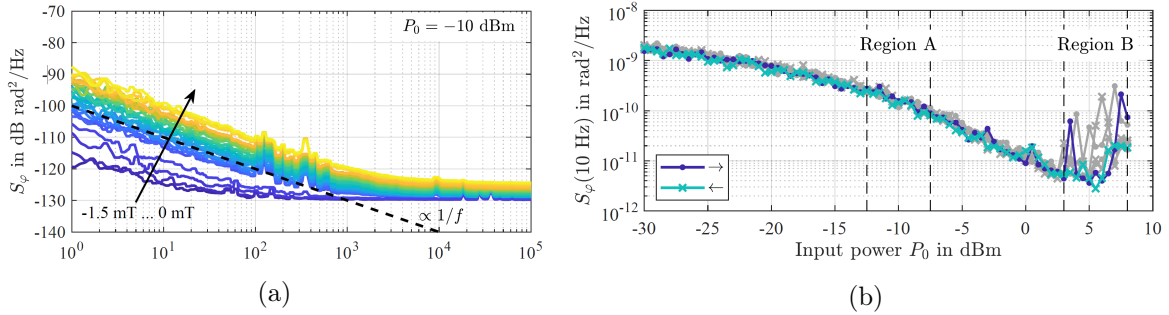


Figure 1.14: Dependency of the phase noise in Love wave magnetic field sensors with a 200 nm FeCoSiB layer on (a) the external bias field strength and (b) the SAW excitation power. In (b) Region A denotes a power region of little random domain wall jumps and Region B a power region of high random domain jumps. [DMK⁺21]

Building upon the prior efforts by Kittmann and Durdaut the goal of this work is to further improve the limit of detection of the SAW Love wave sensors and to identify and realize new material and deposition concepts for these sensors.

Chapter 2

SAW Sensor Fabrication

This chapter gives specific details and instructions, which are not covered in the publications listed in Chapter 3 on the fabrication of SAW delay line sensors used in this work. All fabrication steps were performed in the Kiel Nanolaboratory at Kiel University, which is a ISO class 5 clean room. Therefore, all steps described in this chapter are specific to the clean room in Kiel and optimized for the devices located in this clean room. The first section gives details regarding the fabrication process of the interdigital transducers from magnetron sputtering to ion beam etching. Afterwards the fabrication process of the SiO_2 guiding layer will be discussed in detail. Special emphasis is put on the steps undertaken to achieve SiO_2 of sufficient quality for SAW sensing. The deposition of the magnetostrictive FeCoSiB layer is elaborated in the last section.

2.1 IDTs

Deposition

The interdigital transducers (IDTs) in this work are deposited by DC magnetron sputtering in a *Von Ardenne CS730S* sputtering cluster tool using 8 inch targets. They always consist of Cr/Au/Cr where the thicknesses are 8 nm for both Cr layers and 200 nm to 300 nm for Au. Both Cr layers act as adhesion promoters, the bottom layer for Au and the top layer for the SiO₂ guiding layer, respectively. The following parameters are used for the deposition of each layer:

- Cr: 200 W_{DC}, 25 sccm Ar-flow, 4·10⁻³ mbar, 8 inch target
- Au: 200 W_{DC}, 25 sccm Ar-flow, 6·10⁻³ mbar, 8 inch target

Photolithography

The structuring of the IDTs is done by ion beam etching (IBE) and photolithography. For the photolithography a photomask consisting of 80 delay lines is used. The positive photoresist *AZ1518* by *MicroChemicals* is deposited by spin coating with a spin speed of 4000 rpm resulting in 1.8 μm thickness. Prior to that hexamethyldisilazane (HMDS) is applied to the wafer to prevent delamination of the photoresist during development. The consequences of skipping this step are shown in Figure 2.1. The developer got



Figure 2.1: Light microscopy image of the photoresist AZ nLOF 2070 by MicroChemicals prepared for lift-off on ST-cut quartz. No HMDS was applied and therefore the photoresist delaminated.

underneath the IDT structures which are only $3.5\ \mu\text{m}$ wide and released them from the substrate. For development the *MIF AZ726* developer by *MicroChemicals* is used. Also, the final hard bake should not be omitted, as the photoresist is exposed to elevated temperatures during the subsequent IBE.

To excite Love waves the IDTs need to be oriented along a certain axis on the wafer. For ST-cut quartz this is 90° to the crystallographic X-axis [JV97]. For orientation manufacturers create a wafer flat perpendicular to the crystallographic X-axis and therefore the IDTs are orientated on the wafer with the propagation direction of the acoustic wave parallel to the wafer flat as shown in Figure 2.2. However, it needs to be noted that not all manufacturers stick to this convention. While most European manufacturers will create the flat 90° to the X-axis, in other parts of the world they do not. This is illustrated in Figure 2.2 on langasite where the propagation direction is also 90° to the X-axis, but the flat was placed parallel. Therefore, the IDTs needed to be applied accordingly. Additionally, special care should be taken that the IDTs are aligned parallel to the propagation direction, as deviations by less than 1° can already cause beam steering [Mor07, p. 87 f.].

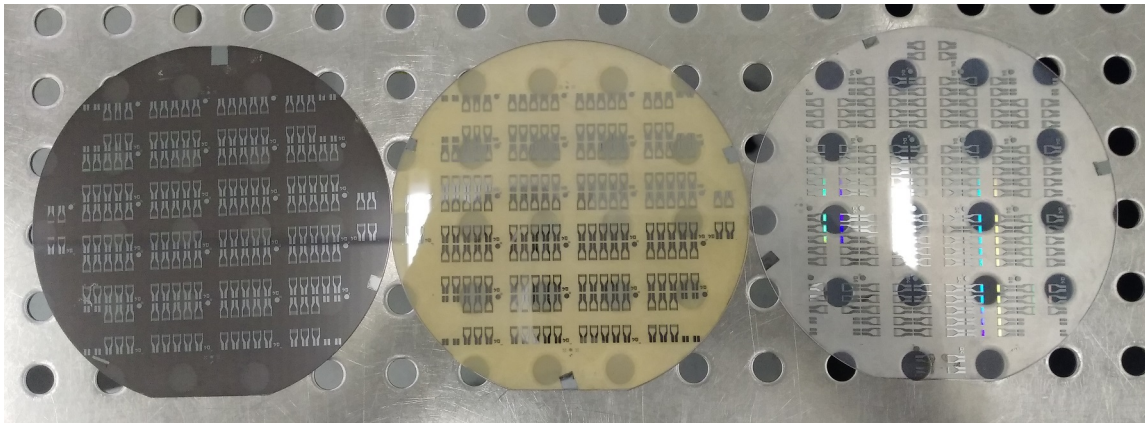


Figure 2.2: IDT orientation on 4" wafers made from different materials. From left to right: 64° Y-cut LiNbO_3 , langasite (0° , 22° , 90°) and ST-cut quartz. On LiNbO_3 the propagation direction is parallel to the x axis, while on Langasite and quartz it is 90° to the X-axis.

Etching

Following the lithography step the final IDT structure is provided by IBE in an *Oxford Instruments* IBE tool. The etching is performed under an angle of 10° with respect to the home position of the wafer. Before etching the 4" quartz wafer is placed on a 6" copper carrier wafer and heat paste is applied on the backside of the quartz wafer to

improve the thermal conductivity. Still, to prevent excessive temperature generation on the wafer and associated burning of the photoresist, the etching is performed in sequences of 3.5 minutes of etching and pauses of 3.5 minutes while the sample is rotating. The etching process is monitored by secondary ion mass spectroscopy (SIMS), where the released ions of each involved material are plotted over time. The SIMS profiles of the IDT etching process are shown in Figure 2.3a. At the end of the process the Cr signal has stopped decreasing and the Si signal stopped increasing, hence the process is stopped. The etching process is monitored by secondary ion mass spectroscopy (SIMS), where the released ions of each involved material are recorded over time. The SIMS profiles from the IDT etching process are shown in Figure 2.3a. The end of the process is reached, when the Cr signal has stopped decreasing and the Si signal has stopped increasing.

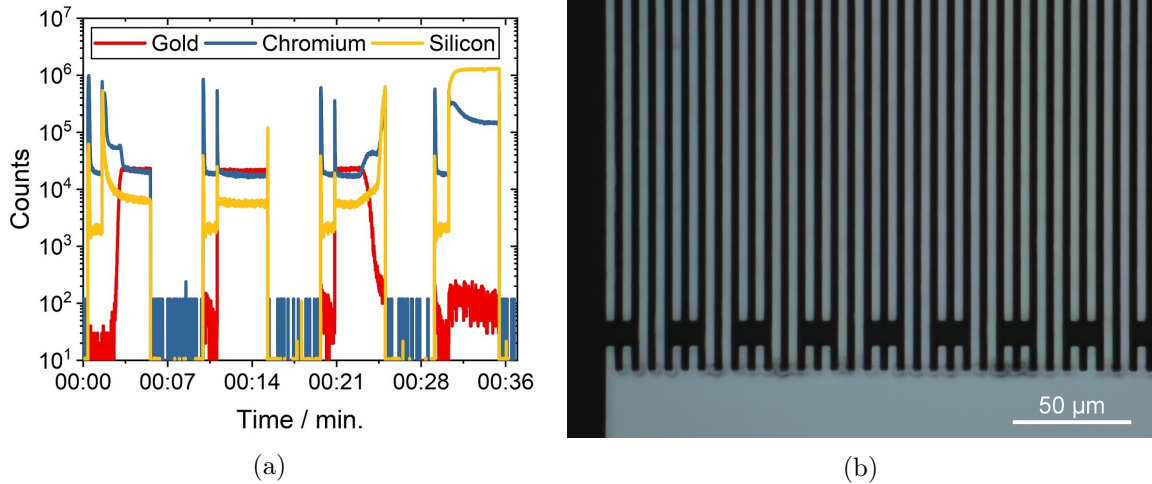


Figure 2.3: Results of ion beam etching. (a) SIMS profile of the etched materials. (b) Microscope image of the final IDT structure after IBE. Bright areas are the metalization. The width and spacing of and in-between each IDT finger is 3.5 μm , respectively.

After etching the surplus photoresist is removed using acetone in an ultrasonic bath. As Cr is used as an adhesion layer higher ultrasonic powers can be applied. If the resist is slightly burned nonetheless and more difficult to remove, slightly elevated temperatures below 60 $^{\circ}\text{C}$ can be applied to the bath. The final double finger IDT structure is shown in Figure 2.3b. The width and spacing of the fingers are 3.5 μm , respectively, which results in an acoustic wave length of $\lambda = 28 \mu\text{m}$.

2.2 Guiding Layer

Deposition

The SiO₂ guiding layers in this work were deposited by plasma-enhanced chemical vapor deposition (PECVD). A schematic of the PECVD chamber is shown in Figure 2.4. The *Sentech* SI 500 PPD deposition tool consists of a shower head through which the plasma as well as the reaction gases are inserted. The top electrode is located at the center of the shower head and the bias is applied between the top and bottom electrodes via a RF generator. A substrate heater is incorporated into the bottom electrode. The temperature is controlled using the heater in combination with active

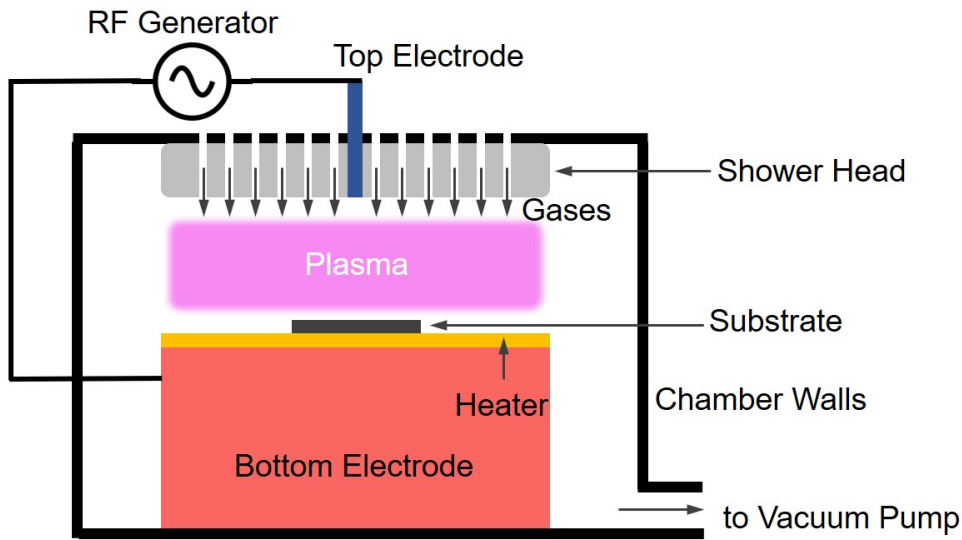


Figure 2.4: Schematic of a PECVD chamber.

cooling through a circulation chiller. The parameters used for the deposition of SiO₂ are listed in Table 2.1 and are based on the work of Hölken [Höl12].

Table 2.1: Deposition Parameters for SiO₂ deposition by PECVD.

Parameter	Value	Unit
Pressure	0.8	mbar
Power	50	W
Temperature	300	°C
SiH ₄ (5 % SiH ₄ in Ar)	104	sccm
N ₂ O	65	sccm
Ar	225	sccm
N ₂	75	sccm

Prior to deposition the vacuum chamber vacuum is at a base pressure of 10^{-7} mbar range. For the lack of an intermediate transfer chamber, the deposition process is started after about 15 minutes following the transfer of the sample from the load lock into the deposition chamber. Upon reaching the process temperature the reaction gases SiH_4 and N_2O are introduced into the chamber, the plasma is ignited and the depositions starts. Typical deposition rates are in the order of 1.55 nm/s, therefore a process duration of about 43 minutes equals a film thickness of 4 μm . After the deposition, the RF bias is turned off and all gas inlets are closed. The heating is turned off immediately and the wafer removed from the chamber, while the temperature is still elevated.

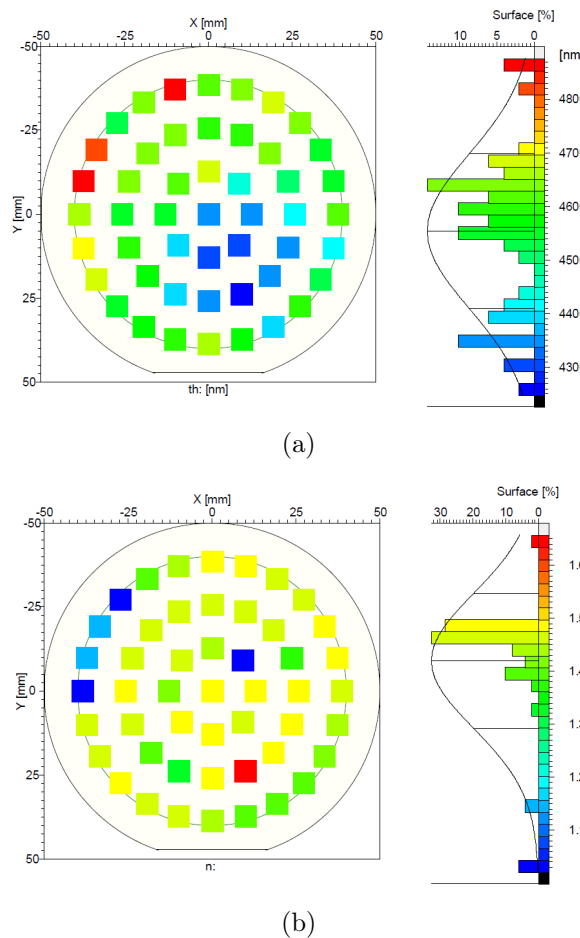


Figure 2.5: Ellipsometry on SiO_2 deposited for 50 minutes on Si wafers. (a) thickness and (b) refractive index over a 4" wafer.

The thickness and refractive index of the deposited layers can be monitored by ellipsometry if the films are deposited on a non-transparent substrate such as silicon. Ellipsometry scans with a laser ellipsometer SE 400adv by Sentech are shown in Figure 2.5 over a 4" Si wafer. The measurement was conducted in the so-called

Combined Ellipsometry and Reflectometry (CER) mode, during which reflectometry measurements are additionally performed as a reference. In Figure 2.5a the thickness distribution for an entire 4" wafer is shown. In general, SiO₂ layers deposited by PECVD from a shower head exhibit lower thicknesses in the center of the wafer, as the electrode in the PECVD chamber is located above the center of the wafer. At the location of the top electrode there are no gas outlets, therefore there are no reaction gases directed at the wafer center. The thickness variation from center to wafer edge is about 6.5%. Additionally, in Figure 2.5b the refractive index n for an entire 4" wafer is shown. According to the ellipsometer's software database the refractive index of stoichiometric SiO₂ from PECVD should be 1.46. On average the measurement is in good agreement with this expected value. A variation in n corresponds with a variation of mechanical properties. Accordingly, due to the variation of the thickness and n a variation of SAW frequency in the final device occurs, as well as a slight variation in sensitivity. Therefore, if the desired SiO₂ thickness is 4 μm the frequency of the final SAW device is varying between 139 MHz to 145 MHz, due to the thickness variation from the wafer edge to the wafer the center. Regarding the sensitivity, however, the properties of the magnetostrictive film are more decisive and thus it is not straight forward to distinguish the guiding layers contribution accordingly.

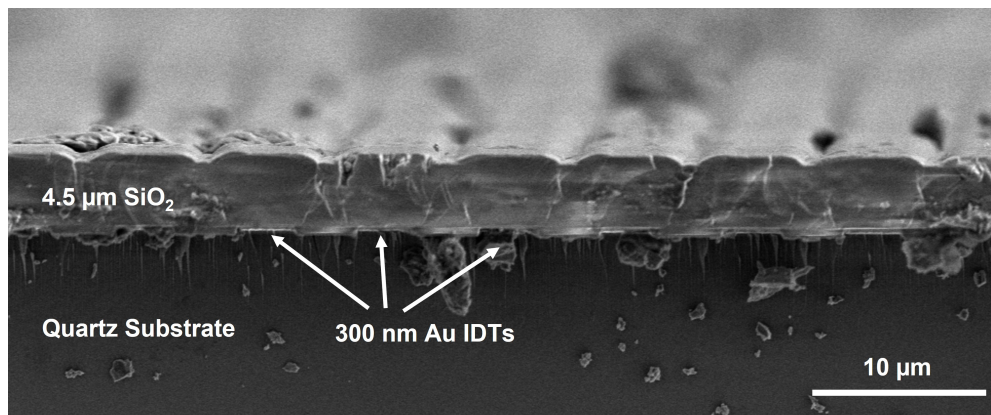


Figure 2.6: Scanning electron microscopy image showing a cross section of an 4.5 μm SiO₂ layer deposited by PECVD on ST-cut quartz and Cr/Au (300 nm)/Cr IDTs. Image taken by Patricia Pop-Ghe.

Figure 2.6 shows a scanning electron microscopy (SEM) image of a cross-section of an SiO₂ layer deposited on ST-cut quartz with 300 nm thick Au IDTs. The SiO₂ layer shows a grating-like topography provided by the IDTs beneath. Such gratings can lead to potential reflections of the acoustic waves and hence to an increase of insertion loss [Has00, p. 25 ff.]. To overcome this the oxide layer can be treated by chemical-mechanical polishing (CMP). However, for CMP a thicker layer needs to be deposited

which potentially leads to a degradation of the SiO_2 layer, as with a longer deposition time more defects are incorporated into the film.

To ensure sufficient quality of the SiO_2 even after several depositions the correct conditioning of the deposition chamber is crucial. With regard to the Sentech SI 500 PPD system it is necessary to clean the chamber mechanically as soon as particel-like contamination appears on the deposited film. Afterwards, a SiO_2 deposition process for a few minutes is performed to cover the chamber walls with a thin layer of SiO_2 , as this prevents the release of atoms from the chamber walls into the plasma through etching and thus undesired changes of the plasma composition [GKK⁺14].

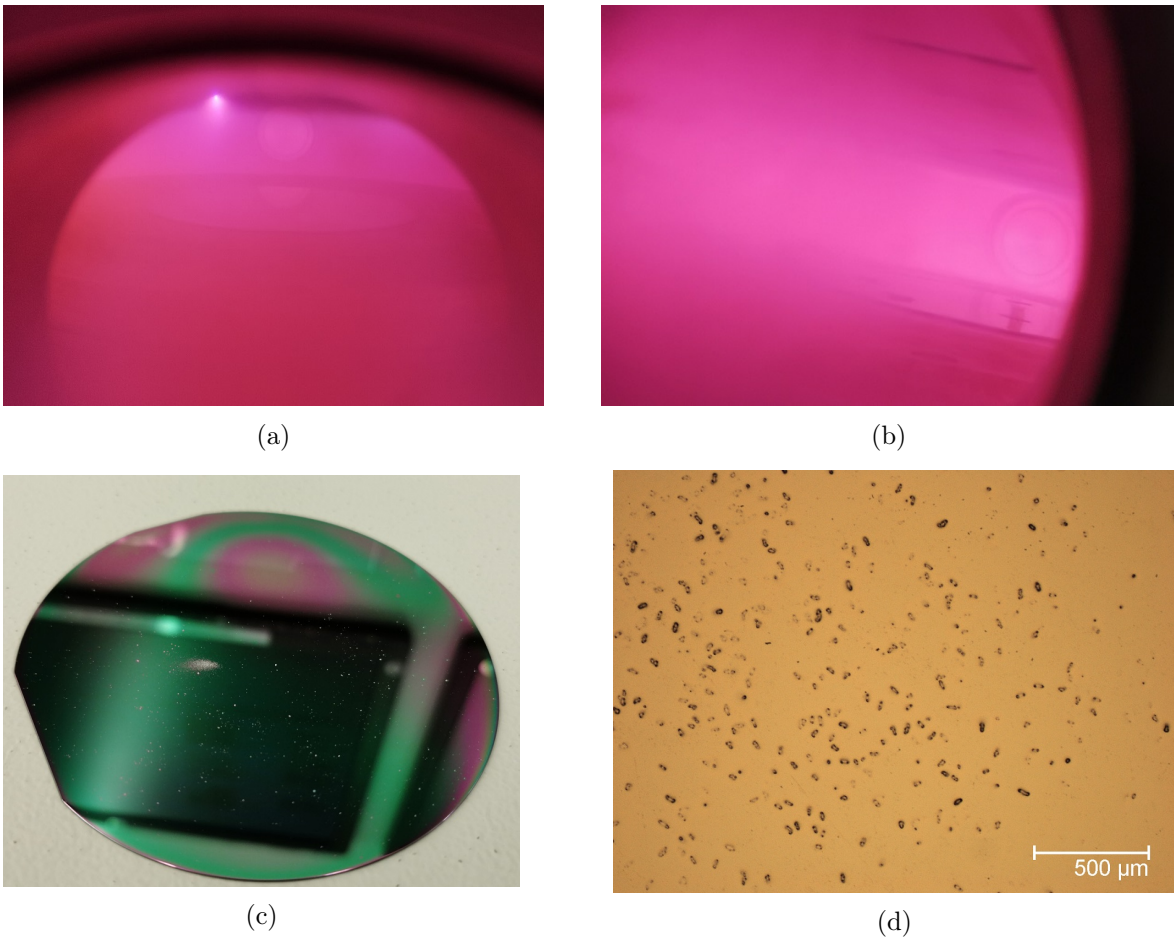


Figure 2.7: Influence of chamber conditioning. (a) N_2 plasma directly after SiO_2 deposition. A bright spot on the shower head appears which is located next to the electrode. (b) N_2 plasma after 20 minutes of prior N_2 plasma cleaning. No bright spot appears and the plasma is homogeneous in color. (c) SiO_2 on a Si wafer deposited after several $4.5 \mu\text{m}$ SiO_2 depositions without N_2 plasma cleaning in-between. White powder-like contamination appears on the wafer surface. (d) Light microscopy image of a SiO_2 layer deposited without pre-conditioning.

Despite the advantages of covering the chamber with the same material as the one which is deposited, the top electrode has to stay clean. Coverage of the top electrode with insulating SiO₂ leads to a change of the induced bias voltage and to an alteration of the PECVD plasma process. Hence, to prevent the covering of the top electrode after every deposition a N₂ plasma cleaning is performed. Additionally, the N₂ plasma can be used to monitor the condition of the top electrode. As Figure 2.7a shows directly after SiO₂ deposition the N₂ plasma contains a bright spot and additionally the bias voltage is elevated to as high as 8 V. This indicates an plasma arcing since the contact to the top electrode is inhibited. After 20 minutes of N₂ plasma cleaning the N₂ plasma shows no such arc as shown in Figure 2.7b and consequently the bias voltage is found to be around 0 V. The consequence of not performing N₂ plasma cleaning are shown in Figure 2.7c and in the light microscopy image in Figure 2.7d. In Figure 2.7c it can be seen that a residual powder-like contamination appears on the surface, which might stem from reactions that occur in proximity of the wafer surface, as the center of the electrode setup shifts if the top electrode is contaminated. Further, in Figure 2.7d it can be seen that this contamination is implemented into the film. This results in a degradation of the wave guiding properties of the layer and provides a poor surface morphology for the subsequently deposited magnetostrictive layer.

Etching

To enable electrical measurements the SAW sensors are wire bonded to custom printed circuit boards (PCBs), for which contact pads are released by means of inductively-coupled plasma - reactive ion etching (ICP-RIE). As an etching mask the positive photoresist AZ4562 is applied via spin coating and structured by photolithography prior to etching. The photoresist is chosen to be sufficiently thicker than the 4 μm SiO₂ layer as it is also etched during the reactive etching. Subsequently, the wafer is mounted on an aluminum 6 " carrier wafer and thermally connected by applying heat paste. The guiding layer is then etched by a ICP-RIE plasma etcher SI 500 using CHF₃ as the reactive gas. The process pressure during etching is $p = 4 \cdot 10^{-2}$ mbar, the RF power $P = 250$ W, the Ar flow 75 sccm and the flow of the reactive gas CHF₃ 25 sccm. The etching rate is approximately 1.5 nm/s. Notably, the thickness of the SiO₂ layer is varying over the wafer, which causes a variation of the times required to etch through the SiO₂ throughout the wafer. After etching the thermal paste is removed and the photoresist stripped from the wafer surface.

2.3 Magnetostrictive Film

The magnetoelastic material used as the sensitive element in this work is an alloy with nominal composition $(\text{Fe}_{90}\text{Co}_{10})_{78}\text{Si}_{12}\text{B}_{10}$, which is deposited by RF magnetron sputtering. The basis of this work was a single layer of 200 nm FeCoSiB (see Section 3.1 and Section 3.2), which later was extended to an exchange bias system wherein the FeCoSiB is coupled to an antiferromagnetic $\text{Mn}_{80}\text{Ir}_{20}$ layer. The detailed fabrication and deposition process of these thin films is described in the following.

Preparation

As shown by Kittmann [Kit20] thermal treatment of FeCoSiB in a magnetic field cannot be applied on ST-cut quartz-based devices due to the anisotropic thermal expansion coefficients present in quartz. Therefore, the deposition needs to be performed in a magnetic field. For the magnetron sputtering of the magnetoelastic film the Von Ardenne CS730S cluster tool was used, which is capable of providing a build-in magnetic field with a field strength of approximately $H_{\text{Ardenne}} = 10$ mT. However, it turns out that this magnetic field is not homogeneous enough to induce a uniaxial anisotropy in the thin films along the intended axis. Alternatively, magnetic fields are introduced with permanent magnets mounted on to the 6" carrier plates together with the samples. While this provides sufficient homogeneity to induce uniaxial magnetic anisotropy, the size and amount of processable samples is significantly reduced, as only small permanent magnets can be introduced into the chamber due to limitations of the wafer transferring system. Therefore, depositions in this work are performed on chips consisting of two delay lines only, which are placed in the center of two permanent magnets aligned in parallel. Consequently, wafers consisting of 80 delay lines are diced into chips of two delay lines per chip by means of wafer dicing. Afterwards, the single chips are cleaned and photolithography is performed to structure the delay lines for the post-deposition lift-off of the FeCoSiB alloy. For lift-off either the negative photoresist AZ nLOF 2070 or the image reversal resist AZ 5214e have been used. No influence of the different photoresists on magnetic properties was observed.

Deposition

The sputtering parameters for the materials used for single layers and for exchange biased layers, namely Ta, FeCoSiB, $\text{Ni}_{81}\text{Fe}_{19}$ and MnIr are listed in Table 2.2. The depositions of FeCoSiB and NiFe are done by RF magnetron sputtering as the permeabilities of these materials are too high to ignite a plasma by DC bias. Further, applying a RF bias only is not sufficient to ignite a plasma, as a large portion of the

magnetic flux lines are concentrated in the target. To overcome this limitation, the plasma is ignited on another carrier plate on which a magnetic field is present through built-in permanent magnets. This additional magnetic field increases the magnetic flux outside of the target and makes the plasma ignition possible.

Table 2.2: Deposition parameters of all layers used for the exchange bias stack and single layers of FeCoSiB. The deposition of FeCoSiB is performed in sequences of 30 s depositions followed by 300 s pauses. The number next to the deposition rate gives the thickness offset, given by the ignition of the plasma (DC) or the movement of the sample (RF).

Material	Target Size / "	Power / W	Pressure / mbar	Ar Flow / sccm	Deposition Rate / nm/s
Ta	8	200 DC	$4 \cdot 10^{-3}$	30	0.45 + 2.5 nm
FeCoSiB	8	200 RF	$6 \cdot 10^{-3}$	40	0.18 + 0.7 nm
NiFe	8	200 RF	$6 \cdot 10^{-3}$	40	0.23 + 1.2 nm
MnIr	4	40 DC	$2 \cdot 10^{-3}$	16	0.33 + 2.7 nm

After ignition and impedance matching of the RF matchbox of about 20 seconds the actual sample is moved beneath the target by the rotating sample holder of the sputtering tool. After the deposition is completed, the sample is moved out from beneath the target in the same direction as it moved in while the plasma is still burning. In addition to the fact that heat treatments cannot be applied to quartz substrates, also the depositions need to be performed in a way, in which the heating of the substrate by the plasma is prevented. To achieve this cooling periods are introduced between depositions, which are longer than the deposition time of a single deposition period. Within the master's thesis of Thormählen the optimum ratio of deposition time and cooling time was found to be 1:10, i.e. 30 seconds of deposition and 300 seconds of cooling time in which the plasma is turned off [Tho17]. Performing the deposition this way prevents heating of the carrier plate above 40 °C.

The NdFeB permanent magnets used to generate the magnetic field which magnetizes the FeCoSiB layers have dimensions of 25.6·2 mm³. In a first attempt two permanent magnets were placed parallel to each other and fixed by Aluminum clamps on an Aluminum carrier plate as shown in Figure 2.8a and the sample was placed on the carrier wafer directly. In Figure 2.9a hysteresis loops of the top pinning exchange bias system FeCoSiB (100 nm) / NiFe (6 nm) / MnIr (8 nm) are depicted, which were obtained parallel and perpendicular with regard to the applied magnetic field during deposition. On the basis of these it can be derived that there is an exchange bias present as for one the loops being shifted along the field axis. However, the anisotropy in the film is not as intended, since the easy axis of magnetization was supposed to be parallel to the applied magnetic field. In addition, the perpendicular loop is shifted in-

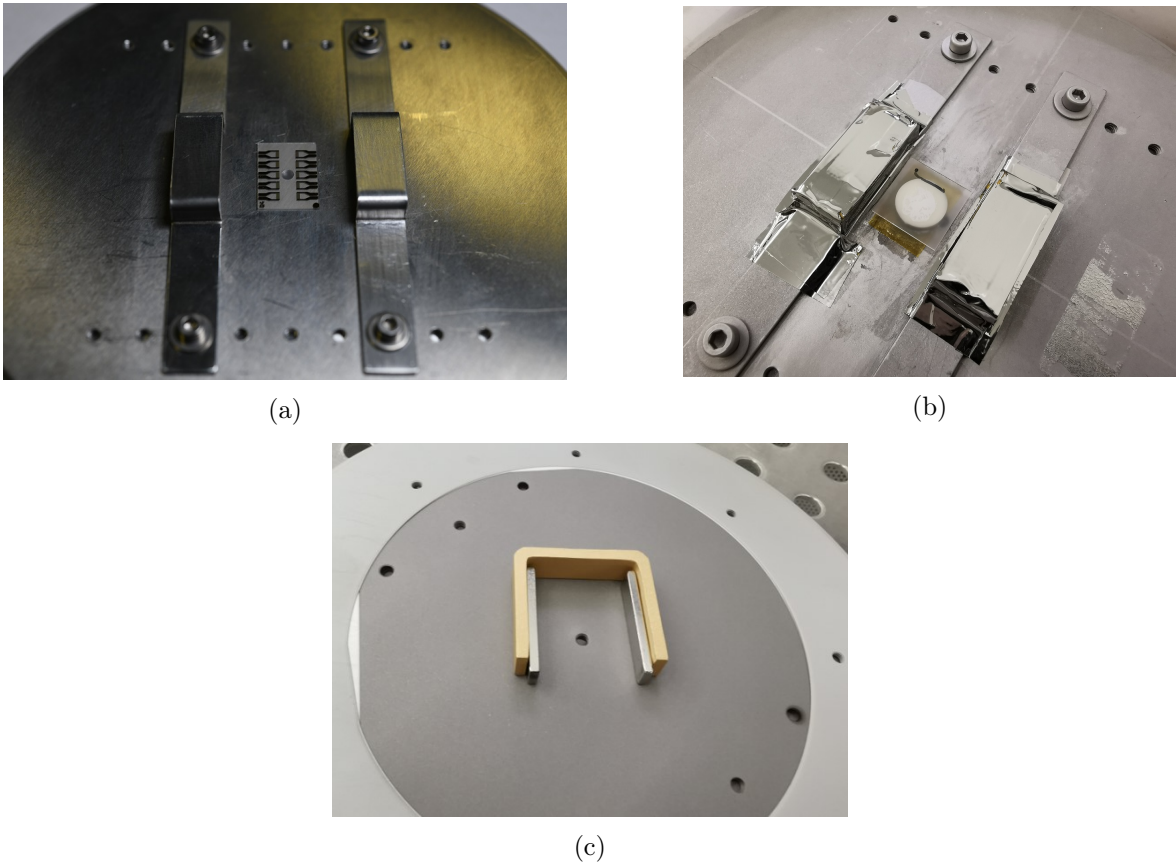


Figure 2.8: Different permanent magnet setups. (a) First attempt with only two NdFeB magnets placed parallel. (b) Al_2O_3 disc used to decouple the sample from the carrier wafer. (c) NdFeB magnets connected by a ferromagnetic steel yoke which generate a magnetic field of at least 60 mT. The yokes are passivated utilizing a 100 nm thin Au layer coating.

dicating that the anisotropy axis as well as the exchange bias direction are tilted. These tilts in anisotropy have been associated with the given anisotropic thermal expansion of the substrate, due to its heating during film growth. A ceramic Al_2O_3 separator was introduced beneath the sample and is fixed by heat paste as shown in Figure 2.8b as a measure to avoid heating of the Al carrier wafer. The corresponding magnetization loops are given in Figure 2.9b for the same exchange bias system as before.

Only one of the resulting hysteresis loops exhibits a shift indicating that the exchange bias direction corresponds to the applied magnetic field direction. However, these loops show little uniaxial anisotropy, suggesting that the deposition field is not homogeneous enough to induce such anisotropy. To improve the homogeneity and magnitude of the generated magnetic field the two permanent magnets are connected by a ferromagnetic yoke as shown in Figure 2.8c. Finally, the resulting hysteresis loops in case of application of an Al_2O_3 disc are displayed in Figure 2.9c. By the magnetic field an easy axis

of magnetization was introduced which is parallel to the applied magnetic field.

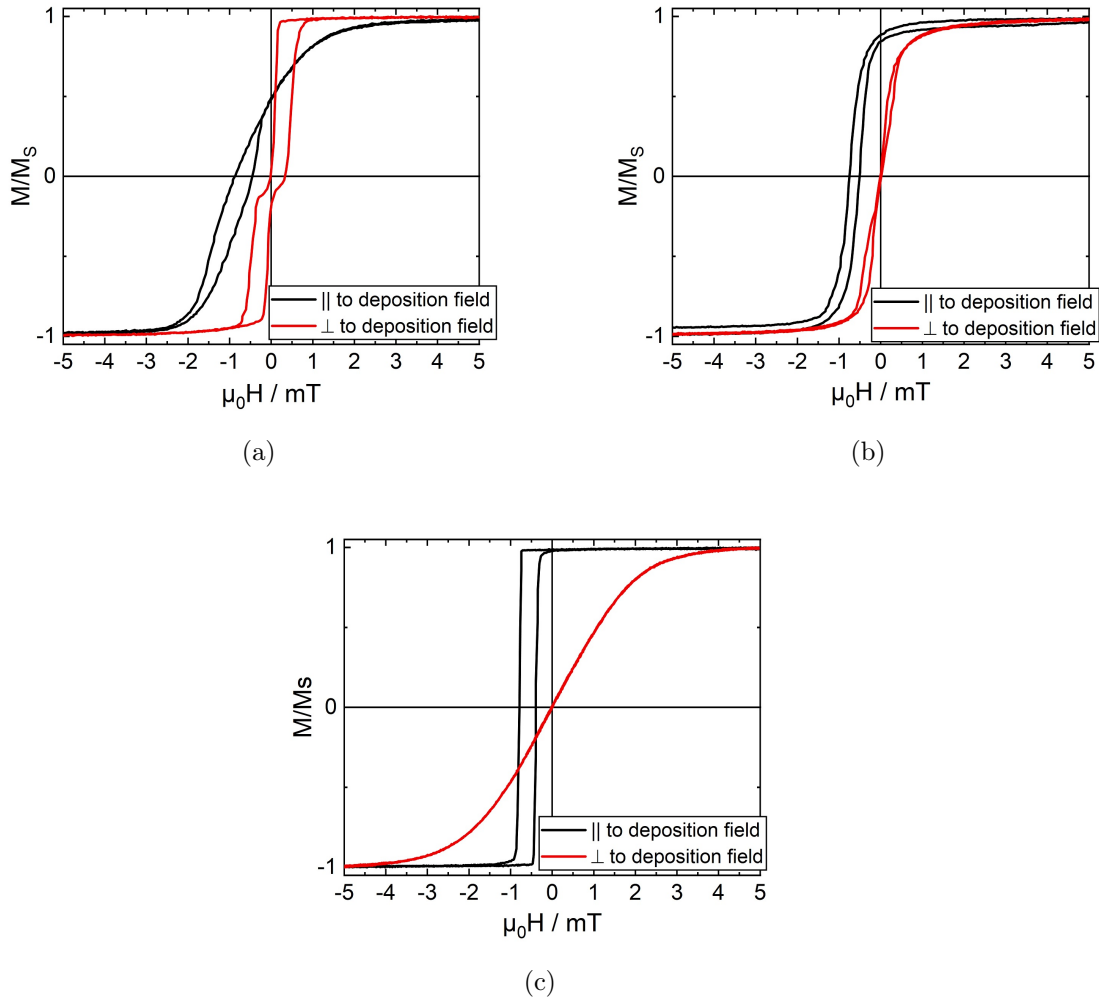


Figure 2.9: Magnetization loops of the exchange bias stack FeCoSiB (100 nm)/NiFe (6 nm)/MnIr (8 nm) on ST-cut quartz deposited using the different permanent magnet setups in Figure 2.8. (a) Deposition only with two NdFeB magnets as shown in Figure 2.8a. (b) Deposition with an Al_2O_3 disc to decouple the sample from the carrier wafer as shown in Figure 2.8b. (c) Deposition done with the NdFeB magnets connected by a yoke (Figure 2.8c) and on a Al_2O_3 spacer. The deposition field was applied with 90° to the X-axis of the quartz substrate.

Separating the sample from the carrier plate also improves the reproducibility of the deposited FeCoSiB films. This is demonstrated in Figure 2.10 for 200 nm thick single layers of FeCoSiB, which shows hysteresis loops parallel and perpendicular to the deposition field. They originate from four different films deposited separately. In all cases hard and easy axis of magnetization are aligned 90° with respect to each other. Only a small variation of the anisotropy field $\mu_0 H_k$ between 1.6 mT and 2 mT is

observed. Due to the separation of the sample and the Al carrier less heat is transferred to the sample, which reduces the influence of strain originating from the anisotropic thermal expansion.

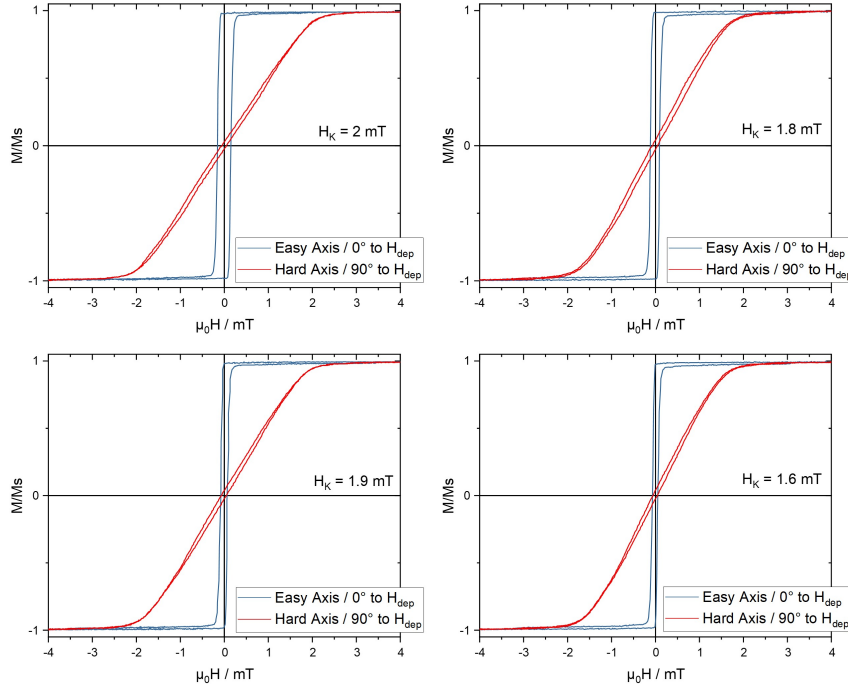


Figure 2.10: Hysteresis loops for 200 nm FeCoSiB measured along the easy and hard axis of magnetization from four different depositions, respectively using a yoke and an Al₂O₃ spacer. The easy axis correlates with the field direction applied during deposition. The samples in this case were circles with a diameter of 13.8 mm on ST-cut quartz. The field was applied with 90° relative to the crystallographic X-axis of the quartz cut.

Ion Beam Etching

Instead of lift-off the magnetostrictive film can also be structured via ion beam etching (IBE). IBE has the advantage of inhibiting less edge domains forming in the magnetic film, as the films in the exchange bias stack do not get thinner towards the edges, which is the case for films structured by lift-off due to shadowing during layer deposition. In a first attempt, the etching has been performed on exchange biased FeCoSiB under an angle of 60° with respect to the ion beam. As shown in Figure 2.11a etching under this angle leads to shadowing on the contact pads. While there is still residual FeCoSiB in the area without guiding layer, the contact pads have been removed by the etching. Additionally, Figure 2.11a shows that due to the poor coating of the photoresist on

the SAW chips the edges of the chips are still covered by FeCoSiB leading to short circuiting of the contact pads. As a solution to both issues, an etching angle of 80° with respect to the ion beam (10° with respect to 0° position in the IBE device) was chosen. In addition, during sputtering the edges of the chips are covered to prevent deposition on the edges.

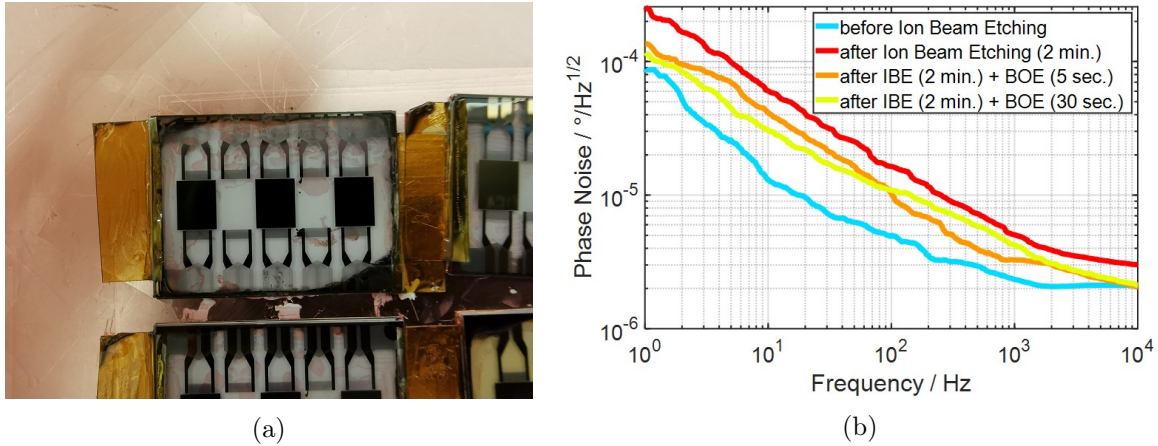


Figure 2.11: Influence of ion beam etching of the FeCoSiB layer on the SAW sensor. (a) Photograph of a SAW sensor after IBE at 30° (60° with respect to the ion beam). (b) Phase noise of a SAW device without a FeCoSiB layer before IBE, after IBE and after a buffered HF oxide etch (BOE) of 5 s and 30 s.

While it was shown that ion beam etching can be applied even on small SAW chips another severe disadvantage was revealed in the characterization of the sensor performance. As demonstrated in Figure 2.11b the ion beam etching leads to an increase in the sensor's noise, independent of the magnetostrictive layer. The SAW device in Figure 2.11b was not coated with FeCoSiB and the phase noise was measured before etching and after 2 minutes of etching. The amplitude phase noise increases by a factor of about 3 after etching the entire delay line. This corresponds to a factor of 6 in the power spectral density in the $1/f$ regime. A similar noise increase was observed in MOSFET devices after the etching of the gate oxide [HMW⁺94]. However, a chemical wet etching step after the dry etching reduces the surface roughness, which decreases the $1/f$ noise in FET devices again [SSL⁺15]. Consequently, wet etching was also performed on ion beam etched SAW devices. Indeed, Figure 2.11b shows that in SAW devices the noise decreases again by a factor of approximately 1.2 after an buffered oxide etch (BOE) in hydrofluoric acid for 5 seconds. However, increasing the etching time does not further decrease the $1/f$ noise. Therefore other mechanisms besides surface roughness seem to act as noise sources after IBE. Based on these results, the exchange biased layers in this work were structured by lift-off.

Chapter 3

Publications

In this chapter the results of this work are presented. These results are in the form of three per-reviewed publications and one manuscript which is submitted for publication at the time of submission of this thesis. Each manuscript will be shortly introduced in each section, its novelty and contribution to the state-of-the-art will be outlined and the contributions of the author to each manuscript will be listed.

3.1 Magnetic Anisotropy Controlled FeCoSiB Thin Films

Based upon previous investigations by Kittmann [Kit20] in this publication the influence of the quartz substrate on the performance of SAW delay line magnetic field sensors is demonstrated. Crystalline quartz is a highly anisotropic material, which makes it very versatile and suitable for many different applications. However, this anisotropy is detrimental for the magnetic properties and anisotropy of the magnetic film deposited on the quartz. In case of ST-cut quartz the thermal expansion coefficient is smaller along the propagation direction. It was shown that annealing the magnetoelastic film on the SAW sensor leads to a severe reduction of the sensor's sensitivity as with the same temperature treatment the anisotropy field H_k becomes nearly one order of magnitude larger than on silicon. This increase in H_k is due to the thermally generated strain acting along the same axis during cooling as the applied magnetic field. As a consequence, the uniaxial anisotropy along the SAW propagation direction was induced by a magnetic field applied during deposition, leading to anisotropy fields comparable to films on Si substrates. The precise control of anisotropy enables an improvement of the sensor's performance with limits of detection as low as 70 pT/ $\sqrt{\text{Hz}}$ at 10 Hz and 25 pT/ $\sqrt{\text{Hz}}$ at 100 Hz. These are the lowest detection limits reported for SAW magnetic field sensors at the time of publication, underlining the importance of magnetic anisotropy on the performance of SAW magnetic field sensors.

Authors Contribution

Own contribution to the manuscript:

- Measurements and preparation of samples (large fraction)
- Interpretation of the results (large fraction)
- Preparation of figures (large fraction)
- Data analysis (large fraction)
- Writing of the manuscript (large fraction)
- Fabrication of samples (shared)
- Designing experiments (shared)

Reproduced from *Appl. Phys. Lett.* **116**, 073503 (2020); DOI: 10.1063/1.5140562, with the permission of AIP Publishing.

Magnetic anisotropy controlled FeCoSiB thin films for surface acoustic wave magnetic field sensors

Cite as: Appl. Phys. Lett. **116**, 073503 (2020); doi: [10.1063/1.5140562](https://doi.org/10.1063/1.5140562)

Submitted: 28 November 2019 · Accepted: 7 February 2020 ·

Published Online: 19 February 2020



Viktor Schell,¹ Cai Müller,¹ Phillip Durdaut,² Anne Kittmann,¹ Lars Thormählen,¹ Fabian Lofink,³ Dirk Meyners,¹ Michael Höft,² Jeffrey McCord,¹ and Eckhard Quandt^{1,a)}

AFFILIATIONS

¹Institute for Materials Science, Kiel University, Kiel 24143, Germany

²Institute of Electrical Engineering and Information Technology, Kiel University, Kiel 24143, Germany

³Fraunhofer Institute for Silicon Technology ISIT, Itzehoe 25524, Germany

^{a)}Author to whom correspondence should be addressed: eq@tf.uni-kiel.de

ABSTRACT

Surface acoustic wave magnetic field sensors based on guided Love waves using the ΔE effect of a magnetostrictive thin film have been shown to be promising candidates for the measurement of weak fields at low frequencies as required for biomagnetic applications or as current sensors benefitting from the large dynamic range and bandwidth. The deposition of soft magnetic films with high magnetostriction is, however, more challenging on piezoelectric substrates such as quartz than on silicon. Thermally induced anisotropic expansion during the deposition process or during post-deposition magnetic field annealing leads to uniaxial stresses acting on the films, which makes the precise control of magnetic anisotropy difficult. Accordingly, this work analyzes the influence of the deposition process and heat treatment on the performance of Love wave devices. ST-cut quartz based delay line surface acoustic wave sensors with a SiO₂ guiding layer are employed, and a 200 nm layer of amorphous magnetostrictive (Fe₉₀Co₁₀)₇₈Si₁₂B₁₀ is used as the sensitive element. Magneto-optical imaging is performed for magnetic domain characterization, and the sensor performance is characterized in terms of bias field dependent phase sensitivity and frequency dependent phase noise. By performing a low temperature deposition in an external magnetic field, considerable improvement in limits of detection at biomagnetic relevant frequencies down to 70 pT/ $\sqrt{\text{Hz}}$ at 10 Hz and 25 pT/ $\sqrt{\text{Hz}}$ at 100 Hz is achieved.

Published under license by AIP Publishing. <https://doi.org/10.1063/1.5140562>

Since, for the first time, White and Voltmer placed interdigital transducers (IDTs) onto a piezoelectric substrate for the generation of surface acoustic waves (SAW),¹ devices utilizing those have been thoroughly investigated as sensors for a plethora of quantities. These investigations include the sensing of gases,² pressure,³ temperature,⁴ humidity,⁵ biological molecules in liquids,^{6,7} magnetic fields,^{8–10} and many more. SAW sensors use the inverse piezoelectric effect to generate elastic waves by a high frequency voltage applied to IDTs on top of a piezoelectric substrate. In the delay line setup, the traveling wave is picked up by a second pair of IDTs and converted back into an electrical signal using the direct piezoelectric effect after propagating over a defined distance. A measurable phase change between output and input signals occurs upon an alteration of the wave velocity caused by an external influence. Love wave SAW sensors, which are composed of a piezoelectric substrate generating horizontal shear waves capped with a guiding layer confining the acoustic wave at the surface,¹¹ have been mostly investigated as biosensors;¹² only a few works focused on magnetic field applications.¹³ Magnetic field sensing with SAW devices

is based on the velocity change of the traveling acoustic waves due to a non-linear change of the elastic properties of a propagated magnetostrictive material with magnetic field induced magnetization, termed the ΔE effect.¹⁴ Several magnetic materials and SAW designs have been investigated over the years.^{15–18} Love type SAW sensors turned out to be the most promising candidates for the sensing of very low amplitude magnetic fields.^{8,10} This is mainly attributed to two properties of this type of sensor: first, the strong confinement of the acoustic energy at the sensor's surface by the acoustic wave guide layer, thus, changes on the surface have a higher impact on the wave velocity. Second, due to the predominantly horizontal shear displacement, Love waves are more sensitive to changes in the shear modulus of the propagated media. It was shown that the change in the shear modulus (ΔG) leads to a stronger effect compared to the change in Young's modulus (ΔE),¹⁹ consequently leading to higher sensitivities.

Amorphous, magnetostrictive thin films of composition (Fe₉₀Co₁₀)₇₈Si₁₂B₁₀ have been mainly used as the sensitive layer in magnetoelastic (ME) cantilever-style composites that are based on

silicon substrates.^{20,21} The deposition conditions, thermal treatment or anisotropy in general of magnetic films on piezoelectric substrates, however, were rarely discussed. Mathews *et al.* recently reported on the induction of an easy axis of magnetization by a post-deposition heat treatment of a Ni film on a 128° Y-cut LiNbO₃ based SAW device.²² Having a trigonal crystal structure quartz is highly anisotropic with regard to most of its properties, e.g., electrical and thermal conductivities, dielectric and piezoelectric constants, or coefficient of thermal expansion (CTE). Quartz has two linear CTEs: $\alpha_{11} = 14.3 \times 10^{-6} \text{ K}^{-1}$ parallel to the crystallographic X-axis and $\alpha_{33} = 7.8 \times 10^{-6} \text{ K}^{-1}$ parallel to the Z-axis. For rotated quartz cuts, the thermal expansion coefficient α'_{11} for any given direction in the YZ-plane can be calculated by the geometric relation,

$$\alpha'_{11} = \alpha_{11} \cdot \sin^2 \theta + \alpha_{33} \cdot \cos^2 \theta, \quad (1)$$

with θ being the angle between the surface normal and the Z-axis.²³ Accordingly, the thermally generated uniaxial stress σ_f in the FeCoSiB film can be estimated by

$$\sigma_f = E_f \cdot \varepsilon = E_f \cdot \Delta\alpha_s \cdot \Delta T, \quad (2)$$

with ΔT being the deviation from room temperature, E_f the Young's modulus of the film, ε the strain, and $\Delta\alpha_s = \alpha_{11} - \alpha'_{11}$ the resulting CTE of the substrate. On this basis, the stress induced anisotropy energy density K_σ of the FeCoSiB film can be derived by

$$K_\sigma = \frac{3}{2} \cdot \lambda_s \cdot \sigma_f, \quad (3)$$

where λ_s equals the isotropic saturation magnetostriction of the magnetic material.²⁴ In general, the uniaxial anisotropy energy density K_u of a magnetic material can be estimated by

$$K_u = \frac{H_k \cdot \mu_0 \cdot M_s}{2}, \quad (4)$$

with H_k being the anisotropy field, μ_0 the vacuum permeability, and M_s the saturation magnetization.

The presented SAW sensor [Fig. 1(a)] is based on a 500 μm thick ST-cut quartz substrate with the propagation direction being 90° to the crystallographic X-axis (Z'-axis). Cr (10 nm)/Au (300 nm)/Cr (10 nm) IDTs are deposited and structured by means of DC magnetron sputtering and standard photolithography, respectively. Operating in a delay line configuration, the sensor consists of two pairs

of split finger IDTs acting as in- and output transducers, each consisting of 25 pairs of 3.5 μm wide split fingers with a metallization ratio of 1. Hence, the periodicity of the IDTs is 28 μm corresponding to the wavelength of the acoustic waves at the sensor's synchronous frequency, which is between 147 and 148 MHz slightly varying from device to device [see Fig. 1(b)]. The SiO₂ guiding layer is deposited by means of plasma-enhanced chemical vapor deposition (PECVD), and the contact bonding pads are etched accessible utilizing inductively coupled plasma-reactive ion etching (ICP-RIE). More details regarding the fabrication process can be found in Ref. 8. The 8 nm/200 nm/5 nm thick Ta/(Fe₉₀Co₁₀)₇₈Si₁₂B₁₀/Ta layers are deposited by means of RF magnetron sputter-deposition in a parallel plate setup, and the delay line is structured via a subsequent lift-off process. Two types of depositions were performed. The first was performed by applying an external magnetic field of $H_{\text{ex}} = 180 \text{ Oe}$ at the position of the sensor delay line to induce a uniaxial magnetic anisotropy in the thin film parallel to the SAW propagation direction [see Fig. 1(a)]. The magnetic field was generated by two parallel orientated Nd₂Fe₁₄B permanent magnets with a size of 25 × 6 × 2 mm³ and a spacing of 20 mm. The second deposition was conducted without any external field (besides the omnipresent magnetron field of $\leq 25 \text{ Oe}$). However, both depositions were performed in cycles of 30 s of deposition and 300 s of cooling time with a deposition rate of 0.16 nm/s, ensuring that the substrate does not heat up above 40 °C to reduce uniaxial stress acting on the deposited film due to anisotropic thermal expansion of the quartz substrate. A post-deposition annealing at 270 °C for 30 min with subsequent cooling to room temperature in a strong external magnetic field $H_{\text{ex}} = 1300 \text{ Oe}$ is performed on the non-magnetic field deposited sample to also induce a uniaxial anisotropy parallel to the SAW propagation direction. Each sensor is mounted to a printed circuit board (PCB), and its impedance is matched to 50 Ω at both ports.²⁵ Scattering parameters were recorded using a vector network analyzer at magnetic saturation. Magnetic bias field dependent sensitivities of the SAW devices were measured using a Zurich Instruments UHFLLI lock-in amplifier for excitation and dynamic phase detection, while a 10 Hz sinusoidal magnetic field was applied with an amplitude of $\mu_0 H_{\text{AC}} = 100 \text{ nT}$. The magnetic fields during these measurements were provided by two solenoids. Phase noise measurements at the sensor's magnetic working points were conducted in a magnetically shielded chamber²⁶ and recorded using a Rohde & Schwarz FSWP phase noise analyzer. The magnetic DC bias fields for these measurements were provided by a potentiometer controlled low noise 6 V vintage car battery. Finally, magnetic hysteresis loops and domain images were recorded by means of large view magneto-optical Kerr effect (MOKE) microscopy.²⁷ The loops were recorded by averaging the MOKE image intensity over the whole delay line.

Figure 2(a) shows the obtained hysteresis loops of the non-magnetic field deposited FeCoSiB film before and after annealing in a magnetic field of 1.3 kOe and the magnetic field deposited film. All loops were measured perpendicular to the SAW propagation direction, which is the direction that the AC/DC fields are applied in any later measurements, and thus the direction of sensitivity. From the hysteresis loop and the MOKE microscopy image in Fig. 2(b), it can be seen that although no magnetic field was applied during the deposition, there is already an anisotropy in the FeCoSiB film indicated by the anisotropy field and the preferred domain orientation. Upon post-deposition cooling, a uniaxial compressive strain anisotropy

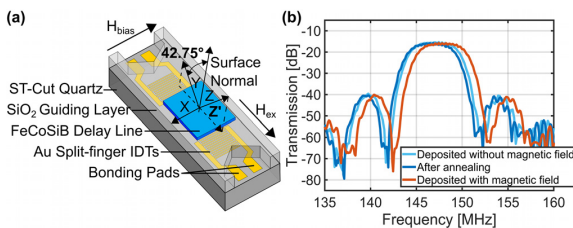


FIG. 1. (a) Schematic illustration of the fabricated SAW sensor. (b) Measured transmission characteristics (scattering parameter S_{21}) of two sensors. One deposited without a magnetic field before (light, blue) and after annealing (dark, blue). The second one was deposited with the present magnetic field (dark, red). All are measured in magnetic saturation.

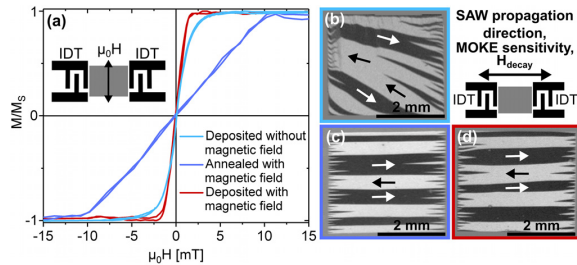


FIG. 2. Magnetic characterization of FeCoSiB films on quartz SAW devices. (a) Magnetic hysteresis loops taken from longitudinal magneto-optical Kerr effect (MOKE) contrast measured perpendicular to the SAW's propagation direction after deposition in a magnetic field of 180 Oe (dark, red), after deposition without a magnetic field (bright, blue) and after annealing in a magnetic field of 1.3 kOe (dark, blue). Magnetic domain images in the demagnetized state were taken from (b) the non-magnetic field deposited sample, (c) after annealing in a magnetic field, and (d) the film which was deposited in a magnetic field. The AC demagnetization field H_{decay} was applied along the SAW propagation direction before the images were taken. The gray area around the magnetic film is the non-magnetic SiO_2 layer.

perpendicular to the SAW propagation direction (X-axis) is acting on the film stemming from the lower CTE along the Z'-axis, i.e., less contraction takes place along this axis. Using Eqs. (1) and (2), the resulting stress acting along the X-axis can be calculated. With $E_{\text{FeCoSiB}} = 150 \text{ GPa}$, $\nu_{\text{FeCoSiB}} = 0.3$,²⁸ and $\Delta T = 13 \text{ K}$, the estimated resulting uniaxial stress acting on the FeCoSiB film during cooling is $\sigma_{\text{dep}} = 6 \text{ MPa}$, hence resulting in $K_{\sigma, \text{dep}} = 270 \text{ J/m}^3$ using Eq. (3) and $\lambda_s = 30 \text{ ppm}$.²⁹ Compared to $K_{u,1} = 1232 \text{ J/m}^3$ calculated from Eq. (4) with $M_s = 1.4 \text{ T}$ ²⁹ and $\mu_0 H_k = 2.2 \text{ mT}$ [taken from Fig. 2(a)], this is a small value, indicating that the anisotropy is not exclusively stress induced. After magnetic field annealing, the anisotropy field is increased strongly to $\mu_0 H_k = 10 \text{ mT}$. As can also be seen from Fig. 2(c), the magnetic film possesses a well-defined uniaxial anisotropy, confirmed by the pronounced domain alignment along the SAW propagation direction. Applying the above calculations to this case, $K_{\sigma, \text{ann}} = 4995 \text{ J/m}^3$ is obtained with $\Delta T = 247 \text{ K}$. This result is in the range of the calculated uniaxial anisotropy $K_{u,2} = 5600 \text{ J/m}^3$, indicating that the anisotropy is mostly thermally induced. Due to the high thermally induced stress, anisotropy is increased, therefore requiring a high field for magnetization reversal. The film deposited with an external magnetic field present shows the softest magnetic behavior with $\mu_0 H_k = 1.5 \text{ mT}$. The MOKE image in Fig. 2(d) shows that a precise orientation of domains parallel to the SAW propagation direction was achieved deviating only by up to 2° from ideal 90° orientation. This orientation of the easy axis of magnetization to the applied field, a 90° rotation of domains, leads to high magnetostriction³⁰ and consequently to a high ΔE effect.¹⁴ In contrast to the annealed film, a much lower induced anisotropy energy $K_{u,3} = 840 \text{ J/m}^3$ persists. However, the orientation of uniaxial anisotropy is similar in these two cases as can be seen from the alignment of the respective magnetic domains. Since the thermally induced $K_{\sigma, \text{dep}} = 378 \text{ J/m}^3$ is quite low, the applied magnetic field is dominating during the deposition process.

The sensitivities (phase change per unit of magnetic field) of the SAW devices with the three different magnetic films are shown in Fig. 3 as a function of DC bias fields applied perpendicular to the

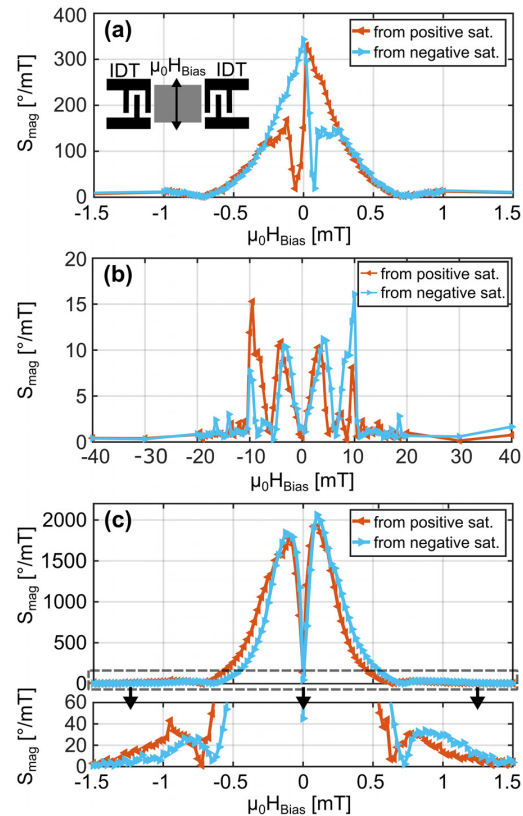


FIG. 3. Measured sensitivities as a function of applied DC bias field of devices (a) without magnetic field deposited FeCoSiB, (b) after annealing in an external magnetic field, and (c) with magnetic field deposited FeCoSiB. Also shown in (c) is the range from 0 to $60^\circ/\text{mT}$. Note the different $\mu_0 H_{\text{bias}}$ -axis range in (b).

SAW propagation direction. All three curves show local maxima at which the incremental change in elastic modulus is the highest, and thus, also, the slope of the signal's phase is maximized. The non-magnetically treated device [Fig. 3(a)] shows its highest sensitivity of $340^\circ/\text{mT}$ at $\mu_0 H_{\text{bias}} = 0 \text{ mT}$ coming from negative saturation (-10 mT). Coming from positive saturation ($+10 \text{ mT}$), approximately the same value is achieved due to the high symmetry of the curves. However, each curve shows non-symmetry around 0 bias field, which is a direct consequence of the tilted magnetic anisotropy axis in the film. Annealing the film strongly decreases the sensitivity of the device [Fig. 3(b)] to only a maximum value of $17^\circ/\text{mT}$ at $\mu_0 H_{\text{bias}} = 10 \text{ mT}$. This, on the one hand, can be attributed to the high anisotropy of the FeCoSiB film [Fig. 2(a)] after annealing, thus leading to a low piezomagnetic coefficient, which is defined as $\partial \lambda_s / \partial H$.²⁸ But it was also shown by Squire *et al.* that a softer magnetic material leads to a higher ΔG effect.³¹ In our case, the magnetoelastically induced phase change of the magnetic field deposited device is about 360° , while for the annealed device, it is only 24° . Therefore, an increase in the total phase

change by a factor of 15 is the consequence of the higher ΔG effect. As shown in Figs. 2(a) and 2(d), applying a magnetic field already during deposition leads to the highest sensitivities of up to $2000^\circ/\text{mT}$ at $\mu_0 H_{\text{bias}} = 0.1 \text{ mT}$ [Fig. 3(c)]. A precise orientation of uniaxial anisotropy with simultaneously low total anisotropy leads to the high sensitivity and also to the high symmetry of the curves. Also shown in Fig. 3(c) are the two outer maxima at the transition into saturation, which are about two orders of magnitude smaller than the two inner maxima. This indicates that the two curves in Figs. 3(b) and 3(c) are similar, also due to the similar domain alignment only varying in total sensitivity.

However, for the detection of very small magnetic fields not only the phase sensitivity is relevant, but also the generated phase noise from which the lowest detectable magnetic signal can be derived (limit of detection, LOD). Figure 4(a) shows the measured phase noise spectra for all three presented cases measured at bias fields at which the devices show their highest sensitivity. A characteristic $1/f$ noise regime can be observed in the range up to 10 kHz. This range is mainly dominated by magnetic noise believed to be stemming from domain wall activity adding up to 20 dB in noise compared to the magnetically saturated state.²⁵ The differences in phase noise between each device are, however, comparably low. Between the non-magnetic field and the magnetic field deposited samples, the difference in noise in the bio-magnetic relevant regime of 1–1000 Hz is only between 2 and 5 dB. This deviation in phase noise is still in the range of fluctuations, which were observed in a variety of fabricated Love wave devices that were investigated. Despite the increase in sensitivity, the phase noise is maintained constant. This is mirrored in the limit of detection (LOD) given in Fig. 4(b). Because of the very low sensitivity of the annealed device, its LOD is significantly higher than the other two over the whole frequency range. Before annealing, however, already a decent LOD of $280 \text{ pT}/\sqrt{\text{Hz}}$ at 10 Hz and $95 \text{ pT}/\sqrt{\text{Hz}}$ at 100 Hz is achieved. Deposition of the FeCoSiB film within a magnetic field leads, due to the high sensitivity to LODs of $70 \text{ pT}/\sqrt{\text{Hz}}$ at 10 Hz and $25 \text{ pT}/\sqrt{\text{Hz}}$ at 100 Hz.

In conclusion, the influence of the deposition process and post deposition treatment on the magnetic anisotropy in FeCoSiB thin films on quartz substrates and thus on the sensitivity of magnetic field

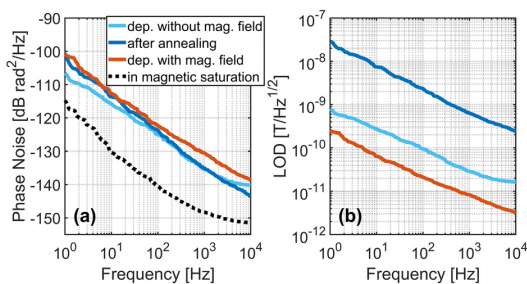


FIG. 4. (a) Measured phase noise floor and (b) calculated limit of detection as a function of the frequency from a carrier signal of SAW devices with magnetic films deposited without any magnetic field (light, blue), after annealing the same sample (dark, blue), and deposited with a magnetic field present (dark, red). Also shown in (a) is one sensor measured while magnetically saturated (dashed, black).

Love wave SAW sensors was investigated in this report. Three different preparation conditions were compared, revealing that post-deposition annealing drastically reduces the sensitivity of the device. This reduction is due to a high thermally induced magnetic anisotropy stemming from anisotropic coefficients of thermal expansion of the quartz substrate. However, applying a low temperature deposition process in combination with a magnetic field yields very high sensitivities up to $2000^\circ/\text{mT}$ attributed to the low but well aligned magnetic anisotropy in the film. The phase noise of these devices was not influenced, but is strongly dominated by magnetic noise requiring more advanced magnetic multilayers for further improvement of the LOD.³²

The authors would like to thank the German Research Foundation (Deutsche Forschungsgemeinschaft, DFG) who funded this work through the collaborative research center CRC 1261 “Magnetolectric Sensors: From Composite Materials to Biomagnetic Diagnostics.”

REFERENCES

- R. M. White and F. W. Voltmer, *Appl. Phys. Lett.*, **7**, 314 (1965).
- L. Rana, R. Gupta, M. Tomar, and V. Gupta, *Sens. Actuators, B* **252**, 840 (2017).
- H. Scherr, G. Scholl, F. Seifert, and R. Weigel, *IEEE Ultrasonics Symposium Proceedings* (1996), p. 347.
- L. Reindl, I. Shrena, S. Kenshil, and R. Peter, in *Proceedings of the 2003 IEEE International Frequency Control Symposium and PDA Exhibition Jointly with the 17th European Frequency and Time Forum* (2003), p. 935.
- C. Caliendo, E. Verona, A. D’Amico, A. Furlani, G. Iucci, and M. V. Russo, *Sens. Actuators, B* **16**, 288–292 (1993).
- M. D. Schlensog, T. M. A. Gronewold, M. Tewes, M. Famulok, and E. Quandt, *Sens. Actuators, B* **101**, 308 (2004).
- A. Malave, U. Schlecht, T. M. A. Gronewold, M. Perpeet, and M. Tewes, *IEEE Sens.* **2006**, 604–607 (2006).
- A. Kittmann, P. Durdaut, S. Zabel, J. Reermann, J. Schmalz, B. Spetzler, D. Meyners, N. X. Sun, J. McCord, M. Gerken, G. Schmidt, M. Höft, R. Knöchel, F. Faupel, and E. Quandt, *Sci. Rep.* **8**, 278 (2018).
- V. Polewczyk, K. Dumesnil, D. Lacour, M. Moutaouekkil, H. Mjahed, N. Tiercelin, S. Petit Watelot, H. Mishra, Y. Dusch, S. Hage-Ali, O. Elmazria, F. Montaigne, A. Talbi, O. Bou Matar, and M. Hehn, *Phys. Rev. Appl.* **8**, 024001 (2017).
- X. Liu, B. Tong, J. Ou-Yang, X. Yang, S. Chen, Y. Zhang, and B. Zhu, *Appl. Phys. Lett.* **113**, 082402 (2018).
- B. Jakoby and M. J. Vellekoop, *Smart Mater. Struct.* **6**, 668 (1997).
- M.-I. Rocha-Gaso, C. March-Iborra, A. Montoya-Baides, and A. Arnau-Vives, *Sensors* **9**, 5740 (2009).
- M. Inoue, N. Fujita, and T. Fujii, *J. Appl. Phys.* **73**, 6159 (1993).
- A. Ludwig and E. Quandt, *IEEE Trans. Magn.* **38**, 2829 (2002).
- D. C. Webb, D. W. Forester, A. K. Ganguly, and C. Vittoria, *IEEE Trans. Magn.* **15**, 1410 (1979).
- M. Yamaguchi, K. Hashimoto, H. Kogo, and M. Naoe, *IEEE Trans. Magn.* **16**, 916 (1980).
- S. M. Hanna, *IEEE Trans. Ultrason., Ferroelectr., Freq. Control* **34**, 191 (1987).
- M. Kadota, S. Ito, Y. Ito, T. Hada, and K. Okaguchi, *Jpn. J. Appl. Phys., Part 1* **50**, 07HD07 (2011).
- Z. Sárközi, K. Mackay, and J. C. Peuzin, *J. Appl. Phys.* **88**, 5827 (2000).
- H. Greve, E. Woltermann, H.-J. Quenzer, B. Wagner, and E. Quandt, *Appl. Phys. Lett.* **96**, 182501 (2010).
- B. Tong, X. Yang, Z. Guo, K. Li, J. Ouyang, G. Lin, and S. Chen, *Ceram. Int.* **39**, 6853 (2013).
- S. A. Mathews, N. S. Bingham, R. J. Suess, K. M. Charipar, R. C. Y. Auyeung, H. Kim, and N. A. Charipar, *IEEE Trans. Magn.* **55**, 1 (2019).

- ²³V. E. Bottom, *Introduction to Quartz Crystal Unit Design* (Van Nostrand Reinhold Company, New York, 1982).
- ²⁴B. D. Cullity and C. D. Graham, *Introduction to Magnetic Materials* (John Wiley & Sons, Inc., Hoboken, New Jersey, 2009).
- ²⁵P. Durdaut, A. Kittmann, E. Rubiola, J.-M. Friedt, E. Quandt, R. Knochel, and M. Hoft, *IEEE Sens. J.* **19**, 8000 (2019).
- ²⁶R. Jahns, H. Greve, E. Woltermann, E. Lage, E. Quandt, and R. Knöchel, in 2011 IEEE International Workshop on Medical Measurements and Applications Proceedings (2011), p. 107.
- ²⁷J. McCord, *J. Phys. D: Appl. Phys.* **48**, 333001 (2015).
- ²⁸E. Lage, C. Kirchof, V. Hrkac, L. Kienle, R. Jahns, R. Knöchel, E. Quandt, and D. Meyners, *Nat. Mater.* **11**, 523 (2012).
- ²⁹P. Hayes, M. Jovičević Klug, S. Toxværd, P. Durdaut, V. Schell, A. Teplyuk, D. Burdin, A. Winkler, R. Weser, Y. Fetisov, M. Höft, R. Knöchel, J. McCord, and E. Quandt, *Sci. Rep.* **9**, 16355 (2019).
- ³⁰A. Ludwig and E. Quandt, *J. Appl. Phys.* **87**, 4691 (2000).
- ³¹P. T. Squire, D. Atkinson, and S. Atalay, *IEEE Trans. Magn.* **31**, 1239 (1995).
- ³²M. Jovičević Klug, L. Thormählen, V. Röbisch, S. D. Toxværd, M. Höft, R. Knöchel, E. Quandt, D. Meyners, and J. McCord, *Appl. Phys. Lett.* **114**, 192410 (2019).

3.2 Sputter Deposited Magnetostrictive Layers

The deposition time of soft magnetic FeCoSiB on quartz is more than 4 hours for 200 nm, due to the need of cooling breaks between deposition periods of 30 s [Kit20, Tho17]. In preliminary experiments by Thormählen it was found out that applying a DC bias instead of an RF bias during magnetron sputtering, leads to lower heating of the substrate. Therefore, the ratio of deposition time to cooling breaks can be reduced. In this publication the same magnetic properties are achieved via DC sputtering, as well as the same sensor performance, while reducing the total deposition time. Due to the analogousness of the deposited films, the sensitivities exhibited by SAW sensors are similar as well. Therefore, under the given circumstances the sensor performance is not restricted by the type of bias used during deposition.

Author Contributions

Own contribution to the manuscript:

- Fabrication of samples (shared)
- Measurements of samples (shared)
- Designing experiments (shared)
- Data analysis (shared)
- Interpretation of the results (shared)
- Preparation of figures (shared)
- Writing of the manuscript (shared)

Reproduced from *Sensors* **21(24)**, 8386 (2021); DOI: 10.3390/s21248386.



Article

Sputter Deposited Magnetostrictive Layers for SAW Magnetic Field Sensors

Lars Thormählen ^{1,*}, Dennis Seidler ¹, Viktor Schell ¹, Frans Munnik ², Jeffrey McCord ¹ and Dirk Meyners ¹

¹ Institute for Materials Science, Kiel University, Kaiserstraße 2, 24143 Kiel, Germany; dese@tf.uni-kiel.de (D.S.); visc@tf.uni-kiel.de (V.S.); jmc@tf.uni-kiel.de (J.M.); dm@tf.uni-kiel.de (D.M.)

² Institute of Ion Beam Physics and Materials Research, Helmholtz-Zentrum Dresden-Rossendorf (HZDR), 01328 Dresden, Germany; f.munnik@hzdr.de

* Correspondence: lath@tf.uni-kiel.de

Abstract: For the best possible limit of detection of any thin film-based magnetic field sensor, the functional magnetic film properties are an essential parameter. For sensors based on magnetostrictive layers, the chemical composition, morphology and intrinsic stresses of the layer have to be controlled during film deposition to further control magnetic influences such as crystallographic effects, pinning effects and stress anisotropies. For the application in magnetic surface acoustic wave sensors, the magnetostrictive layers are deposited on rotated piezoelectric single crystal substrates. The thermomechanical properties of quartz can lead to undesirable layer stresses and associated magnetic anisotropies if the temperature increases during deposition. With this in mind, we compare amorphous, magnetostrictive FeCoSiB films prepared by RF and DC magnetron sputter deposition. The chemical, structural and magnetic properties determined by elastic recoil detection, X-ray diffraction, and magneto-optical magnetometry and magnetic domain analysis are correlated with the resulting surface acoustic wave sensor properties such as phase noise level and limit of detection. To confirm the material properties, SAW sensors with magnetostrictive layers deposited with RF and DC deposition have been prepared and characterized, showing comparable detection limits below 200 pT/Hz^{1/2} at 10 Hz. The main benefit of the DC deposition is achieving higher deposition rates while maintaining similar low substrate temperatures.

Keywords: magnetron sputter deposition; FeCoSiB; ERDA; XRD; film stress; magnetic field sensor; magnetic properties; magnetic domains; SAW



Citation: Thormählen, L.; Seidler, D.; Schell, V.; Munnik, F.; McCord, J.; Meyners, D. Sputter Deposited Magnetostrictive Layers for SAW Magnetic Field Sensors. *Sensors* **2021**, *21*, 8386. <https://doi.org/10.3390/s21248386>

Academic Editor: Michael Kraft

Received: 1 November 2021

Accepted: 9 December 2021

Published: 15 December 2021

Publisher's Note: MDPI stays neutral with regard to jurisdictional claims in published maps and institutional affiliations.



Copyright: © 2021 by the authors. Licensee MDPI, Basel, Switzerland. This article is an open access article distributed under the terms and conditions of the Creative Commons Attribution (CC BY) license (<https://creativecommons.org/licenses/by/4.0/>).

1. Introduction

Surface acoustic wave (SAW) devices constitute a multifunctional sensor concept [1]. The use of different piezoelectric substrates and crystallographic orientations allows the excitation of various types of surface acoustic waves, like seismic waves such as Rayleigh waves or shear horizontal waves called Love waves. Depending on the different surface waveforms, sensors can be used for different measurement applications such as biological molecule detection [2,3] and temperature [4]. A large area of application for SAW sensors is a magnetic field sensor [4–8] and a tabular comparison can be found in the Appendix A (see Table A1). The sensors are based on various substrates and magnetic sensitive layers. Typical substrates are St-cut Quartz in different cutting directions, LiNbO₃ and LiTaO₃ [2–12]. In that context, a wide range of ferromagnetic materials are used for the magnetic sensitive layer, e.g., FeCo, FeGa, Fe₂Tb and (Fe₉₀Co₁₀)₇₈Si₁₂B₁₀ (FeCoSiB) [10–12], which are deposited on the SAW sensor as full films, multilayers or patterned structures [12–14]. The variety of magnetic layers display different magnetic behavior, which is strongly correlated to the magnetic anisotropies of the magnetic films. Controlling and adapting these for the respective layer system and utilizing them is one of the major challenges in the development of these magnetic systems for SAW devices. The shown research is based on ST-cut quartz SAW devices with a full film FeCoSiB layer based on

previous studies [5,8,9] with a focus on the deposition process of the magnetic sensitive layer with regard to material composition, magnetic anisotropy, film stress, amorphicity and overall sensor performance.

In general, the working principle of SAW sensors is the generation of elastic waves based on the inverse piezoelectric effect by applying a high frequency voltage to interdigital transducers (IDT) deposited on a piezoelectric substrate.

As mentioned before, the Love wave sensors utilize horizontal shear waves. The waves propagate along a delay line while the wave energy is concentrated at the sensor's surface by a guiding layer. To allow external influences to affect the sensor, it can be equipped with an additional functional layer on the delay line. For the purpose of magnetic field sensing, this functional layer consists of a magnetostrictive material. External magnetic fields cause the magnetostrictive material to change the effective shear and young's modulus, affecting the velocity of transmitted Love waves in the guiding layer. Using opposite output IDTs, the voltage generated in the piezoelectric material by the transmitted and influenced shear wave is recorded and the phase change between input and output signal serves as a measure of the applied magnetic field. In this case, a magnetostrictive layer was deposited from a magnetron sputter target with the composition $(\text{Fe}_{90}\text{Co}_{10})_{78}\text{Si}_{12}\text{B}_{10}$ (FeCoSiB) on top of the delay line. The general characteristics of the used sensor concept are shown in ref Kittmann et al. [5].

In previous studies, it was shown that the preparation of a magnetostrictive layer presents a particular challenge in terms of control of magnetic anisotropy and magnetic domain structure [8]. Although methods exist to subsequently adjust the magnetic anisotropy of the film by means of heat treatments, these cannot be directly transferred to quartz substrates. Unlike silicon (100)-based magnetostrictive film sensors, quartz substrates for SAW applications exhibit anisotropic thermal expansion, resulting in uniaxial film stress in the magnetostrictive layer with thermal load. As a result, these (uniaxial) film stresses contribute directly to the effective magnetic anisotropy in these films [15]. To minimize the effects of film stress, changes due to anisotropic thermal expansion, deposition processes have to be adapted to quartz to reduce the substrate temperature during deposition. On the other hand, film stress generated by the deposition can be beneficially utilized to influence the magnetic properties of the magnetostrictive film. By introducing an additional stress anisotropy to the induced magnetic anisotropy, it is possible to imprint an improved alignment of the magnetic anisotropy and, thus, the magnetic domain structure in soft magnetic material [16].

One of the most commonly used magnetron sputtering methods is based on radio frequency (RF) sputter operation which has the advantage that thicker magnetic target materials with strong magnetron fields can be used. For this reason, it is possible to use the powder-sintered material FeCoSiB, as the manufacturing process and machining of the target material requires a base thickness of several millimeters. However, the method has a high energy input on the substrate and the resulting deposition rates are low. To compensate for exhibited substrate heating, complex and expensive methods for sample cooling must be applied. As an alternative, cooling phases with plasma interruption were added to the deposition process [8,9].

This publication investigates the application of direct current (DC) deposition for magnetostrictive layer preparation on quartz substrates with the aim of reducing the energy input into the substrate and increasing the deposition rate. To enable DC operation, a magnetically adapted FeCoSiB target is used. An important aspect is the chemical composition of the resulting thin films. The soft-magnetic behavior of FeCoSiB depends on the concentration of silicon and boron atoms, which serve as glass formers between iron and cobalt [17]. The use of these elements makes the sputter-deposited layers amorphous and by this eliminates magneto-crystalline anisotropy effects on the magnetic properties. It must therefore be ensured that despite the change of deposition mode, the composition of the films is unaffected so that the film structure remains amorphous. These amorphous magnetic films show good soft-magnetic properties [18] together with a high magnetostrictive

tive response, as desired for use in SAW-based magnetic field sensors. It will be shown that a changeover to DC deposition enables significantly higher deposition rates without a significant alteration in structural and magnetic properties, as well as in SAW sensor performance. For this purpose, the chemical, structural and magnetic properties of DC and RF with different sputter pressure-deposited FeCoSiB films are investigated. The corresponding SAW sensor performance with RF and DC deposited magnetic films is compared in terms of sensitivity and noise.

2. Materials and Methods

The required magnetostrictive FeCoSiB layers for the experiments are deposited in a VonArdenne CS730S sputtering system. The system has nine planar magnetron sputter sources and allows the deposition of materials as adhesion or passivation layers without breaking the vacuum. FeCoSiB depositions are performed from a multi-element target with 99.95% purity and at constant power for RF and DC of 200 W with argon gas flow of 40 sccm. The chamber pressure is varied for the depositions in the range of 1.0×10^{-3} mbar to 1.0×10^{-2} mbar with a step size of 1.0×10^{-3} mbar. The depositions cannot be performed in one cycle. Deposition time limits are necessary to keep the energy input into the sample and the resulting sample temperature low to minimize thermal expansion-induced film stress. Depending on the chamber pressures, deposition times are adjusted to deposit 5 nm FeCoSiB by RF mode and 20 nm FeCoSiB by DC mode. As a result, for the preparation of in total 200 nm thick FeCoSiB layers, 40 cycles and 10 cycles are run for RF and DC, respectively. To ensure that the maximum temperature of the substrate does not exceed 30 °C, cooling breaks of 300 s (RF) and 180 s (DC) are introduced between deposition cycles. As an additional measure, 2 mm thick AlO₂ spacers are placed below the samples to thermally decouple the SAW substrate from the aluminum sample carrier.

For the fabrication of FeCoSiB layers on SAW substrates with a thickness of 200 nm, the Ar pressure is chosen to achieve a compressive film stress of 200 MPa. Thus, for an Ar pressure of 2.5×10^{-3} mbar, the rate for RF is 0.16 nm/s with a cycle sequence of 30 s deposition time and 300 s deposition pause. For DC, on the other hand, with a chamber pressure of 2.0×10^{-3} mbar, the rate is 0.4 nm/s with a cycle sequence of 50 s deposition/180 s cooling. As a result, the total processing time is reduced from approx. 4.5 h for RF to 1.5 h for DC for the aimed FeCoSiB thickness. A uniaxial magnetic anisotropy is induced in the films parallel to the SAW propagation direction by applying a static permanent magnetic field of $\mu_0 H_{\text{dep}} = 70$ mT during film deposition (see Figure 1). This field is generated by two parallel aligned Nd₂Fe₁₄B permanent magnets with dimensions of 25 mm × 6 mm × 2 mm. The magnets are connected by an iron yoke to increase the strength and homogeneity of the generated magnetic field. The magnet is used for all depositions.

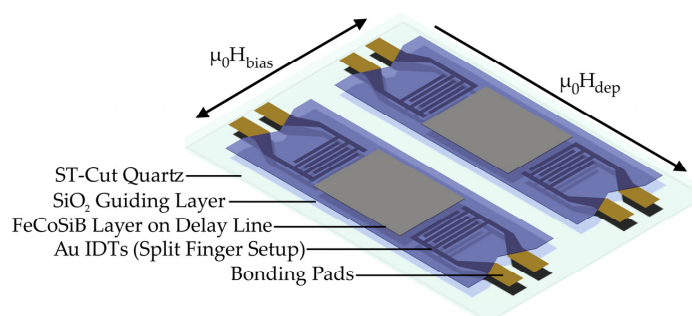


Figure 1. Schematic drawing of a SAW chip in use with two SAW delay line sensors, each with an independent guide layer. For magnetic anisotropy imprinting a magnetic field $\mu_0 H_{\text{dep}}$ is used during deposition of the magnetic layer FeCoSiB. The sensors are operated with $\mu_0 H_{\text{bias}}$ at the magnetic operating point during sensor operation.

The deposited FeCoSiB films are chemically characterized by elastic recoil detection analysis (ERDA) [19], which enables the detection of light elements in a heavy element matrix. For the chemical analysis, 10 mm × 10 mm silicon substrates (100) with native oxide are used. These substrates are coated with a stack of 5 nm Cr/400 nm FeCoSiB/10 nm Ta. Here, chromium serves as an adhesion promoter. Tantalum is used for surface passivation to prevent early corrosion of the FeCoSiB. The ERDA measurements are performed with a Cl^{7+} ion beam and two different energies of 43 MeV and 35 MeV. The angle of incidence on the film is 75° with respect to the normal sample. The irradiated film area has a size of 2 mm × 2 mm. The scattered Cl ions and recoiled target atoms are detected at an angle of 30° with a Bragg ionization chamber (BIC), which allows the energy and the atomic number to be determined. The last is necessary to identify the particle. To measure the total energy, the particles must be stopped completely in the BIC, which is filled with isobutane at a pressure of 125 mbar. This pressure is optimal for the measurement of recoil atoms of C to P and scattered Cl ions produced by a beam energy of 43 MeV. Because the recoil B atoms are light and have a long-range, a separate measurement with a beam energy of 35 MeV has been performed, which is sufficiently low for the B atoms to be completely stopped in the detector. The output of the BIC detector is a 2D-histogram where the number of particles is displayed as a function of energy and Bragg peak signal [20]. In this 2D plot, the elements can be identified in branches, detaching from the main branch of scattered Cl ions. The analysis depth for the recoil atoms is based on where the recoil branch detaches from the main branch and it is highest for atoms with low atomic number (Z). For Si, the analysis depth is relatively low as can be observed in the depth profiles (Section 3.1). H recoil atoms have been detected with a separate solid-state detector at a scattering angle of 40°. This detector is preceded by a 25 μm Kapton foil to stop scattered ions and heavy recoil ions. The depth resolution of this system is reduced because of energy loss straggling in the foil. A separate detector is needed because the range of the H atoms is too large to stop in the BIC detector. The processing of the measured spectra and calculation of elemental depth profiles is performed using NDF v9.3g [21].

As described, B and Si serve as glass formers and prevent the formation of crystalline iron-cobalt phases. Provided that enough of the glass formers is incorporated, an amorphous film structure is expected to form during sputter deposition. To investigate the structure by X-ray diffraction (XRD) method, samples are prepared from silicon (100) substrates with native surface oxide. The sample size is 15 mm × 15 mm to avoid beam overspill. The substrates are coated by 10 nm Ta/200 nm FeCoSiB. These layers are patterned by lithography and lift-off process to create a circular FeCoSiB layer with an area of 150 mm². No passivation layer is used for the XRD measurements, which are executed timely after layer deposition. To examine for the X-ray amorphous state, a Rigaku Smartlab 9 kW XRD tool is operated in grazing incidence (GIXRD) geometry. Generating Cu $K\alpha_1$ and $K\alpha_2$ radiation, the source is run at a power setting of 200 mA and 45 kV. The resulting diffraction patterns are recorded with a 2D detector.

Another important aspect when considering the magnetic performance on the SAW sensors is the film stress of the magnetostrictive layer. For the determination of the respective film stress, cantilevers made of “UPILEX-S®” in a size of 25 mm × 2.5 mm × 50 μm are used. The cantilevers are coated with a 10 nm layer of Ta before magnetic coating and reference measurement, to improve adhesion and reflection properties. The bending of the cantilevers before and after deposition of 200 nm FeCoSiB at varying chamber pressures is recorded and evaluated using a Keyence VK100 laser confocal microscope. The Stoney equation [22] is used to calculate the resulting film stresses. In order to investigate the influence of film stress on the imprinting of magnetic anisotropy by the external magnetic field, additional magnetic analysis samples based on 10 mm × 10 mm silicon (100) substrates with native oxide are prepared for magnetic property investigations. These samples are coated with the layer system 10 nm Ta/200 nm FeCoSiB/10 nm Ta. In this case, the Ta layers act as adhesion promoter and passivation layer, respectively. The deposition of

FeCoSiB for the RF and DC samples is performed at the deposition pressures between 2×10^{-3} mbar and 1×10^{-2} mbar.

The SAW sensors used for this work are based on the above-mentioned ST-Cut quartz and have two SAW sensors with independent delay line on a sensor chip of size $14 \text{ mm} \times 8.9 \text{ mm}$. The single sensors have two pairs of split finger IDTs with a periodicity of $28 \text{ }\mu\text{m}$ and Figure 2 shows the scattering parameters (S_{12} and S_{21}) for a sensor used in this publication. The center frequency is at 142.5 MHz. All sensors investigated show similar scattering parameters in the range between 141 MHz and 146 MHz. The variance of the center frequency is due to thickness differences in the SiO_2 wave guiding layer.

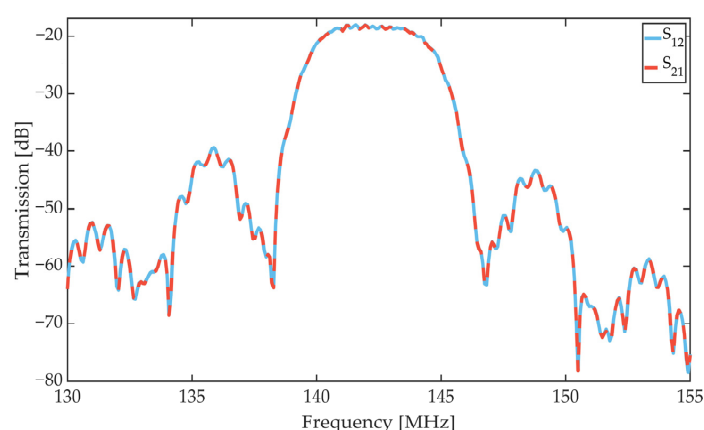


Figure 2. Scattering parameters (S_{12} and S_{21}) of an SAW sensor used in this publication measured in magnetic saturation. The center frequency of the Love wave device is at 142.5 MHz.

The design and fabrication of the SAW sensors has been described in detail in publications [5,8]. To evaluate the sensor properties, the SAW sensors are mounted on printed circuit boards (PCB) and the impedance of input and output is matched to 50 ohm. The measurements are performed using a Zurich Instruments UHFIL lock-in amplifier, a vector network analyzer and a Rohde and Schwarz FSWP phase noise analyzer in a shielded chamber [23,24]. Scattering parameters, magnetic sensitivity and phase noise are measured. A more detailed description of the measurement procedure can be found in Schell et al. [8]. The cross-sensitivity to temperature of SAW sensors is well known and can be mitigated by using a second SAW device without magnetostrictive coating for compensation [25,26]. In the experiments presented here with a focus on the influence of the magnetic layer, the temperature in the lab environment was kept constant and a compensation method was not applied. An additional approach to reduce these influences on ST-Cut quartz resonators is shown in Mishra et al. [27].

For a better understanding of the magnetic layer behavior of the fabricated SAW magnetic field sensors, large view magneto-optical Kerr effect (MOKE) microscopy investigations are performed [28]. The large view microscope has the ability to image the entire delay line and capture the magnetization loops and magnetic domain images, also on the device level. For this purpose, the above-mentioned magnetic analysis samples, as well as the magnetic SAW sensors, were considered. Magnetic domain images are taken in the demagnetized state and around the devices' working points to analyze the orientation of the magnetic domains and their overall domain structure. To investigate the magnetic behavior in more detail, longitudinal and transversal magnetization loops of the device samples were measured with the application of magnetic field parallel and perpendicular to the imprinting field $\mu_0 H_{\text{dep}}$ in the MOKE microscope. The magnetic hysteresis losses are extracted from the magnetization loops obtained for films with different conditions of film depositions.

3. Results

3.1. Chemical and Structural Analysis

The ERDA depth profiles of DC (a) and RF (b) deposited FeCoSiB layers in Figure 3 show the elemental distributions in at.% as a function of profile depth in at/cm². Based on the estimated densities of the measured elements, an overall measurement depth of 420 nm (equal to 3526 at/cm²) can be assumed. In Figure 3, the depth profiles recorded at accelerator energies 43 MeV and 35 MeV for a depth of 120 nm are merged for the measured elements iron (Fe), cobalt (Co), silicon (Si), oxygen (O), carbon (C), boron (B) and hydrogen (H).

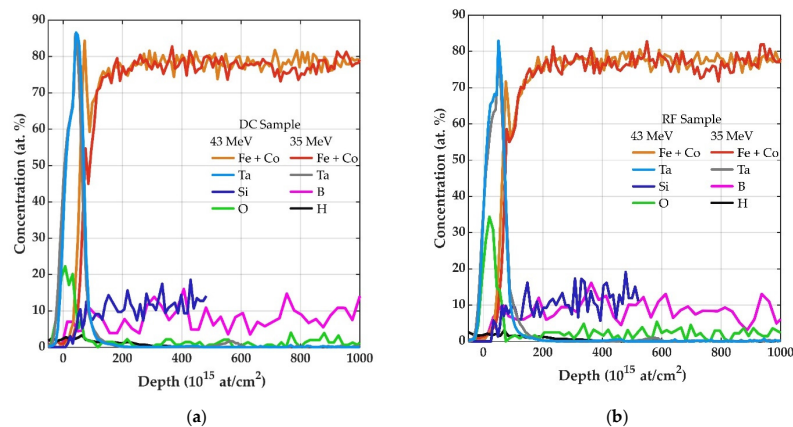


Figure 3. (a,b) ERDA depth profile of FeCoSiB deposited with DC and RF. The samples consist of a 5 nm Cr/400 nm FeCoSiB/10 nm Ta layer. The tantalum layer serves as a protection layer to prevent oxidation. The displayed measurement depth range corresponds to approximately 120 nm. As indicated, two different accelerating voltages 43 MeV and 35 MeV were used to obtain optimal results for all elements.

The concentration data are derived from the measured ERDA and CI scattering spectra and have been calculated using NDF v9.3g. A special case arises for the elements Fe and Co. Due to their similar masses, Fe and Co signals cannot be differentiated from each other and are therefore summed. The uncertainty of the determined elemental concentration of the performed measurement is in the 1 at.% range for the elements (Fe+Co), Si and B. Due to the low amounts of oxygen, carbon and hydrogen (close to the detection limit) the relative error of O content is 10% and 20–30% for C and H. Furthermore, the depth profiles are convoluted by the system resolution, physical effects such as straggling and isotope distribution for B, and also by the statistical fluctuations of the spectra [19].

From the elemental depth profiles, it can be concluded that the 10 nm thick Ta top layer has sufficient oxidation resistance and can prevent deep penetration of O. The concentration of O drops sharply with penetration depth, falling within the Ta layer to a low amount of about 2 at.%, which remains constant till the end of the depth profile. Apparently, O is incorporated into the film during deposition. Possible oxygen sources include chamber leakage, sputter gas impurities, and the use of powder-sintered target material. The last one is assumed to be the most likely source due to the manufacturing method of powder-sintered targets. Furthermore, it can be seen in Figure 3 that in both deposition cases the element distribution after the Ta top layer is constant. This provides information that no measurable compositional variation is formed by the pause times between the deposition cycles for DC and RF and the FeCoSiB grows as a continuous film. The origin of the elements C and H are assumed to be due to a residual gas content in the deposition chamber. Furthermore, manufacturing and processing of the FeCoSiB target for the magnetic adaption could cause the incorporation of the detected C impurities.

However, it should be noted that the configuration of the ERDA setup with BIC was chosen to enable the detection of the target elements, whereas the Ar detection requires a configurational change. To improve the mass separation between Ar atoms and Cl ions, ERDA can be used with a time-of-flight analysis system (ToF). Additional ToF-ERDA experiments reveal an upper limit of 0.5 at.% for the Ar concentration in the FeCoSiB layers. The elemental concentrations averaged across the measured FeCoSiB cross-sections are summarized in Table 1.

Table 1. Averaged elemental concentrations calculated from the FeCoSiB depth profile for an RF and DC sample deposited from a target material with a nominal composition of $(\text{Fe}_{90}\text{Co}_{10})_{78}\text{Si}_{12}\text{B}_{10}$.

Sample	Fe+Co (at.%)	Si (at.%)	O (at.%)	C (at.%)	B (at.%)	H (at.%)
RF	77.4	11.4	2.32	0.44	8.40	0.075
DC	78.2	12.0	1.63	0.52	7.63	0.056

Fe and Co together reach a proportion of about 78 at.%, which equals the content in the sputter target with the nominal composition of $(\text{Fe}_{90}\text{Co}_{10})_{78}\text{Si}_{12}\text{B}_{10}$. Si also reaches the target value of 12 at.%. B, on the other hand, deviates from the desired concentration of 10 at.% by more than 1 at.%. Within the mentioned measurement error, the ERDA measurements reveal the same elemental concentrations for both deposition methods RF and DC.

The structural analysis was performed by XRD as described above. Figure 4 shows the measured X-ray intensities of the two FeCoSiB films deposited by RF (DC) mode at a pressure of 2.5×10^{-3} mbar (2.0×10^{-3} mbar). The XRD spectra show two broad and smaller diffractions at 2 Theta equal to 34° and 39° , which originate from the buried Ta layer. The Ta adhesion promoter is still measurable due to the GIXRD penetration depth of more than 200 nm. Due to the low intensity, it is not possible to determine any precise information about the Ta structure. We assume a nanocrystalline or an amorphous structure. An amorphous structure was reported for thin tantalum layers prepared by magnetron sputter deposition [29]. The third reflex, and largest, extends around 44° . In this 2 Theta range, diffraction peaks can emerge from Fe at 44.77° , Co at 47.69° and FeCo at 44.97° . It is assumed that the main source of the signal is the high amount of Fe in the film. Broad and low-intensity distributions are measured in this 2 Theta range for possible Fe and Co signals. No further peaks are exhibited. Based on the results of the GIXRD, it can be assumed the amorphous FeCoSiB quality is the same, regardless of RF or DC deposition mode.

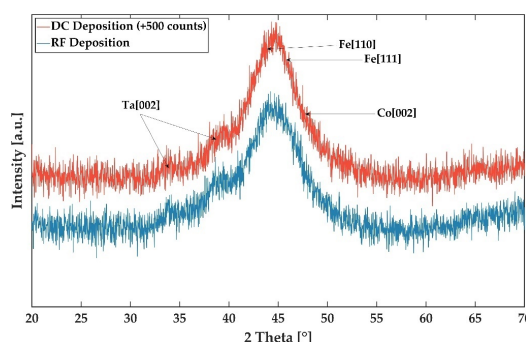


Figure 4. XRD result of Ta/FeCoSiB thin films deposited by RF and DC mode at 2.5×10^{-3} mbar and 2.0×10^{-3} mbar, respectively. For both deposition processes, the power was set to 200 W at an Ar flow of 40 sccm. Grazing incidence XRD was used with 2 Theta ranging from 20° to 70° with steps of 0.25° . For a better representation, an offset for the XRD result for the thin film deposited by DC mode was used. The adhesion promoter tantalum and a signal combination of the amorphous FeCoSiB are noticeable.

3.2. FeCoSiB Film Stress and Magnetic Behavior

After it has been demonstrated that both deposition methods DC and RF lead to the same layer composition and structure, the control of film stress and imprinted magnetic anisotropy become important parameters for the following magnetic samples and SAW sensors. The film stresses determined for this purpose are shown in Figure 5 as a function of Ar deposition pressure for RF and DC sputter deposition conditions.

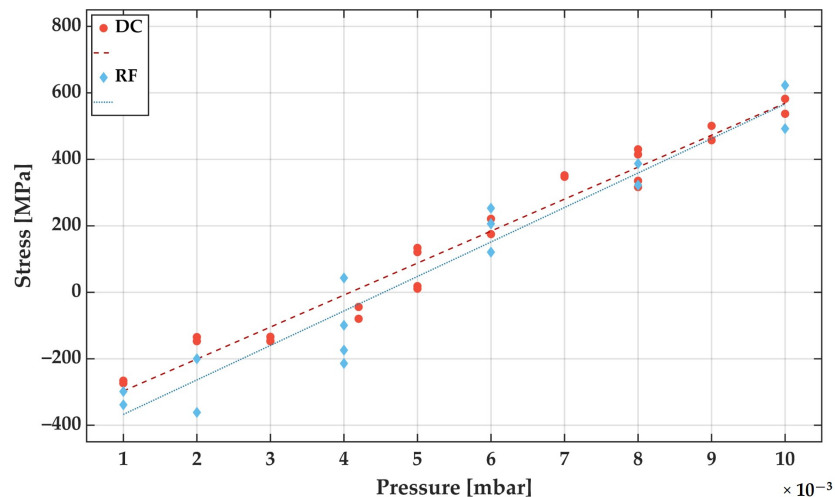


Figure 5. Determined film stress measurements for depositions performed with DC (red) and RF (blue) with different Ar deposition pressures. The resulting FeCoSiB film thickness was set to 200 nm and the initial and resulting bending is measured with a laser confocal microscope. The film stresses are calculated by the Stoney equation from the curvature of the cantilevers before and after film deposition. (The data are fitted with a simple linear regression).

It is clearly visible that both deposition modes show a similar film stress to deposition pressure relation. The overall course of the stress vs. Ar deposition pressure curves can be explained by the pressure-dependent mean free path of the film formers. At lower pressure the sputtered species retain their kinetic energy and a more compact film growth [30]. According to the assumed linear regression, the transition from compressive to tensile stress appears at around 4.0×10^{-3} mbar and 4.5×10^{-3} mbar for DC and RF deposition, respectively. For both deposition modes, the Ar deposition pressure can be adjusted to obtain FeCoSiB layers with low-stress magnitudes.

To relate the changes in film stress to the magnetic properties of the film, 10 mm × 10 mm sized samples with a 200 nm thick FeCoSiB layer were analyzed utilizing MOKE magnetometry and microscopy. For the measurement of the magnetization loops the region of interest was positioned in the center of the sample with a size of 5 mm × 5 mm, which approximately corresponds to the SAW sensor magnetic film size and position. Concentrating on the center of the films minimizes edge effects in the measurements of the magnetization reversal and thereby reflects the actual magnetic film properties.

Magnetization loops obtained field from RF and DC deposited samples at deposition pressures of 2.0×10^{-3} mbar and 8.0×10^{-3} mbar are shown in Figure 6. The corresponding film stress is ≥ 200 MPa compressive and ≥ 300 MPa tensile for 2.0×10^{-3} mbar and 8.0×10^{-3} mbar, respectively. The magnetic field was applied from -3 mT to $+3$ mT parallel and perpendicular to the magnetic deposition field $\mu_0 H_{\text{dep}}$.

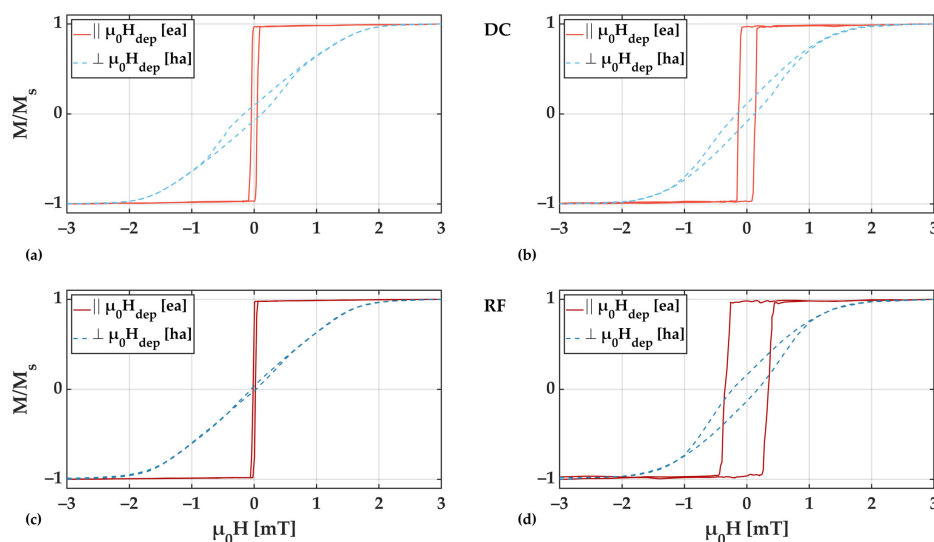


Figure 6. Magnetization curves for 200 nm thick FeCoSiB films deposited with DC (a,b) and RF (c,d) at an Ar deposition pressure of 2.0×10^{-3} mbar (a,c) and 8.0×10^{-3} mbar (b,d) measured along and perpendicular to μ_0H_{dep} , respectively along the presumed easy axis (ea) and hard axis (ha) of magnetization. The measured area of $5 \text{ mm} \times 5 \text{ mm}$ was set to the sample center to avoid edge effects. The measurement field was applied parallel (red) and perpendicular (blue) to μ_0H_{dep} .

From the magnetization loops, clear uniaxial anisotropy characteristics can be derived with the easy axis (ea) of magnetization aligned along the direction of μ_0H_{dep} . In all cases, the coercivity of the magnetic films increases with tensile film stress.

In Figure 7, corresponding magnetic domain images obtained at zero field from the same RF and DC deposited samples are shown. Small tilts (up to 5°) of the induced anisotropy axis are visible as a result from slight field inhomogeneities in the deposition field setup (μ_0H_{dep}) and/or deviations in the position in the sputtering chamber.

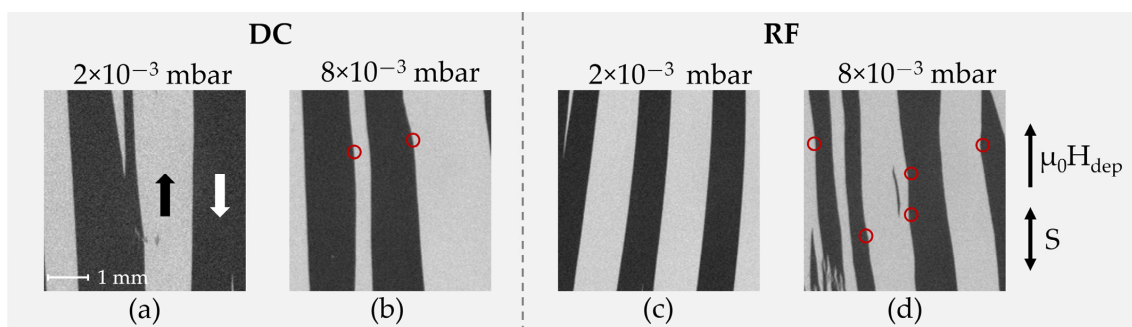


Figure 7. MOKE microscopy images of demagnetized magnetic samples deposited with 10 nm Ta/200 nm FeCoSiB /10 nm Ta with an applied magnetic deposition field μ_0H_{dep} during deposition, at Ar deposition pressures of 2.0×10^{-3} mbar (a,c) and 8.0×10^{-3} mbar (b,d) for DC (a,b) and RF (c,d) sputter-deposited samples. The magneto-optical sensitivity S is aligned parallel to the μ_0H_{dep} . The FeCoSiB films with low deposition pressure and high compressive film stresses (a,c) show a slight misalignment of the magnetic domain walls by up to 5° as compared to the direction of μ_0H_{dep} . At high deposition pressures and high tensile stresses (b,d), magnetic domain wall pinning centers (red circles) appear in the magnetic layer.

For both deposition pressures the formation of large and well-aligned magnetic domains becomes visible. In contrast to the 2.0×10^{-3} mbar samples, the 8.0×10^{-3} mbar

samples show areas of local domain wall pinning (red circles in Figure 7), which are particularly evident for the case of RF deposition. This is an indication of magnetically active defects, which are related to magnetic property inhomogeneities. The domain wall pinning becomes also visible during the magnetization reversal along the magnetic easy axis (not shown). It is directly reflected in the variations seen in the magnetization loops (Figure 6). Considering the high tensile stresses, the presumed magnetic property variations are assumed to be due to local magneto–elastic interactions, which directly influence the magnetic behavior [31]. The exact nature of the defects cannot be concluded from our measurements.

Overall, comparing the measured magnetization loops at low and high deposition pressure, a significant broadening is visible for higher pressures, which correlates directly with the observed changes in magnetic domain characteristics and substantiates the domain wall pinning by local stress fields due to an increase in stress magnitude.

An accurate parameter to quantify the change in the magnetization loops is the hysteresis loss. The hysteresis loss is especially important as it is strongly connected to the exhibited magnetic noise in magnetolectric composite magnetic field sensors [32–34]. Data for the whole parameter range are displayed in Figure 8a for DC and Figure 8b for RF deposition for Ar deposition pressures ranging from 2.0×10^{-3} mbar to 8.0×10^{-3} mbar. A saturation magnetization of $M_s = 1193$ kA/m [35] was assumed for the extraction from the MOKE loops.

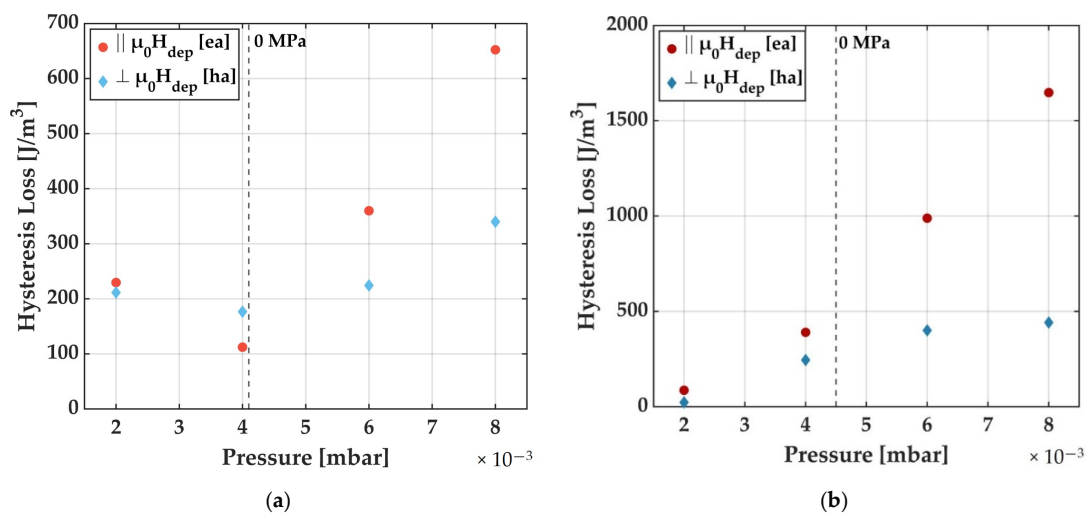


Figure 8. Hysteresis losses for DC (a) and RF (b) deposited FeCoSiB films as a function of Ar deposition pressure. The values in (a,b) were obtained from hysteresis curves of magnetic test samples with a measured area of $5 \text{ mm} \times 5 \text{ mm}$ located in the center of the samples. To determine the hysteretic losses, the enclosed area of the hysteresis curves was determined according to the orientation parallel and perpendicular to $\mu_0 H_{\text{dep}}$. The approximate positions of zero stresses are indicated.

For both deposition methods, a trend to higher hysteresis losses with higher Ar deposition pressure is visible. Although we assume that the FeCoSiB films deposited with RF and DC have the same chemical composition (ERDA) and structure (XRD), we see a clear trend in the change of magnitude of magnetic losses. From the magnetic domain studies, we relate this to inhomogeneities in the magnetic films that, in connection with the magnetostrictive material, hinder the magnetization process. Magnetic domain wall pinning and a reduction of small field permeability arise from the magnetoelastic interactions. It is well known that CoFe-based amorphous soft-magnetic alloys display a minimum in coercivity with zero magnetostriction [36] due to the exhibited coupling between stresses and magnetic properties.

3.3. SAW Sensor Performance

As shown in the previous chapter, a uniaxial anisotropy cannot be induced precisely with increasing sputtering pressure. Therefore, the FeCoSiB films on the SAW devices are deposited at sputtering pressures, which correspond to film stresses of -200 MPa (compressive stress), i.e., 2.0×10^{-3} mbar for DC deposition and 2.5×10^{-3} mbar for RF deposition (see Figure 5).

An analogous magnetic analysis as shown before, including magnetization loop measurements and magnetic domain analysis, was performed directly on the SAW devices. The magnetic analysis was further restricted to the active region of the SAW device. Magnetization loops with the magnetic field along and perpendicular to the direction of wave propagation are shown in Figure 9. The magnetic field direction perpendicular to the deposition field ($\perp \mu_0 H_{\text{dep}}$) corresponds to the applied bias field in SAW sensor operation defining the working point. To get a clearer view on the overall magnetization reversal behavior also the transverse magnetization loops [32,37] are analyzed.

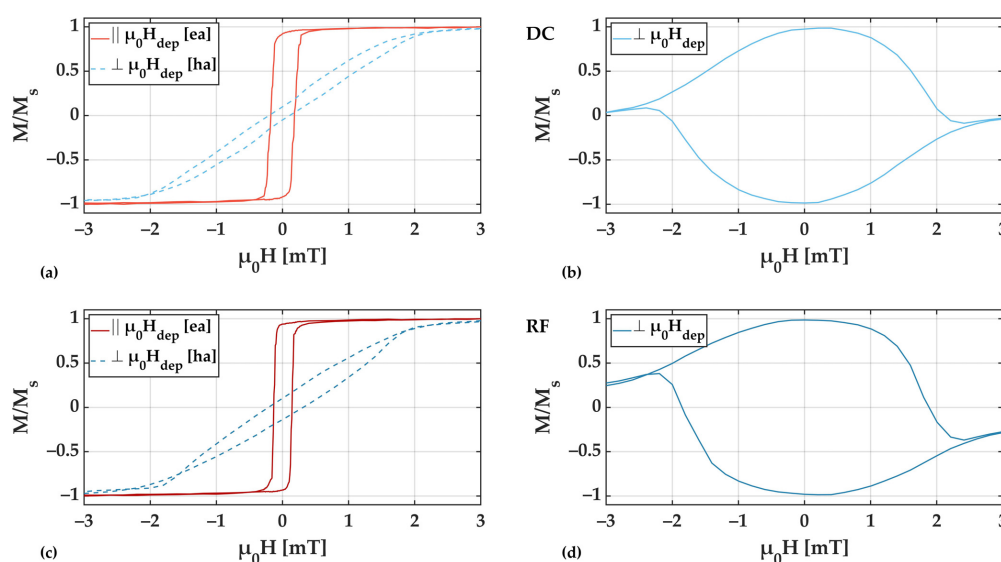


Figure 9. Longitudinal and transversal magnetization curves for a 200 nm thick FeCoSiB film deposited with DC sputter deposition at an Ar pressure of 2.0×10^{-3} mbar (a,b) and with RF sputter deposition at an Ar pressure of 2.5×10^{-3} mbar (c,d) from SAW devices. Longitudinal curves were measured along (red) and perpendicular (blue) to $\mu_0 H_{\text{dep}}$, the latter being perpendicular to the SAW propagation direction. The measured area was set in accordance with the active SAW device area.

Corresponding magnetic domain images at magnetic bias fields $\mu_0 H_{\text{bias}}$ of -0.35 mT and $+0.35$ mT coming from negative and positive saturation, respectively, are displayed in Figure 10.

The magnetic hysteresis effects are more pronounced as in the case of the extended thin films, which we attribute to magnetic domain effects at the sample edges. Spike domains extending in the active region of the sensor become visible in Figure 10e, which hinder the magnetization reversal and which lead to an increase in coercivity for the magnetic field directions along and perpendicular to $\mu_0 H_{\text{dep}}$. For the magnetic field direction perpendicular to $\mu_0 H_{\text{dep}}$ we obtain a coercivity field of $\mu_0 H_c \approx 0.15$ mT for RF and $\mu_0 H_c \approx 0.3$ mT in the case of DC sputter deposition. From the transverse magnetization loops (Figure 9b,d), a mostly coherent rotation of magnetization is obtained for the horizontally aligned magnetic bias fields. Despite the rotational process, unity of magnetization is not reached due to the spike domain formation at the top and bottom edge. The lower amplitude in the general

magnetic and magnetic domain behavior of the magnetostrictive phase of the SAW sensors is comparable. The hysteretic magnetization reversal behavior has a direct influence on the SAW sensor characteristics.

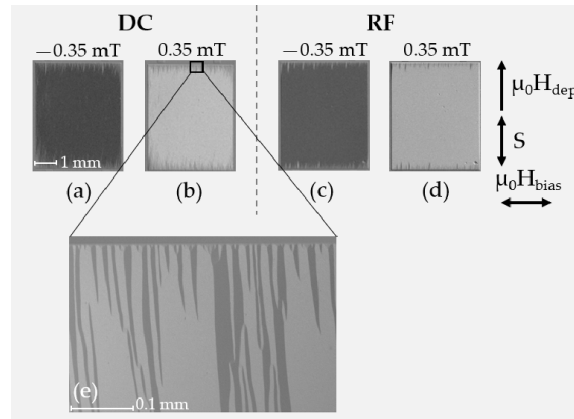


Figure 10. MOKE images from DC (a,b,e) and RF (c,d) sputter deposited SAW structures at magnetic bias fields $\mu_0 H_{\text{bias}}$ of -0.35 mT and $+0.35$ mT aligned perpendicular to $\mu_0 H_{\text{dep}}$ (as indicated). The magneto-optical sensitivity (S) is aligned parallel to $\mu_0 H_{\text{dep}}$. Nearly single magnetic domain behavior occurs. Yet, spike domains (e) [38] at the bottom and top edges (\perp to $\mu_0 H_{\text{dep}}$) form. Shown in (e) is a higher resolution ($20\times$) version of image (a) in the area of the upper edge and shows the spike domains.

Figure 11a shows the phase change of SAW sensors with DC and RF deposited FeCoSiB films under the intrinsic compressive stress as a function of an applied DC bias stress as a function of an applied DC bias field $\mu_0 H_{\text{Bias}}$. The field was changed from -10 mT to $+10$ mT and vice versa with a step size of 25 μT in the most relevant field range from -1 mT to $+1$ mT.

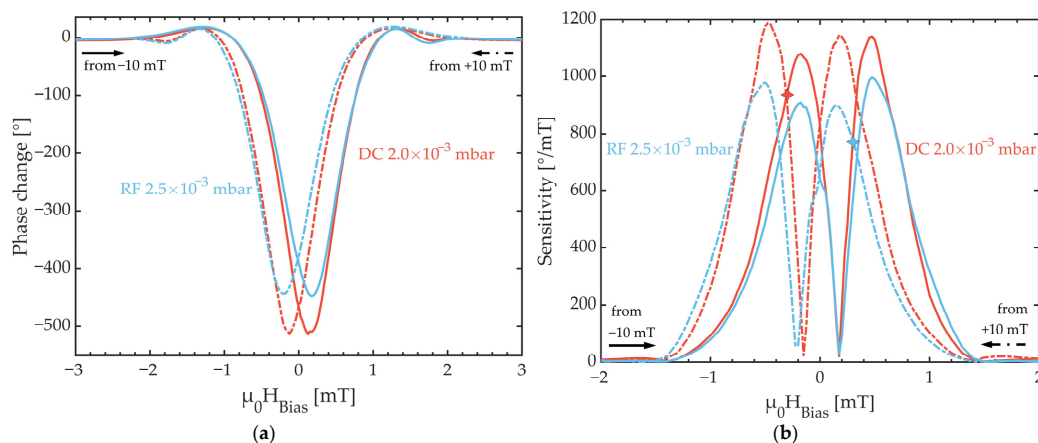


Figure 11. (a) Phase change of SAW sensors as a function of applied DC bias field for DC (red) and RF (blue) deposited FeCoSiB films with low compressive film stress. (b) Measured sensitivity as a function of applied DC bias field obtained using a 1 μT AC field for DC (red) and RF (blue) deposited FeCoSiB films with compressive film stress. Markings in the DC and RF curves highlight the magnetic bias field in which the best LOD measurement has been achieved. All curves in (a,b) were recorded from -10 mT to $+10$ mT and vice versa. The measurement step size in the range from -1 mT to $+1$ mT is 25 μT . AC and DC fields were applied perpendicular to the SAW propagation direction.

With 510° for the DC sputtered sensor and 450° for RF the total phase changes are very similar for both deposition techniques. In fact, several sensors have been measured to confirm the obtained results and all show maximum phase changes between 430° and 510° . The hysteresis characteristics are in accordance with the magnetometric analysis of the obtained bias curves, i.e., the large hysteresis between the two field scanning directions for each deposition technique. While in an ideal hysteresis-free case both phase minima are expected to be at 0 mT bias field [5], they are around the coercive fields at -0.125 mT and $+0.125$ mT for the DC deposition case and -0.2 mT and $+0.175$ mT for the RF deposited films. Nevertheless, the bias curve hysteresis is very similar for both deposition techniques and therefore independent of the type of deposition bias.

In Figure 11b, the measured sensitivity, i.e., the derivative of the phase change, shows two characteristic sensitivity maxima for each measurement direction and each sensor. The maxima indicate the positions of the highest slope in the static bias curves in Figure 11a. These points of highest sensitivity for the RF deposition case are at -0.175 mT and $+0.475$ mT coming from negative saturation with maximum sensitivities of $907^\circ/\text{mT}$ and $996^\circ/\text{mT}$, respectively, and at $+0.15$ mT and -0.5 mT coming from positive saturation with maximum sensitivities of $900^\circ/\text{mT}$ and $978^\circ/\text{mT}$, respectively. For the DC deposited films, these respective points are at -0.175 mT and $+0.475$ mT coming from negative saturation and $+0.175$ mT and -0.475 mT coming from positive saturation with sensitivity of $1081^\circ/\text{mT}$, $1138^\circ/\text{mT}$, $1144^\circ/\text{mT}$ and $1188^\circ/\text{mT}$, respectively. The slight differences in total phase change and sensitivities originate from slightly varying FeCoSiB thicknesses [9] and tilted orientation of magnetic anisotropy [8]. However, the values presented here are in good agreement with previously published results covering a sensitivity range from $500^\circ/\text{mT}$ to $2000^\circ/\text{mT}$ [5,8,9,32].

While the sensitivity is a useful sensor characteristic, the measure which ultimately quantifies the performance of a magnetic field sensor, however, is the limit of detection (LOD). The LOD results from dividing the sensors noise, in this case phase noise, by its sensitivity. As shown in Figures 11b and 12a, while the maximum sensitivity of the sensor with DC deposited FeCoSiB is higher than the phase noise is, in general, it is lower for the RF deposited films.

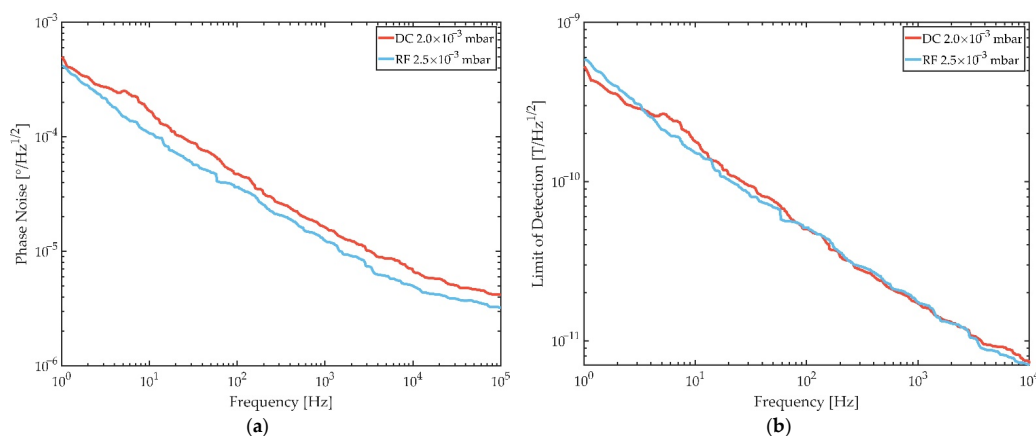


Figure 12. (a) Phase noise as a function of frequency from the SAW excitation carrier for DC (red) and RF (blue) deposited FeCoSiB films with compressive film stress. The shown phase noise spectra are measured at magnetic bias fields and excitation powers, which lead to the lowest limits of detection. In the DC deposition case this corresponds to a bias field of -0.3 mT (from negative saturation) and an excitation power of 1 dBm, and in the RF deposition case this is $+0.35$ mT (from positive saturation) and 2 dBm. (b) Limit of detection as a function of frequency from the SAW excitation carrier for DC (red) and RF (blue) deposited FeCoSiB films with compressive film stress. The limit of detection is the quotient of a sensors phase noise and its sensitivity.

The phase noise spectra in Figure 12a are both recorded under sensor operating parameters, which lead to the lowest LOD for each sensor. More precisely, these parameters are the excitation power and $\mu_0 H_{\text{bias}}$. Phase noise spectra were measured for various DC bias fields and it turned out that the lowest LODs are achieved when applying a bias field slightly higher, i.e., slightly off the point of highest sensitivity. For the DC deposition case, this is at -0.3 mT coming from negative saturation and $+0.35$ mT coming from positive saturation for the RF case. For the excitation power, it was shown before that there exists an optimum excitation power where the phase noise is the lowest in SAW magnetic field sensors [32]. For the sensor design considered in Ref. [32] and here, this optimum excitation power is 1 dBm for the DC deposition case and for the RF case it is 2 dBm. Finally, this optimum operation leads to detection limits as low as 179 pT/Hz^{1/2} for DC deposited films and 152 pT/Hz^{1/2} for RF deposited films at 10 Hz, respectively. At 100 Hz the LODs are 51 pT/Hz^{1/2} (DC) and 52 pT/Hz^{1/2} (RF).

However, it should be noted that the LODs of all sensors investigated for this study vary for both deposition types between 152 pT/Hz^{1/2} and 190 pT/Hz^{1/2} at 10 Hz and can therefore be considered equivalent. This shows that in terms of SAW magnetic field sensor performance with DC deposited films, the same LODs can be achieved while providing lower deposition times and less heat generation.

4. Conclusions

FeCoSiB thin films using DC magnetron sputtering for magnetic field SAW sensors were shown to give equivalent results in terms of magnetic properties as well as sensor performance as compared to commonly used RF deposited layers.

Due to the higher deposition rate in DC operation, it becomes possible to reduce the total deposition time by a factor of 3, which is a significant improvement and advantage over the common RF sputter process. Furthermore, the chemical composition measured by ERDA and the structure measured by XRD of the prepared films are identical for DC and RF deposited FeCoSiB. Major factors influencing the magnetic performance of the SAW sensors such as film stress can be controlled and show that compressively stressed FeCoSiB films provide better control of the soft-magnetic film properties. On the SAW device level, it was shown that the magnetic layer properties and the resulting detection limits of the sensors with a single layer of 200 nm FeCoSiB are virtually the same with 51 pT/Hz^{1/2} (DC) and 52 pT/Hz^{1/2} (RF) at 100 Hz and with 179 pT/Hz^{1/2} on average at 10 Hz. Through further development of DC mode deposited magnetic films it will be possible to further improve the magnetic anisotropy of the thin film as well as to reduce the film variance. Thus, it will be possible to further improve the sensitivity, as well as the resulting LOD, with a significantly accelerated preparation process.

Another approach to improve the sensor performance is to use other structuring mechanisms, such as ion beam etching, to gain better control over the edge profile of the FeCoSiB, while also reducing possible defect structures caused by the resist needed for the lift-off process. Alternative magnetic layer systems, such as exchange bias stacks, show significant improvements in sensor performances [39–41]. However, due to the complexity of the exchange bias systems, the deposition times would increase significantly when using the RF mode, which can now be ideally compensated by DC film deposition.

Author Contributions: Conceptualization, L.T., D.S., V.S., F.M., J.M. and D.M.; methodology, L.T., V.S. and D.S.; validation, L.T.; formal analysis, L.T., D.S. and V.S.; investigation, L.T., D.S., V.S., F.M.; resources, L.T., V.S., F.M. and D.S.; data curation, L.T.; writing—original draft preparation, L.T., V.S., D.S., F.M. and D.M., J.M.; writing—review and editing, D.M., J.M. and F.M.; visualization, L.T., D.S. and V.S.; supervision, D.M. and J.M.; project administration, D.M. and J.M.; funding acquisition, D.M. and J.M. All authors have read and agreed to the published version of the manuscript.

Funding: This research was funded by the German Research Foundation (Deutsche Forschungsgemeinschaft, DFG) through the project A1 of the Collaborative Research Centre CRC 1261 ‘Magneto-electric Sensors: From Composite Materials to Biomagnetic Diagnostics’. The chemical analysis was funded by Helmholtz-Zentrum Dresden-Rossendorf (HZDR) through the proposal 2002176.

Data Availability Statement: The data presented in this study are available on request from the corresponding author.

Acknowledgments: We thank Katrin Brandenburg and Sabrina Curt is for proof-reading of the manuscript. Also, the authors would like to thank DFG and HZDR for funding.

Conflicts of Interest: The authors declare no conflict of interest. The funders had no role in the design of the study; in the collection, analyses, or interpretation of data; in the writing of the manuscript, or in the decision to publish the results.

Appendix A

Table A1. Chronological comparison of selected SAW magnetic field sensors from 2018 to 2021 based on substrate and magnetic layer.

Source	Substrate	IDT	SAW Guiding/Top Layer	Magnetic Layer	Wave Form	Operating Frequency	Sensitivity
This work	ST-cut quartz x + 90°	10 nm Ta/200 nm Au/10 nm Cr	4.5 μm SiO ₂	10 nm Ta/ 200 nm FeCoSiB/ 10 nm Ta	Love wave	144 MHz	1188°/m (2373 kHz/mT *)
Fahim 2021 [42]	ST-cut quartz (Murata RO3101)	Al	-	PVA + Ni/Fe nanopowder	-	433.92 MHz	5.83 kHz/mT
Mishra 2020 [43]	ST-cut quartz x + 90°	Al	400 nm ZnO	100 nm CoFeB	Love wave	421 MHz	0.75 kHz/mT
Yang 2020 [44]	ST-cut quartz x + 90°	100 nm Al	333 nm ZnO/ 400 nm SiO ₂	5 nm Ta/ 100 nm Co ₄₀ Fe ₄₀ B ₂₀ / 5 nm Pt	Love wave	433 MHz	−170.4 kHz/mT
Schell 2020 [8]	ST-cut quartz x + 90°	10 nm Cr/300 nm Au/C10 nm Cr	4.5 μm SiO ₂	8 nm Ta/ 200 nm FeCoSiB/ 5 Ta	Love wave	147–148 MHz	2000°/mT (3999 kHz/mT *)
Mishra 2020 [27]	ST-cut quartz x + 90°	100 nm Al	510 nm ZnO	100 nm CoFeB	Love wave	433 MHz	15.53 kHz/mT
Jia 2020 [13]	128°YX LiNbO ₃	300 nm Al	50 nm SiO ₂	50 nm Cr/ 500 nm FeCo (dot array)	-	150 MHz	6 kHz/mT
Xiangli 2018 [4]	ST-cut quartz x + 90°	Ta	SiO ₂	FeCoSiB	Love wave	221.76 MHz	663.98 kHz/mT
Kittman 2018 [5]	ST-cut quartz x + 90°	12 nm Cr/300 nm Au/12 nm Cr	4.5 μm SiO ₂	10 nm Ta/ 200 nm FeCoSiB/ 10 nm Ta	Love wave	147.2 MHz	504°/mT (1008 kHz/mT *)

* The specification in kHz/mT represents an approximation. For data conversion a delay time of 1389 ns has been assumed. This delay time was reported for a similar sensor design as considered here [24].

References

- Ruppel, C.W.; Dill, R.; Fischerauer, A.; Fischerauer, G.; Gawlik, A.; Machui, J.; Muller, F.; Reindl, L.; Ruile, W.; Scholl, G.; et al. SAW devices for consumer communication applications. *IEEE Trans. Ultrason. Ferroelectr. Freq. Control* **1993**, *40*, 438–452. [\[CrossRef\]](#)
- Malave, A.; Schlecht, U.; Gronewold, T.M.A.; Perpeet, M.; Tewes, M. Lithium Tantalate Surface Acoustic Wave Sensors for Bio-Analytical Applications. In Proceedings of the 5th IEEE Conference on Sensors (IEEE Sensors 2006), Daegu, Korea, 22–25 October 2006; pp. 604–607. [\[CrossRef\]](#)
- Schlenso, M.D.; Gronewold, T.M.A.; Tewes, M.; Famulok, M.; Quandt, E. A Love-wave biosensor using nucleic acids as ligands. *Sens. Actuators B Chem.* **2004**, *101*, 308–315. [\[CrossRef\]](#)
- Yang, Y.; Mengue, P.; Mishra, H.; Floer, C.; Hage-Ali, S.; Petit-Watelot, S.; Lacour, D.; Hehn, M.; Han, T.; Elmazria, O. Wireless Multifunctional Surface Acoustic Wave Sensor for Magnetic Field and Temperature Monitoring. *Adv. Mater. Technol.* **2021**, 2100860. [\[CrossRef\]](#)
- Kittmann, A.; Durdaut, P.; Zabel, S.; Reermann, J.; Schmalz, J.; Spetzler, B.; Meyners, D.; Sun, N.X.; McCord, J.; Gerken, M.; et al. Wide Band Low Noise Love Wave Magnetic Field Sensor System. *Sci. Rep.* **2018**, *8*, 278. [\[CrossRef\]](#)
- Liu, X.; Tong, B.; Ou-Yang, J.; Yang, X.; Chen, S.; Zhang, Y.; Zhu, B. Self-biased vector magnetic sensor based on a Love-type surface acoustic wave resonator. *Appl. Phys. Lett.* **2018**, *113*, 82402. [\[CrossRef\]](#)
- Polewczyk, V.; Dumesnil, K.; Lacour, D.; Moutaouekkil, M.; Mjahed, H.; Tiercelin, N.; Petit-Watelot, S.; Mishra, H.; Dusch, Y.; Hage-Ali, S.; et al. Unipolar and Bipolar High-Magnetic-Field Sensors Based on Surface Acoustic Wave Resonators. *Phys. Rev. Appl.* **2017**, *8*, 024001. [\[CrossRef\]](#)

8. Schell, V.; Müller, C.; Durdaut, P.; Kittmann, A.; Thormählen, L.; Lofink, F.; Meyners, D.; Höft, M.; McCord, J.; Quandt, E. Magnetic anisotropy controlled FeCoSiB thin films for surface acoustic wave magnetic field sensors. *Appl. Phys. Lett.* **2020**, *116*, 73503. [[CrossRef](#)]
9. Kittmann, A.; Müller, C.; Durdaut, P.; Thormählen, L.; Schell, V.; Niekietel, F.; Lofink, F.; Meyners, D.; Knöchel, R.; Höft, M.; et al. Sensitivity and noise analysis of SAW magnetic field sensors with varied magnetostrictive layer thicknesses. *Sens. Actuators A Phys.* **2020**, *311*, 111998. [[CrossRef](#)]
10. Kadota, M.; Ito, S. Sensitivity of Surface Acoustic Wave Magnetic Sensors Composed of Various Ni Electrode Structures. *Jpn. J. Appl. Phys.* **2012**, *51*, 07GC21. [[CrossRef](#)]
11. Li, W.; Dhagat, P.; Jander, A. Surface Acoustic Wave Magnetic Sensor using Galfenol Thin Film. *IEEE Trans. Magn.* **2012**, *48*, 4100–4102. [[CrossRef](#)]
12. Mishra, H.; Hehn, M.; Hage-Ali, S.; Petit-Watelot, S.; Mengue, P.W.; Zghoon, S.; M’Jahed, H.; Lacour, D.; Elmazria, O. Microstructured Multilayered Surface-Acoustic-Wave Device for Multifunctional Sensing. *Phys. Rev. Appl.* **2020**, *14*, 014053. [[CrossRef](#)]
13. Jia, Y.; Wang, W.; Sun, Y.; Liu, M.; Xue, X.; Liang, Y.; Du, Z.; Luo, J. Fatigue Characteristics of Magnetostrictive Thin-Film Coated Surface Acoustic Wave Devices for Sensing Magnetic Field. *IEEE Access* **2020**, *8*, 38347–38354. [[CrossRef](#)]
14. Mishra, H.; Hehn, M.; Lacour, D.; Elmazria, O.; Tiercelin, N.; M’Jahed, H.; Dumesnil, K.; Petit-Watelot, S.; Polewczyk, V.; Talbi, A.; et al. Intrinsic versus shape anisotropy in micro-structured magnetostrictive thin films for magnetic surface acoustic wave sensors. *Smart Mater. Struct.* **2019**, *28*, 12LT01. [[CrossRef](#)]
15. McCord, J.; Schäfer, R.; Frommberger, M.; Glasmachers, S.; Quandt, E. Stress-induced remagnetization in magnetostrictive films. *J. Appl. Phys.* **2004**, *95*, 6861–6863. [[CrossRef](#)]
16. Peng, B.; Zhang, W.L.; Zhang, W.X.; Jiang, H.C.; Yang, S.Q. Effects of stress on the magnetic properties of the amorphous magnetic films. *Phys. B Condens. Matter* **2006**, *382*, 135–139. [[CrossRef](#)]
17. O’Handley, R.C. *Modern Magnetic Materials: Principles and Applications*; Wiley: New York, NY, USA, 2000; ISBN 0-471-15566-7.
18. Fiorillo, F. *Measurement and Characterization of Magnetic Materials*; Elsevier: Amsterdam, The Netherlands, 2004; ISBN 978-0-12-257251-7.
19. Wang, Y.; Nastasi, M.A. (Eds.) *Handbook of Modern Ion Beam Materials Analysis*, 2nd ed.; Materials Research Soc.: Warrendale, PA, USA, 2009; ISBN 978-1-60511-215-2.
20. Kreissig, U.; Grigull, S.; Lange, K.; Nitzsche, P.; Schmidt, B. In situ ERDA studies of ion drift processes during anodic bonding of alkali-borosilicate glass to metal. *Nucl. Instrum. Methods Phys. Res. Sect. B Beam Interact. Mater. At.* **1998**, *136–138*, 674–679. [[CrossRef](#)]
21. Barradas, N.P.; Jeynes, C.; Webb, R.P. Simulated annealing analysis of Rutherford backscattering data. *Appl. Phys. Lett.* **1998**, *71*, 291. [[CrossRef](#)]
22. Janssen, G.C.A.M.; Abdalla, M.M.; van Keulen, F.; Pujada, B.R.; van Venrooy, B. Celebrating the 100th anniversary of the Stoney equation for film stress: Developments from polycrystalline steel strips to single crystal silicon wafers. *Thin Solid Film.* **2009**, *517*, 1858–1867. [[CrossRef](#)]
23. Piorra, A.; Jahns, R.; Teliban, I.; Gugat, J.L.; Gerken, M.; Knöchel, R.; Quandt, E. Magnetolectric thin film composites with interdigital electrodes. *Appl. Phys. Lett.* **2013**, *103*, 32902. [[CrossRef](#)]
24. Durdaut, P.; Kittmann, A.; Rubiola, E.; Friedt, J.-M.; Quandt, E.; Knochel, R.; Hoft, M. Noise Analysis and Comparison of Phase-and Frequency-Detecting Readout Systems: Application to SAW Delay Line Magnetic Field Sensor. *IEEE Sens. J.* **2019**, *19*, 8000–8008. [[CrossRef](#)]
25. Devkota, J.; Ohodnicki, P.R.; Greve, D.W. SAW Sensors for Chemical Vapors and Gases. *Sensors* **2017**, *17*, 801. [[CrossRef](#)] [[PubMed](#)]
26. Wang, W.; Jia, Y.; Xue, X.; Liang, Y.; Du, Z. Grating-patterned FeCo coated surface acoustic wave device for sensing magnetic field. *AIP Adv.* **2018**, *8*, 15134. [[CrossRef](#)]
27. Mishra, H.; Streque, J.; Hehn, M.; Mengue, P.; M’Jahed, H.; Lacour, D.; Dumesnil, K.; Petit-Watelot, S.; Zhgoon, S.; Polewczyk, V.; et al. Temperature compensated magnetic field sensor based on love waves. *Smart Mater. Struct.* **2020**, *29*, 45036. [[CrossRef](#)]
28. McCord, J. Progress in magnetic domain observation by advanced magneto-optical microscopy. *J. Phys. D Appl. Phys.* **2015**, *48*, 333001. [[CrossRef](#)]
29. Lee, S.L.; Windover, D.; Lu, T.-M.; Audino, M. In situ phase evolution study in magnetron sputtered tantalum thin films. *Thin Solid Film.* **2002**, *420–421*, 287–294. [[CrossRef](#)]
30. Thornton, J.A.; Hoffman, D.W. Stress-related effects in thin films. *Thin Solid Film.* **1989**, *171*, 5–31. [[CrossRef](#)]
31. Hubert, A.; Schäfer, R. *Magnetic Domains: The Analysis of Magnetic Microstructures*; Corr. Print., [Nachdr.]; Springer: Berlin, Germany, 2011; ISBN 978-3-540-64108-7.
32. Durdaut, P.; Müller, C.; Kittmann, A.; Schell, V.; Bahr, A.; Quandt, E.; Knöchel, R.; Höft, M.; McCord, J. Phase Noise of SAW Delay Line Magnetic Field Sensors. *Sensors* **2021**, *21*, 5631. [[CrossRef](#)]
33. Urs, N.O.; Golubeva, E.; Röbisch, V.; Toxvaerd, S.; Deldar, S.; Knöchel, R.; Höft, M.; Quandt, E.; Meyners, D.; McCord, J. Direct Link between Specific Magnetic Domain Activities and Magnetic Noise in Modulated Magnetolectric Sensors. *Phys. Rev. Appl.* **2020**, *13*, 28. [[CrossRef](#)]
34. Urs, N.O.; Teliban, I.; Piorra, A.; Knöchel, R.; Quandt, E.; McCord, J. Origin of hysteretic magnetoelastic behavior in magnetolectric 2-2 composites. *Appl. Phys. Lett.* **2014**, *105*, 202406. [[CrossRef](#)]

35. Ludwig, A.; Quandt, E. Optimization of the ΔE effect in thin films and multilayers by magnetic field annealing. *IEEE Trans. Magn.* **2002**, *38*, 2829–2831. [[CrossRef](#)]
36. O’Handley, R.; Mendelsohn, L.; Nesbitt, E. New non-magnetostrictive metallic glass. *IEEE Trans. Magn.* **1976**, *12*, 942–944. [[CrossRef](#)]
37. McCord, J.; Schäfer, R.; Mattheis, R.; Barholz, K.-U. Kerr observations of asymmetric magnetization reversal processes in CoFe/IrMn bilayer systems. *J. Appl. Phys.* **2003**, *93*, 5491–5497. [[CrossRef](#)]
38. Hubert, A.; Schäfer, R. *Magnetic Domains: The Analysis of Magnetic Microstructures*; Softcover Reprint of the Hardcover 1st ed. 1998, Corrected Print. 2000; Springer: Berlin, Germany, 2014; ISBN 978-3-540-85054-0.
39. Lage, E.; Kirchof, C.; Hrkac, V.; Kienle, L.; Jahns, R.; Knöchel, R.; Quandt, E.; Meyners, D. Exchange biasing of magnetoelectric composites. *Nat. Mater.* **2012**, *11*, 523–529. [[CrossRef](#)] [[PubMed](#)]
40. Röbisch, V.; Salzer, S.; Urs, N.O.; Reermann, J.; Yarar, E.; Piorra, A.; Kirchof, C.; Lage, E.; Höft, M.; Schmidt, G.U.; et al. Pushing the detection limit of thin film magnetoelectric heterostructures. *J. Mater. Res.* **2017**, *32*, 1009–1019. [[CrossRef](#)]
41. Jovičević Klug, M.; Thormählen, L.; Röbisch, V.; Toxvaerd, S.D.; Höft, M.; Knöchel, R.; Quandt, E.; Meyners, D.; McCord, J. Antiparallel exchange biased multilayers for low magnetic noise magnetic field sensors. *Appl. Phys. Lett.* **2019**, *114*, 192410. [[CrossRef](#)]
42. Fahim; Mainuddin; Rajput, P.; Kumar, J.; Nimal, A.T. A simple and novel SAW magnetic sensor with PVA bound magnetostrictive nanopowder film. *Sens. Actuators A Phys.* **2021**, *331*, 112926. [[CrossRef](#)]
43. Mishra, H.; Hehn, M.; Hage-Ali, S.; Petit-Watelot, S.; Mengue, P.W.; M’Jahed, H.; Lacour, D.; Elmazria, O.; Zghoon, S. Multifunctional sensor (Magnetic field and temperature) based on Micro-structured and multilayered SAW device. In Proceedings of the 2020 IEEE International Ultrasonics Symposium (IUS), Las Vegas, NV, USA, 7–11 September 2020; pp. 1–4, ISBN 978-1-7281-5448-0.
44. Yang, Y.; Mishra, H.; Mengue, P.; Hage-Ali, S.; Petit-Watelot, S.; Lacour, D.; Hehn, M.; M’Jahed, H.; Han, T.; Elmazria, O. Enhanced Performance Love Wave Magnetic Field Sensors With Temperature Compensation. *IEEE Sens. J.* **2020**, *20*, 11292–11301. [[CrossRef](#)]

3.3 Thin-Film-Based SAW Magnetic Field Sensors

In this publication the first SAW magnetic field sensor is presented, in which the acoustic waves are generated on a piezoelectric AlScN thin film. For this concept, it was shown that several modes are excited in the AlScN film, of which a Rayleigh mode turned out the most sensitive. The sensitivity as well as the noise of these devices which are fabricated at Fraunhofer ISIT, have been investigated.

Author Contributions

Own contribution to the manuscript:

- Measurements of samples (large fraction)
- Designed experiments (shared)
- Interpretation of the results (shared)
- Discussion and review of the manuscript (shared)

Reproduced from *Sensors* **21**, 8166 (2021); DOI: 10.3390/s21248386.



Communication

Thin-Film-Based SAW Magnetic Field Sensors

Jana Marie Meyer^{1,*}, Viktor Schell², Jingxiang Su¹, Simon Fichtner^{1,2}, Erdem Yarar¹, Florian Niekietl¹, Thorsten Giese¹, Anne Kittmann², Lars Thormählen², Vadim Lebedev³, Stefan Moench³, Agnė Žukauskaitė³, Eckhard Quandt² and Fabian Lofink¹

¹ Fraunhofer Institute for Silicon Technology ISIT, Fraunhoferstrasse 1, 25524 Itzehoe, Germany

² Institute for Materials Science, Kiel University, Kaiserstraße 2, 24143 Kiel, Germany

³ Fraunhofer Institute for Applied Solid State Physics IAF, Tullastrasse 72, 79108 Freiburg, Germany

* Correspondence: jana.meyer@isit.fraunhofer.de

Abstract: In this work, the first surface acoustic-wave-based magnetic field sensor using thin-film AlScN as piezoelectric material deposited on a silicon substrate is presented. The fabrication is based on standard semiconductor technology. The acoustically active area consists of an AlScN layer that can be excited with interdigital transducers, a smoothing SiO₂ layer, and a magnetostrictive FeCoSiB film. The detection limit of this sensor is 2.4 nT/√Hz at 10 Hz and 72 pT/√Hz at 10 kHz at an input power of 20 dBm. The dynamic range was found to span from about ±1.7 mT to the corresponding limit of detection, leading to an interval of about 8 orders of magnitude. Fabrication, achieved sensitivity, and noise floor of the sensors are presented.

Keywords: surface acoustic waves; surface acoustic wave sensor; magnetic field sensor; current sensor; magnetostriction; AlScN; FeCoSiB; MEMS; thin film



Citation: Meyer, J.M.; Schell, V.; Su, J.; Fichtner, S.; Yarar, E.; Niekietl, F.; Giese, T.; Kittmann, A.; Thormählen, L.; Lebedev, V.; et al. Thin-Film-Based SAW Magnetic Field Sensors. *Sensors* **2021**, *21*, 8166. <https://doi.org/10.3390/s21248166>

Academic Editor: Arcady Zhukov

Received: 29 October 2021

Accepted: 2 December 2021

Published: 7 December 2021

Publisher's Note: MDPI stays neutral with regard to jurisdictional claims in published maps and institutional affiliations.



Copyright: © 2021 by the authors. Licensee MDPI, Basel, Switzerland. This article is an open access article distributed under the terms and conditions of the Creative Commons Attribution (CC BY) license (<https://creativecommons.org/licenses/by/4.0/>).

1. Introduction

The sensing of magnetic fields has a multitude of use cases ranging from biomedical applications to current sensing in automotive applications [1–5], each having different requirements on the sensor regarding bandwidth, dynamic range, dc capability, size, and price [6,7].

A promising sensing principle of magnetic fields is based on surface acoustic waves (SAW) [8] and the change of the Young's modulus (ΔE effect) of magnetostrictive films [9]. This differs from other sensor approaches, such as using a magnetoelectric composite cantilever suffering from disadvantages such as a small bandwidth, and a good LOD that can only be achieved in resonance [10].

Today, for the fabrication of SAW sensors, the use of piezoelectric single-crystal substrates such as quartz [1,11,12] or LiNbO₃ [13,14] is state-of-the-art. For ST-cut quartz sensors, sensitivities of up to 2000°/mT and a limit of detection of 100 pT/Hz^{1/2} at 10 Hz are reached [15] and, for LiNbO₃, a variation of the SAW velocity of $\Delta v/v = 0.27\%$ at 400 mT [14]. To enable a greater material flexibility, especially in terms of compatibility with CMOS and MEMS technology, a reduction in chip size and the use of cleverly designed multilayers to enhance device performance requires a change to thin-film technology.

For that purpose, thin-film AlN is a promising piezoelectric material due to its high wave velocity, good mechanical and dielectric properties, high thermal conductivity, and high breakdown voltage [16]. Additionally, a SAW sensor operation up to several GHz can be realized, which can significantly increase the sensitivity in many sensor applications [17]. Further, it was shown that alloying AlN with Sc improves the electromechanical coupling significantly without losing the attractive material properties of AlN [18]. The electromechanical coupling in AlScN even increases with increasing frequency, so that its use is particularly interesting for high SAW frequencies [19,20]. The Sc concentration adds an additional parameter for tuning crucial properties of SAW devices, such as the phase velocity and the electromechanical coupling [20]. AlScN as a promising thin-film material

for SAW sensors, as it is described in [21], is studied in this work, and it can be fabricated at reasonable cost with standard semiconductor technology on larger wafer sizes and an easier process integration compared to bulk piezoelectric wafers.

For SAW devices, two common design approaches exist: a delay line, and a resonator configuration [22,23]. In this work, the delay line configuration is chosen, as shown in Figure 1, to increase the interaction volume between the excited wave and the magnetic field sensitive area (magnetostrictive film). For this purpose, two inter-digital transducers (IDTs) are structured on the acoustic layer (thin film AlScN) to excite and readout the SAW signal via the piezoelectric effect [24]. The delay line of length l is located between the two IDTs. To prevent a short circuit between the magnetostrictive film and the IDTs and, more importantly, to reduce the roughness of the underlaying layer of the magnetostrictive film, a SiO₂ layer is grown on top of the piezoelectric layer. The topmost layer in this area of the delay line is the magnetostrictive material FeCoSiB. The acoustic wave passing through the delay line couples to an external magnetic field via the induced change in the Young's modulus of the magnetostrictive film [9].

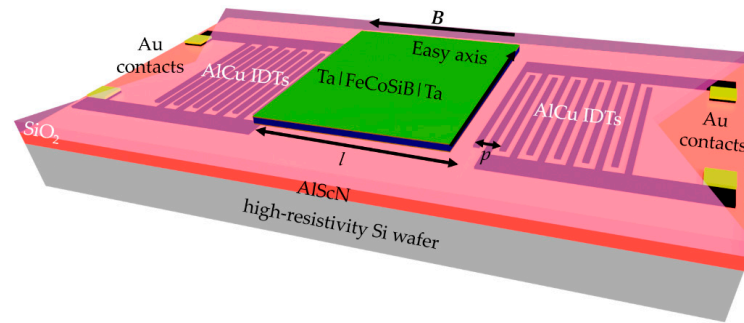


Figure 1. Schematic sketch of the SAW thin-film magnetic field sensor. Magnetostrictive FeCoSiB on top of the silicon dioxide layer of length l is in between the AlCu IDTs. FeCoSiB is capped with Ta to avoid corrosion. The easy axis of the magnetostrictive film defines the sensitive direction of the sensor against an external applied magnetic field B and is chosen to be perpendicular to the direction of SAW propagation. As the piezoelectric material, AlScN is chosen.

As the change of Young's modulus ΔE alters the phase velocity v of the acoustic wave [25], a B -field-induced phase change $\Delta\varphi = 2\pi l f / (v(B_1) - v(B_0))$ can be detected at the output IDTs via the direct piezoelectric effect [26]. The sensitivity of the sensor, which is defined as the phase change per change in magnetic field $S = \partial\varphi / \partial H$, can be written as the product of its individual contributions: magnetic layer sensitivity S_{mag} (change in Young's modulus with magnetic field), structural sensitivity S_{str} (change of the wave velocity with change in Young's modulus), and geometric sensitivity S_{geo} (phase change with change in wave velocity) [1]:

$$S = \frac{\partial\varphi}{\partial H} = \frac{\partial G}{\partial H} \cdot \frac{\partial v}{\partial G} \cdot \frac{\partial\varphi}{\partial v} = S_{mag} \cdot S_{str} \cdot S_{geo} \quad (1)$$

By means of S and the power spectral density S_φ of the random phase fluctuations of the sensor, the limit of detection (LOD) of the sensor can be calculated by [27]:

$$LOD = \frac{\sqrt{S_\varphi}}{S} \quad (2)$$

The logarithmic presentation of the power spectral density $10 \log_{10} (S_\varphi)$ is referred to as phase noise.

2. Materials and Methods

2.1. Sensor Fabrication

On a 200 mm, 725 μm thick, single-side polished high-resistivity Si (001) wafer, a 1 μm $\text{Al}_{0.77}\text{Sc}_{0.23}\text{N}$ layer is sputtered as described in [28].

Afterwards, 200 nm thick AlCu IDTs are sputtered and patterned by dry chloride etching to a design with a delay line length of $l = 3.8$ mm, a split-finger structure [29] of 25 pairs, a periodicity of $p = 16$ μm , and a finger width of 2 μm , resulting in a theoretical phase velocity of the Rayleigh-like mode of 283 MHz (Figure 2(1)). Three-hundred-nanometer-thick gold contacts with a 40 nm WTi adhesion layer are sputter-deposited and structured with a wet etching step (Figure 2(2)). A 1.5 μm thick, low-stress SiO_2 interlayer is deposited with plasma-enhanced chemical vapor deposition (PECVD) at 400 $^\circ\text{C}$ and smoothed and thinned with a chemical mechanical polishing (CMP) step to a thickness of 1 μm . An atomic force microscopy analysis showed that this reduces the surface roughness from 2 nm of the AlScN layer to a roughness of below 1 nm. Such a reduction significantly enhances the soft magnetic properties of the FeCoSiB thin film [30]. Afterwards, the layer is structured with dry etching (Figure 2(3)).

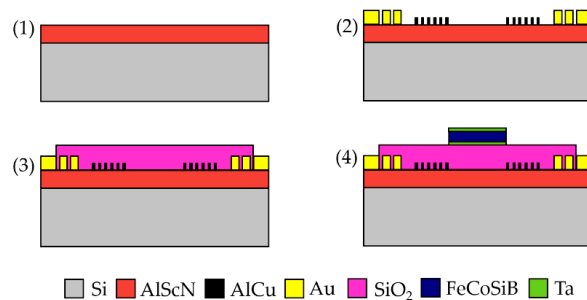


Figure 2. Schematic cross-sections of the processing steps of the thin film SAW sensor. (1) A layer of 1 μm AlScN is sputter-deposited on top of a high-resistance silicon (001) wafer, followed by 200 nm AlCu IDTs and 300 nm gold contacts with a 40 nm WTi adhesion layer that are patterned afterwards (2). A 1.5 μm SiO_2 layer is deposited via PECVD and thinned with CMP to a thickness of 1 μm (3). On top, the magnetostrictive FeCoSiB film with a thickness of 200 nm is deposited with an additional layer of 10 nm Ta on the top and on the bottom (4).

The magnetostrictive layer consisting of 200 nm $(\text{Fe}_{90}\text{Co}_{10})_{78}\text{Si}_{12}\text{B}_{10}$ is deposited via RF magnetron sputtering on top of the SiO_2 layer and structured with ion beam etching to realize steep and straight edges. To improve adhesion and prevent oxidation, 10 nm Ta is deposited on top and below the FeCoSiB film (Figure 2(4)). To induce a uniaxial magnetic anisotropy in the soft magnetic film, an annealing step at 250 $^\circ\text{C}$ for 30 min is performed while applying a magnetic field of 0.2 T. Thereby, the easy axis of the FeCoSiB film is aligned perpendicular to the SAW propagation direction (see Figure 1). The simple process of thermal alignment of the magnetization is an example of the integration-related advantages of the silicon substrate-based thin-film concept. When using single crystal piezoelectric substrates, such a simple thermal imprint is not possible due to anisotropic thermal expansion in the piezoelectric substrate and would result in a significant reduction of the soft magnetic film properties. Instead, a more complex, low-temperature deposition with an applied magnetic field must be applied to achieve a proper alignment of the magnetization [26]. Finally, the sensor is glued and wire-bonded on top of a printed circuit board (PCB), on which there are balun devices to symmetrize the signal. The final sensor is shown in the inset of Figure 3.

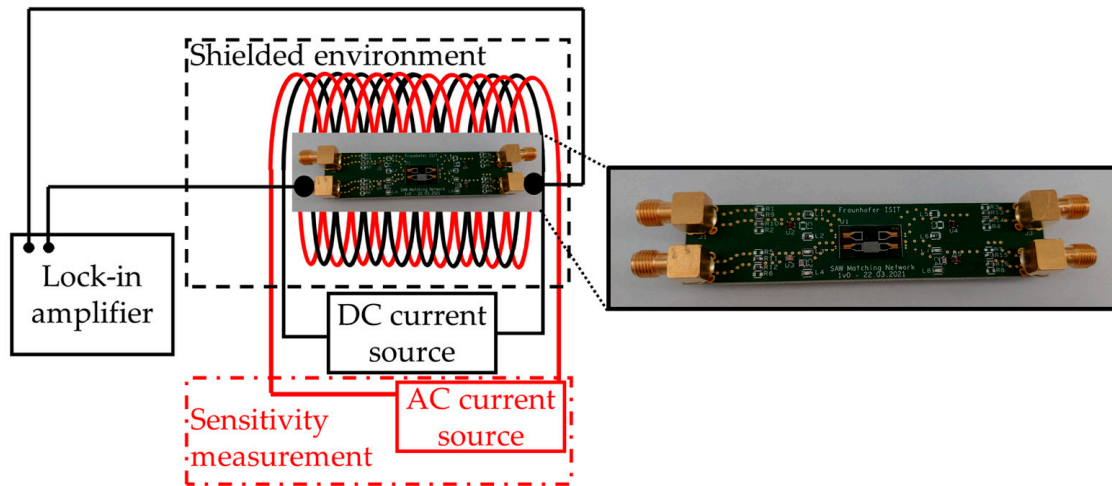


Figure 3. Sketch of the measurement setup. The SAW sensor is placed in a magnetically, electrically, and acoustically shielded measurement chamber inside of two solenoids. For the phase shift measurements, only a dc current source is used to apply a homogeneous magnetic field. A lock-in amplifier is used to apply the synchronous SAW frequency and measure the phase change. The sensitivity S is measured by applying an additional ac magnetic field using the second solenoid that is supplied with another current source using a test amplitude and frequency. The inset shows a zoom-in of the ready-to-use sensor with a balun attached to symmetrize the signal.

2.2. Experimental Setup

The sensor's two-port scattering parameters (S-parameters) are characterized with a vector network analyzer E8361A from Agilent Technologies. A signal power of $p = 0$ dBm is used throughout the experiments in this paper, except for the noise measurements. For all measurements in a magnetic field, the sensor is placed in the center of two axially stacked coils, which are used to generate ac and dc magnetic signals by means of a programmable current source (KEPCO BOP20-10ML) for the dc magnetic field. The solenoids are placed inside a magnetically, electrically, and acoustically shielded measurement chamber. The magnetic field shielding is provided by a mu-metal cylinder ZG1 from Aaronia AG to prevent external influences. The magnetically induced phase shift of the sensor is measured in the homogeneous magnetic field region of the solenoids. To then record the sensor behavior in the magnetic field, the magnetic flux density is swept from negative to positive values and reversed. A lock-in amplifier (UHFLI from Zurich Instruments) is used to apply the synchronous SAW frequency determined by the measurement of the S-parameters and to measure the static phase response $\varphi(B)$ of the sensor at a chosen input power (here 0 dBm).

In order to determine the sensor's optimum working point with the highest sensitivity, the phase φ is analyzed as a function of a dc bias field H . In principle, a numerical calculation of the sensitivity $S = \partial\varphi/\partial H$ should be sufficient to determine the point of steepest slope, which refers to the point of highest sensitivity, but often small phase jumps related to domain wall movement can give the appearance of incorrectly high sensitivities. Therefore, a dynamic phase detection measurement is performed to accurately determine $\partial\varphi/\partial H$ at every single measurement point. For this, one solenoid generates the static magnetic bias field that is superimposed with an ac test-field generated with the second solenoid powered by a current source (Keithley 6221) with a defined amplitude of $10 \mu\text{T}$ and a frequency of 10 Hz. By choosing the amplitude of the ac field that is large enough, the phase fluctuations can be neglected. The sensor's output signal and the phase reference are fed into the UHFLI lock-in amplifier that is used as a phase demodulator. The phase sensitivity is obtained by the evaluation of the amplitude spectrum of the demodulated phase signal [26].

The phase noise measurements are performed with the Rohde & Schwarz FSWP phase noise analyzer at the sensor's magnetic working point and at magnetic saturation at a different sensor's input power. The SAW sensor is placed in the electrically, magnetically, and acoustically shielded chamber during these measurements. To minimize external noise sources, especially those appearing in common dc current sources, a battery-based current source controlled by a potentiometer is applied in series with the solenoids for the generation of the dc magnetic bias field. The internal generator of the phase noise analyzer excites the sensor at the synchronous SAW frequency determined in previous measurements. The LOD can be determined from the measured noise floor with Equation (2). A more detailed description of the measurement setup can be found in [27].

3. Sensor Characterization

A finite element method (FEM) analysis and spectra analysis were performed using COMSOL Multiphysics® software [31] based on the acoustic and electromagnetic parameters of the constituent layers (AlScN, SiO₂, FeCoSiB). The parameters for AlScN were taken from [21] and for FeCoSiB from [1]. The simulated admittance and the displacement of the SAW modes are shown in Figure 4a. A Rayleigh-like thin-film mode is simulated to be at 283 MHz with a high admittance and relatively high displacement that are defined on the surface with some energy losses in the direction of the Si substrate (see Figure 4b).

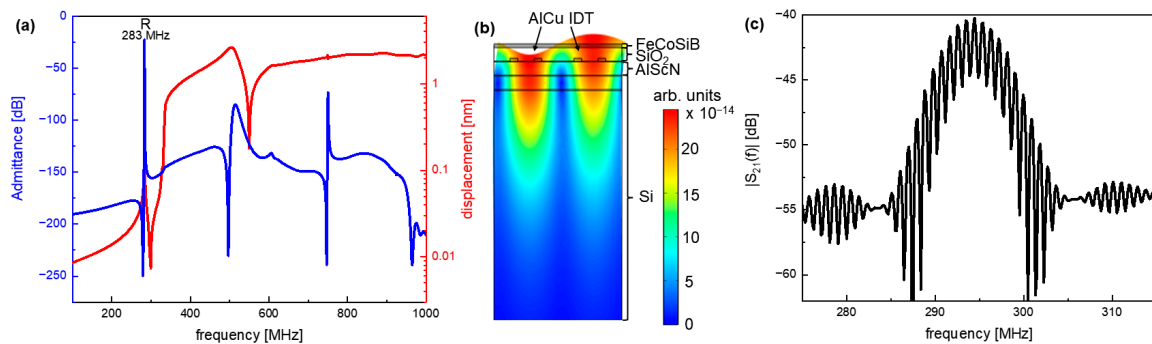


Figure 4. (a) FEM-simulated displacement (red) and admittance (blue) for the presented sensor design. (b) Colored map of absolute deflection for the Rayleigh-like mode at 283 MHz. The deflection into the FeCoSiB layer, the SiO₂ intermediate layer, the IDTs, the AlScN layer, and the Si substrate are displayed. (c) Measured transmission behavior (scattering parameter S₂₁) of the presented sensor. The synchronous frequency of the sensor is determined to be 294.2 MHz with a return loss of 40 dB.

The measured transmission behavior of the thin-film magnetic field sensor is shown in Figure 4c, exhibiting a synchronous frequency of 294.2 MHz at zero flux density, which is very close to the simulated value. The deviation can be explained by the material parameters in the simulation deviating from the experimental parameters in the real sensor, or imperfections in the fabrication, and is assessed as low.

The performance of the sensor in a magnetic field is measured as described above by applying the synchronous frequency of 294.2 MHz with the lock-in amplifier and measuring the static phase response of the sensor shown in Figure 5a from negative to positive field values (black) and reverse (grey). A slight hysteresis is observable, as was expected, resulting from the magnetic material. The linear region of the static phase response, which determines the dynamic range, is marked with a blue line in Figure 5a.

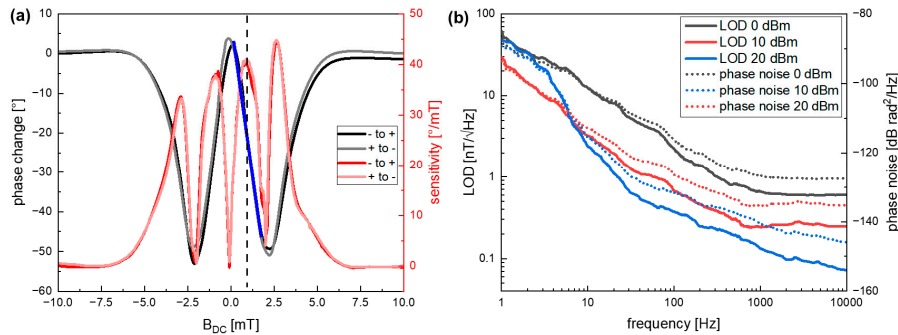


Figure 5. (a) The induced phase shift in the sensor with an external magnetic flux density (black) and the direct measurement of the sensitivity with an ac test signal (red) is shown. The highest slope in the phase change occurs at about 0.85 mT and 2.65 mT, resulting in the highest values of sensitivity of up to $45^\circ/\text{mT}$. A value of 0.85 mT is chosen as a working point (indicated with the dotted line) due to the high sensitivity and the lower field value compared to 2.65 mT. The dynamic range of the sensor is marked with the blue line, showing the linear region of the sensor. The ac signal has an amplitude of $10\ \mu\text{T}$ and a frequency of 10 Hz. (b) Measured phase noise (dotted line) and calculated limit of detection (solid line) as a function of the frequency at magnetic saturation for 0 dBm (black), 10 dBm (red), and 20 dBm (blue) input power.

The sensitivity that is given by the derivative of the phase change as described above is important for the performance of the sensor. The dynamically measured sensitivity via an ac test signal depending on the bias field is shown in Figure 5a (red). The two regions with the maximum phase change are observed at about 0.85 mT and 2.65 mT (Figure 5a) and are the most interesting for sensor application. The highest sensitivity of about $45^\circ/\text{mT}$ is reached at 2.65 mT.

Besides a high sensitivity, a good LOD is an important sensor parameter of the SAW sensor [15]. The LOD dependency on frequency from the carrier and sensor input power is shown in Figure 5b. The measurements are performed at the sensor's working point at $H_{bias} = 0.85\ \text{mT}$, which is chosen due to the technological limitation of the LOD measurement setup and at magnetic saturation. As both measurements are almost identical, only the measurement at saturation is shown in Figure 5b.

Up to a frequency of 1 kHz, a regime of flicker ($1/f$) noise dominates the spectra. This noise is related to defects in the substrate and the SiO_2 layer, as well as random fluctuations of the magnetization and magnetic hysteresis losses [27]. In the specific case of SiO_2 , additional surface roughness is introduced during the ion beam etching step to pattern the FeCoSiB layer. A possible way to reduce this roughness would be to add a lift-off process, though this would have the disadvantage of less defined edges of the magnetostrictive film.

In the $1/f$ noise regime, a LOD of $3.2\ \text{nT}/\text{Hz}^{1/2}$ is achieved at 10 Hz and an input power of 10 dBm. Above 1 kHz, the noise is dominated by white noise, which is additive noise and decreases with increasing signal power [27]. Here, a LOD of $246\ \text{pT}/\text{Hz}^{1/2}$ is reached for 10 kHz. When the input power is increased to 20 dBm, the LOD can be decreased even further at higher frequencies above 10 Hz so that a LOD of $2.4\ \text{nT}/\text{Hz}^{1/2}$ can be reached at 10 Hz and $72\ \text{pT}/\text{Hz}^{1/2}$ at 10 kHz.

The dynamic range of the sensor is given by the linear region around the working point of the sensor and is indicated in Figure 5a with the blue line. It spans from about 1.7 mT to the corresponding LOD, leading to an interval of 8 orders of magnitude. The hysteretic behavior could be compensated as is done in AMR sensors (anisotropic magnetoresistance) with controlled current pulses [32].

With these characteristics, our sensor has already high potential for sensing a wide range of technically relevant electrical currents via the generated magnetic field. In contrast, other current sensor concepts, such as Hall sensors, are limited in the bandwidth in the needed dynamic range and cannot achieve the measurement of fast signals [33]. AMR sensors also have a limit of the bandwidth at 1 MHz and a low dynamic range [34]. The presented SAW

sensor is dc-compatible with a moderately high bandwidth of about 1.2 MHz limited by the delay line length and a high dynamic range of about 8 orders of magnitude.

4. Conclusions

The first thin-film SAW magnetic field sensor using AlScN as piezoelectric material on a silicon substrate is presented. The limit of detection is $2.4 \text{ nT/Hz}^{1/2}$ at 10 Hz, which probably can be lowered further with an impedance matching, higher input power values, and further insights on the sensor design and noise sources. This will also have a high impact on the phase change and the resulting sensitivity of the sensors. At higher frequencies above 10 kHz, the LOD is found to be as low as $72 \text{ pT/Hz}^{1/2}$. Additionally, the magnetic layer can be optimized by an exchange bias [35] to eliminate the need for an external bias field. Due to the possibility to measure galvanically isolated values from dc up to MHz with a high dynamic of up to 8 orders of magnitude, the presented sensor is very interesting for a variety of modern measuring tasks, such as the control of modern power switches, where it is well suited for monolithic wafer-level integration circuits. This clearly sets it apart from the competition in the segment of galvanically isolated magnetic field sensors for power transformers in the field of electromobility, which include Hall sensors and AMR sensors. Thus, this sensor concept has the potential to manage the rising requirements on current sensors regarding bandwidth, dynamic range, precision, and compactness.

Author Contributions: Conceptualization, J.M.M., J.S., S.F., V.L., S.M., A.Ž. and F.L.; methodology, F.N., F.L., V.L. and J.M.M.; software, J.M.M., T.G. and F.N.; validation, J.M.M., V.S. and T.G.; formal analysis, J.M.M., S.F., V.L., S.M. and F.L.; investigation, J.M.M., V.S., T.G., V.L., S.M. and E.Y.; resources, A.Ž., A.K., L.T., E.Q. and F.L.; data curation, J.M.M.; writing—original draft preparation, J.M.M.; writing—review and editing, F.L., V.S., S.F., F.N., V.L., A.Ž. and S.M.; visualization, J.M.M.; supervision, F.L. and E.Q.; project administration, J.M.M., F.L., V.S., E.Q. and A.Ž.; funding acquisition, F.L., E.Q. and A.Ž. All authors have read and agreed to the published version of the manuscript.

Funding: This research was funded by the German Research Foundation (Deutsche Forschungsgemeinschaft, DFG) through the project A9 of the Collaborative Research Centre CRC 1261 ‘Magnetoelectric Sensors: From Composite Materials to Biomagnetic Diagnostics’. This work was partly funded by the BMBF under the project reference numbers 16FMD01K, 16FMD02, 16FMD03. Additionally, this work was supported by the Fraunhofer Internal Programs under Grand No. MAVO 840 173.

Institutional Review Board Statement: Not applicable.

Informed Consent Statement: Not applicable.

Data Availability Statement: The data presented in this study are available on reasonable request from the corresponding author.

Conflicts of Interest: The authors declare no conflict of interest. The funders had no role in the design of the study; in the collection, analyses, or interpretation of data; in the writing of the manuscript; or in the decision to publish the results.

References

- Kittmann, A.; Durda, P.; Zabel, S.; Reermann, J.; Schmalz, J.; Spetzler, B.; Meyners, D.; Sun, N.X.; McCord, J.; Gerken, M.; et al. Wide band low noise love wave magnetic field sensor system. *Sci. Rep.* **2018**, *8*, 278. [[CrossRef](#)] [[PubMed](#)]
- Lenz, J.; Edelstein, S. Magnetic sensors and their applications. *IEEE Sens. J.* **2006**, *6*, 631–649. [[CrossRef](#)]
- Sternickel, K.; Braginski, A.I. Biomagnetism using SQUIDS: Status and perspectives. *Supercond. Sci. Technol.* **2006**, *19*, S160. [[CrossRef](#)]
- Williamson, S.J.; Hoke, M. *Advances in Biomagnetism*; Springer Science & Business Media: Berlin, Germany, 2012.
- Zuo, S.; Schmalz, J.; Ozden, M.O.; Gerken, M.; Su, J.; Niekie, F.; Lofink, F.; Nazarpour, K.; Heidari, H. Ultrasensitive magnetoelectric sensing system for pico-tesla magnetomyography. *IEEE Trans. Biomed. Circuits Syst.* **2020**, *14*, 971–984. [[CrossRef](#)]
- Ziegler, S.; Woodward, R.C.; Lu, H.H.C.; Borle, L.J. Current sensing techniques: A review. *IEEE Sens. J.* **2009**, *9*, 354–376. [[CrossRef](#)]
- Labrenz, J.; Bahr, A.; Durda, P.; Höft, M.; Kittmann, A.; Schell, V.; Quandt, E. Frequency Response of SAW Delay Line Magnetic Field/Current Sensor. *IEEE Sens. Lett.* **2019**, *3*, 1500404. [[CrossRef](#)]
- Webb, D.; Forester, D.; Ganguly, A.; Vittoria, C. Applications of amorphous magnetic-layers in surface-acoustic-wave devices. *IEEE Trans. Magn.* **1979**, *15*, 1410–1415. [[CrossRef](#)]

9. Ludwig, A.; Quandt, E. Optimization of the Delta E effect in thin films and multilayers by magnetic field annealing. *IEEE Trans. Magn.* **2002**, *38*, 2829–2831. [CrossRef]
10. Su, J.; Niekietl, F.; Fichtner, S.; Kirchhof, C.; Meyners, D.; Quandt, E.; Wagner, B.; Lofink, F. Frequency tunable resonant magnetoelectric sensors for the detection of weak magnetic field. *J. Micromech. Microeng.* **2020**, *30*, 075009. [CrossRef]
11. Liu, X.; Tong, B.; Ou-Yang, J.; Yang, X.; Chen, S.; Zhang, Y.; Zhu, B. Self-biased vector magnetic sensor based on a Love-type surface acoustic wave resonator. *Appl. Phys. Lett.* **2018**, *113*, 082402. [CrossRef]
12. Yokokawa, N.; Tanaka, S.; Fujii, T.; Inoue, M. Love-type surface-acoustic waves propagating in amorphous iron-boron films with multilayer structure. *J. Appl. Phys.* **1992**, *72*, 360–366. [CrossRef]
13. Ganguly, A.; Davis, K.; Webb, D.; Vittoria, C.; Forester, D. Magnetically tuned surface-acoustic-wave phase shifter. *Electron. Lett.* **1975**, *11*, 610–611. [CrossRef]
14. Yamaguchi, M.; Hashimoto, K.; Kogo, H.; Naoe, M. Variable SAW delay line using amorphous TbFe₂ film. *IEEE Trans. Magn.* **1980**, *16*, 916–918. [CrossRef]
15. Kittmann, A.; Müller, C.; Durdaut, P.; Thormählen, L.; Schell, V.; Niekietl, F.; Lofink, F.; Meyners, D.; Knöchel, R.; Höft, M.; et al. Sensitivity and noise analysis of SAW magnetic field sensors with varied magnetostrictive layer thicknesses. *Sens. Actuators A Phys.* **2020**, *311*, 111998. [CrossRef]
16. Dubois, M.A.; Murali, P. Properties of aluminum nitride thin films for piezoelectric transducers and microwave filter applications. *Appl. Phys. Lett.* **1999**, *74*, 3032–3034. [CrossRef]
17. Caliendo, C.; Imperatori, P. High-frequency, high-sensitivity acoustic sensor implemented on ALN/Si substrate. *Appl. Phys. Lett.* **2003**, *83*, 1641–1643. [CrossRef]
18. Fichtner, S.; Wolff, N.; Krishnamurthy, G.; Petraru, A.; Bohse, S.; Lofink, F.; Chemnitz, S.; Kohlstedt, H.; Kienle, L.; Wagner, B. Identifying and overcoming the interface originating c-axis instability in highly Sc enhanced AlN for piezoelectric microelectromechanical systems. *J. Appl. Phys.* **2017**, *122*, 035301. [CrossRef]
19. Ding, A. Surface Acoustic Wave Devices Based on C-Plane and A-Plane AlScN. Ph.D. Thesis, Albert-Ludwigs-Universität Freiburg, Freiburg im Breisgau, Germany, 2020.
20. Kurz, N.; Ding, A.; Urban, D.F.; Lu, Y.; Kirste, L.; Feil, N.M.; Žukauskaitė, A.; Ambacher, O. Experimental determination of the electro-acoustic properties of thin film AlScN using surface acoustic wave resonators. *J. Appl. Phys.* **2019**, *126*, 075106. [CrossRef]
21. Wang, W.; Mayrhofer, P.M.; He, X.; Gillinger, M.; Ye, Z.; Wang, X.; Bittner, A.; Schmid, U.; Luo, J. High performance AlScN thin film based surface acoustic wave devices with large electromechanical coupling coefficient. *Appl. Phys. Lett.* **2014**, *105*, 133502. [CrossRef]
22. Slobodnik, A.J. Surface acoustic waves and SAW materials. *Proc. IEEE* **1976**, *64*, 581–595. [CrossRef]
23. Bell, D.T.; Li, R.C. Surface-acoustic-wave resonators. *Proc. IEEE* **1976**, *64*, 711–721. [CrossRef]
24. White, R.M.; Voltmer, F.W. Direct piezoelectric coupling to surface elastic waves. *Appl. Phys. Lett.* **1965**, *7*, 314–316. [CrossRef]
25. Smole, P.; Ruile, W.; Korden, C.; Ludwig, A.; Quandt, E.; Krassnitzer, S.; Pongratz, P. Magnetically tunable SAW-resonator. In Proceedings of the IEEE International Frequency Control Symposium and PDA Exhibition Jointly with the 17th European Frequency and Time Forum, Tampa, FL, USA, 4–8 May 2003; pp. 903–906.
26. Schell, V.; Müller, C.; Durdaut, P.; Kittmann, A.; Thormählen, L.; Lofink, F.; Meyners, D.; Höft, M.; McCord, J.; Quandt, E. Magnetic anisotropy controlled FeCoSiB thin films for surface acoustic wave magnetic field sensors. *Appl. Phys. Lett.* **2020**, *116*, 073503. [CrossRef]
27. Durdaut, P.; Müller, C.; Kittmann, A.; Schell, V.; Bahr, A.; Quandt, E.; Knöchel, R.; Höft, M.; McCord, J. Phase Noise of SAW Delay Line Magnetic Field Sensors. *Sensors* **2021**, *21*, 5631. [CrossRef]
28. Lu, Y.; Reusch, M.; Kurz, N.; Ding, A.; Christoph, T.; Kirste, L.; Lebedev, V.; Žukauskaitė, A. Surface morphology and microstructure of pulsed DC magnetron sputtered piezoelectric AlN and AlScN thin films. *Phys. Status Solidi A* **2018**, *215*, 1700559. [CrossRef]
29. Holland, M.G.; Claiborne, L.T. Practical surface acoustic wave devices. *Proc. IEEE* **1974**, *62*, 582–611. [CrossRef]
30. Piorra, A.; Jahns, R.; Teliban, I.; Gugat, J.; Gerken, M.; Knochel, R.; Quandt, E. Magnetoelectric thin film composites with interdigital electrodes. *Appl. Phys. Lett.* **2013**, *103*, 032902. [CrossRef]
31. COMSOL Multiphysics®v. 5.6. COMSOL AB, Stockholm, Sweden. Available online: <https://www.comsol.com> (accessed on 11 November 2020).
32. Xie, F.; Weiss, R.; Weigel, R. Hysteresis compensation based on controlled current pulses for magnetoresistive sensors. *IEEE Trans. Ind. Electron.* **2015**, *62*, 7804–7809. [CrossRef]
33. Popovic, R.S.; Randjelovic, Z.; Manic, D. Integrated Hall-effect magnetic sensors. *Sens. Actuators A Phys.* **2001**, *91*, 46–50. [CrossRef]
34. Ripka, P. Electric current sensors: A review. *Meas. Sci. Technol.* **2010**, *21*, 112001. [CrossRef]
35. Spetzler, B.; Bald, C.; Durdaut, P.; Reermann, J.; Kirchhof, C.; Teplyuk, A.; Meyners, D.; Quandt, E.; Höft, M.; Schmidt, G.; et al. Exchange biased delta-E effect enables the detection of low frequency pT magnetic fields with simultaneous localization. *Sci. Rep.* **2021**, *11*, 5269. [CrossRef] [PubMed]

3.4 Exchange Biased SAW Magnetic Field Sensors

The noise in SAW magnetic field sensors is stemming from domain wall activated processes. Namely, these are domain wall nucleation, domain wall movement or domain wall annihilation and the interaction of acoustic waves with these. Reducing domain walls or suppressing their formation can be achieved by different means, one of them is being the application of exchange bias of a ferromagnetic film via coupling to an antiferromagnetic film. Thermal treatment of quartz-based sensors leads to a degradation of sensor performance, therefore top pinned exchange bias systems are applied. Herein, the ferromagnetic film is deposited in a magnetic field and the antiferromagnet will have its magnetic moments aligned by the ferromagnetic layer when deposited on top.

In the layer system FeCoSiB/NiFe/MnIr the exchange bias field H_{EB} is comparably low, thus the thickness of the FeCoSiB cannot be increased above 100 nm, since the demagnetization field H_{demag} will exceed H_{EB} . Therefore, two exchange bias stacks are deposited subsequently, but with opposite bias directions, i.e. an antiparallel exchange bias is induced. This way the stray fields are closed between the two stacks and thus H_{demag} is reduced. Reducing the formation of domain walls causes a decrease in phase noise. Further, this noise is dependent on the sensor's excitation power, exhibiting minimum $1/f$ noise at excitation powers between 5 dBm and 10 dBm. The limit of detection correlates with the phase noise, therefore LODs as low as 28 pT/ $\sqrt{\text{Hz}}$ at 10 Hz and 10 pT/ $\sqrt{\text{Hz}}$ at 100 Hz were achieved. These are the lowest values reported for SAW magnetic field sensors at the time of submission and are a further step towards biomagnetic applications.

Author Contributions

Own contribution to the manuscript:

- Fabrication of samples (large fraction)
- Measurements and preparation of samples (large fraction)
- Interpretation of results (large fraction)
- Preparation of figures (large fraction)
- Data analysis (large fraction)
- Writing of manuscript (large fraction)
- Designing experiments (shared)

Manuscript submitted for publication.

Exchange Biased Surface Acoustic Wave Magnetic Field Sensors

Viktor Schell¹, Elizaveta Spetzler², Niklas Wolff³, Lars Bumke¹, Lorenz Kienle³, Jeffrey McCord², Eckhard Quandt¹ & Dirk Meyners^{1a)}

Affiliations

¹ Inorganic Functional Materials, Institute for Materials Science, Kiel University, Kiel 24143, Germany.

² Nanoscale Magnetic Materials – Magnetic Domains, Institute for Materials Science, Kiel University, Kiel 24143, Germany.

³ Synthesis and Real Structure, Institute for Materials Science, Kiel University, Kiel 24143, Germany.

^{a)} Author to whom correspondence should be addressed: dm@tf.uni-kiel.de

Magnetoelastic composites which use surface acoustic waves show great potential as sensors of low frequency and extremely low amplitude magnetic fields like those found in biomagnetic applications. While these sensors provide adequate frequency bandwidth for most applications, their detectability has found its limitation in the low frequency noise generated by the magnetoelastic film. Amongst other contributions, this noise is closely connected to domain wall activity evoked by the strain from the acoustic waves propagating through the film. A successful method to reduce the presence of domain walls in the first place, is to couple the ferromagnetic material with an antiferromagnetic material across their interface and therefore induce an exchange bias, which is unidirectional in nature. In this work we demonstrate the application of a top pinning exchange bias stack consisting of ferromagnetic layers of $(\text{Fe}_{90}\text{Co}_{10})_{78}\text{Si}_{12}\text{B}_{10}$ and $\text{Ni}_{81}\text{Fe}_{19}$ coupled to an antiferromagnetic $\text{Mn}_{80}\text{Ir}_{20}$ layer. The exchange bias is set directly by a magnetic field applied during the deposition of the films without any post-deposition heat treatment. Additionally, stray field closure and hence prevention of magnetic edge domain formation is achieved by an antiparallel biasing of two consecutive exchange bias stacks. The set antiparallel alignment of magnetization of the magnetostrictive FeCoSiB layers provides single domain states over the complete films. This results in a reduction of magnetic phase noise and therefore provides limits of detection as low as 28 pT/Hz^{1/2} at 10 Hz and 10 pT/Hz^{1/2} at 100 Hz, a factor of 2.5 lower than comparable non-exchange biased sensors.

As early as in the 1960s, David Cohen conducted pioneering magnetic measurements of human heart signals using a simple coil [1]. Due to obvious limitations in spatial and signal resolution he later switched to more sophisticated methods, taking advantage of the then newly emerging superconducting quantum interference devices (SQUID) [2,3]. This new approach pathed the way for magnetocardiography and magnetoencephalography as we know it today. However, the (re-)search for miniaturized, economical and easy to use alternatives for the SQUID systems has been going on ever since. While for magnetoencephalography applications the development seems to be heading towards optically pumped magnetometers as a real alternative [4], the position as the successor for SQUID-based magnetocardiography is still disputed. Different alternative sensor concepts are currently considered, such as optically pumped magnetometers [5,6], fluxgate magnetometers [7,8], sensors based on magnetoresistive effects [9,10] or magnetoelectric composites [11]. All of them having their own advantages and disadvantages regarding detection limit, frequency bandwidth, measurement range, spatial resolution, power consumption, lifetime and the necessity for magnetic shielding. All these criteria and the performance of the sensor system as a whole have to be considered to estimate its true capability for biomagnetic diagnostics [12].

Surface acoustic wave (SAW) magnetic field sensors have only recently gained interest as magnetometers for minimal magnetic fields through the combination of Love wave devices with amorphous magnetostrictive thin films [13]. Their

operation principle is based on the generation of high frequency acoustic waves on a piezoelectric substrate by interdigital transducers (IDTs). Using specific cuts of the piezoelectric single crystal substrates in combination with a guiding layer of lower acoustic wave velocity leads to the generation of Love waves [14]. The larger the difference of the mechanical properties between the substrate and the guiding layer is, the stronger is the confinement of the acoustic wave at the guiding layer's surface [15]. This confinement has the advantage compared to other wave modes such as Rayleigh waves, that influences on the sensors surface have a larger impact on the propagating acoustic waves. Such influences can be magnetic fields if the SAW devices are coated with a magnetoelastic film, hence enabling magnetic field sensing capabilities. The sensing principle is based on the delta-E effect, which describes the non-linear change of elastic moduli with magnetization in a magnetostrictive material due to the presence of magnetostrictive strain in addition to the conventional elastic strain of the material [16]. The effective stiffness change changes the velocity of the acoustic waves and leads to a phase shift of the output signal. This change in phase is then proportional to the measured magnetic field amplitude. Different materials and SAW designs have been proposed [17,18], even solely thin film based SAW magnetic field sensors on silicon wafers have been demonstrated [19]. Particularly high sensitivities can be reached by applying magnetically soft magnetostrictive films with a well-aligned magnetic anisotropy and with a low anisotropy energy density K_u [20]. Their large frequency bandwidth [21] makes delay line SAW sensors also promising for the localization and rotational orientation detection of implanted deep brain stimulation electrodes [22].

In SAW based magnetic field sensors the additional noise at low frequencies and low excitation powers has been identified to stem from magnetic losses, which are expressed as the imaginary part μ_r'' of the complex permeability [23]. These losses are associated with characteristic $1/f$ flicker phase noise and depend on the magnetic domain and anisotropy configuration, the magnetic bias field H_{DC} and the power P_{SAW} (i.e. the strain acting on the magnetic material) which the SAW sensor is excited with. It was shown that there are complex and manifold interactions between the propagating Love waves and the domain walls within the magnetostrictive film giving rise to potential phase fluctuations leading to noise [24]. Also, for different types of magnetic field sensors such as giant magnetoimpedance (GMI) [25] or giant magnetoresistance (GMR) [26,27] based devices it was shown that domain wall activated processes lead to $1/f$ low frequency noise. Additional losses can occur specifically in SAW based sensors due to domain wall resonances which are in the frequency range of typical SAW devices [28]. In general, magnetization noise, or more precise the power spectral density of thermally excited magnetization fluctuations S_M is directly proportional to the effective magnetic losses μ_r'' according to the fluctuation-dissipation theorem and is given by

$$S_M(f) = \frac{4k_B T \mu_r''(f)}{2\pi f V \mu_0} \quad (1)$$

where k_B is the Boltzmann constant, T the absolute temperature, f the offset frequency, V the magnetic volume and μ_0 vacuum permeability [23,29]. Taking the change of magnetization during SAW operation into account the more applicable and measurable power spectral density of phase fluctuations S_ϕ can be derived, which is

$$S_\phi(f) = S(H_{DC}, P_{SAW})^2 \frac{4k_B T \mu_0 \mu_r''(f, H_{DC}, P_{SAW})}{2\pi f V (\mu_r'(f, H_{DC}, P_{SAW}))^2} \quad (2)$$

with S being the phase change with change of applied magnetic field, i.e. the sensors sensitivity and μ_r' the real part of the complex permeability [23].

$1/f$ -type noise in magnetic film-based magnetic field sensors is significantly influenced by fluctuations due to magnetic domain wall processes. Therefore, it is desirable to eliminate domain walls in the magnetic films to improve the sensors' performance. One way to achieve this is by biasing a ferromagnetic material by a coupled antiferromagnetic material. This type of exchange interaction is termed exchange bias and was discovered by Meiklejohn and Bean in the year 1957 [30]. It is associated with a shift of the magnetization loop against an exchange bias field H_{EB} which is given by

$$H_{EB} = \frac{J_{EB}}{M_S t_{FM} \mu_0} \quad (3)$$

with the exchange bias energy density J_{EB} , the saturation magnetization M_S and the thickness of the ferromagnetic layer t_{FM} [31].

Especially for spintronic devices such as GMR recording heads the biasing of one of the two ferromagnetic layers by an antiferromagnet lead to a large improvement in device performance through the increase in sensitivity [31–33]. In GMR as well as tunnel magnetoresistance (TMR) devices exchange bias is used for the pinning of one of the ferromagnetic layers of the synthetic antiferromagnet [34,35]. In magnetoelectric composites exchange bias has been successfully applied for shifting the maximum of the magnetoelectric coefficient to zero field, eliminating the need of an external bias field [36]. Additionally, exchange biasing of ferromagnetic layers can be utilized to reduce magnetic noise in ME composites caused by domain wall nucleation, movement, and annihilation [37,38], which could be further improved by an antiparallel biasing of consecutive layers [39]. The only two exchange bias system applied to SAW devices so far are Co/MnIr as the IDT material [40] and CoFeB/MnIr [41]. However, the goal of both studies was not to achieve noise suppression. On piezoelectric substrates elevated temperatures cause in-plane uniaxial stresses in the magnetostrictive film due to the anisotropic expansion of the substrate. This stress leads to high anisotropy fields H_K and consequently to a severe reduction of sensor performance [20]. Therefore, the exchange bias in this study is only induced by an external magnetic field applied during the growth of the film stack and the sample is rotated by 180° inside the magnetic field after the deposition of a single layer (SL) stack to achieve antiparallel (AP) exchange bias.

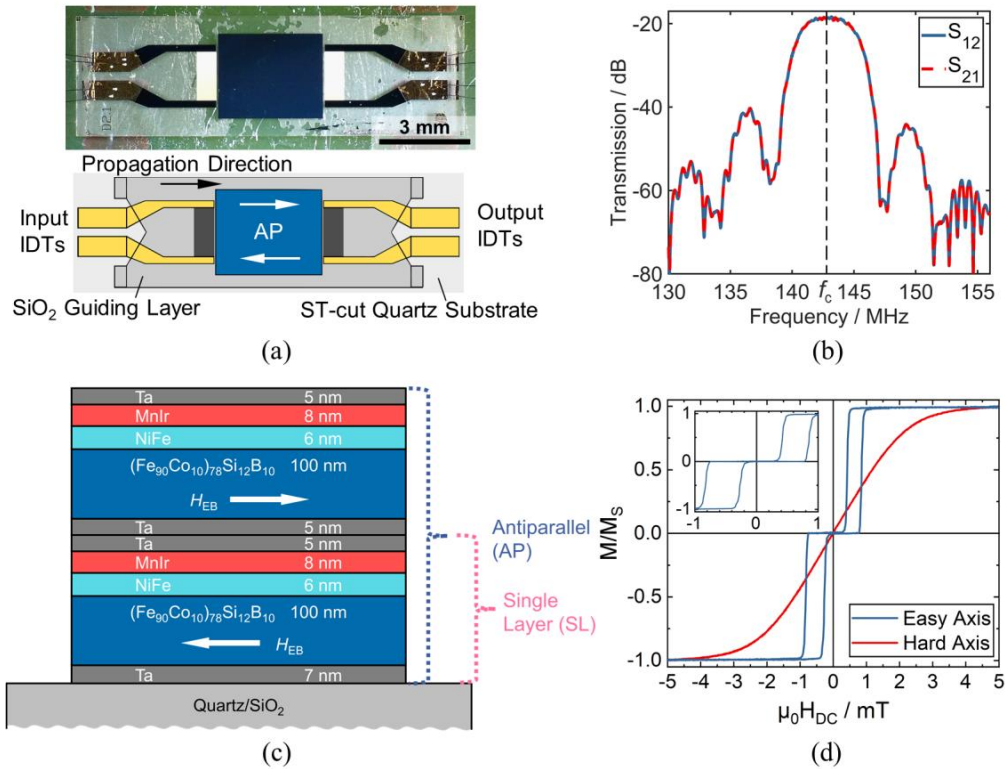


Fig. 1 | SAW device and exchange bias film stack. **a**, Top-view photograph and schematic of the Love wave device with a $4 \mu\text{m}$ SiO_2 guiding layer. The device is mounted on a PCB with pressure sensitive tape and connected to that PCB by wire bonding. **b**, Scattering parameters S_{12} and S_{21} of the device showing a synchronous frequency of $f_c = 142.6 \text{ MHz}$ and an insertion loss at that frequency of -18.5 dB . The sensor was magnetically saturated perpendicular to the propagation direction. **c**, Antiparallel top-pinning exchange bias stack. **d**, Volumetric magnetization loops of the AP exchange bias stack recorded by a BH loop tracer along the easy (blue) and hard axis (red) of magnetization of a circular sample of diameter $d = 13.8 \text{ mm}$ on a ST-cut quartz substrate. The inset shows the easy axis loop in the range of -1 mT to 1 mT .

SAW Device and Exchange Bias System

A photograph and a schematic of the SAW device under investigation is shown in Fig. 1a. All samples are based on ST-cut quartz with the propagation direction 90° to the crystallographic X-axis, along which shear horizontal waves are excited [14]. The 200 nm thick Au split finger IDTs consist each of 25 finger pairs with a width of $3.5 \mu\text{m}$ and spacing

of 3.5 μm , which in total creates a pitch distance and therefore an acoustic wavelength of $\lambda = 28 \mu\text{m}$. Adhesion layers of 8 nm Cr are beneath and above the Au. The acoustic aperture i.e. the width of the acoustic wave front corresponds to 60λ . The measured scattering parameters S_{21} and S_{12} of the sensor under investigation after impedance matching are shown in Fig. 1b. It is magnetically saturated perpendicular to the SAW propagation direction. The sensor exhibits a synchronous frequency of 142.6 MHz and an insertion loss in magnetic saturation of -18.5 dB . Both are determined mainly by the SiO_2 guiding layer's thickness, which is 4 μm in this case and mechanical properties with respect to the substrate. The exchange bias stack consisting of two sequences of $\text{Ta}/(\text{Fe}_{90}\text{Co}_{10})_{78}\text{Si}_{12}\text{B}_{10}/\text{Ni}_{81}\text{Fe}_{19}/\text{Mn}_{80}\text{Ir}_{20}/\text{Ta}$ is shown in Fig. 1c. The FeCoSiB layers are biased in opposite direction i.e., antiparallel to achieve flux closure and hence prevent the formation of closure domains. As the sample is removed from vacuum after the first deposition step the top Ta layer oxidizes in air. Hence, to still provide adhesion for the FeCoSiB of the second deposition step an additional Ta layer is deposited on the oxidized Ta. The topmost Ta layer acts as passivation layer for MnIr. The magnetization loops of the antiparallel exchange bias stack along the easy (parallel to propagation direction) and hard axis (perpendicular to propagation direction) of magnetization are shown in Fig. 1d. The sample was in this case a circle with diameter $d = 13.8 \text{ mm}$ which was structured by lift-off. The magnetic field during deposition was also applied 90° to the crystallographic X-axis as it is done for the SAW devices. Antiparallel shifts of the easy axis hysteresis loop can be observed corresponding to exchange bias fields of $\mu_0 H_{\text{EB,l}} = 0.5 \text{ mT}$ (l for left hand side shift) and $\mu_0 H_{\text{EB,r}} = -0.6 \text{ mT}$ (r for right hand side shift). In comparison to samples with similar thicknesses of the ferromagnetic and antiferromagnetic layers, but in which the bottom-pinned exchange bias was induced by annealing in a magnetic field, our samples show an about four times smaller exchange-bias strength [39]. However, for the system $\text{Ni}_{81}\text{Fe}_{19}/\text{Mn}_{78}\text{Ir}_{22}$ the exchange bias energy is, according to (3), $J_{\text{EB,NiFe}} = 70 \mu\text{J}/\text{m}^2$ [42], which is comparable to this system with each stack exhibiting coupling energies of $J_{\text{EB,l}} = 61 \mu\text{J}/\text{m}^2$ and $J_{\text{EB,r}} = 73 \mu\text{J}/\text{m}^2$, respectively with $M_S = 1.45 \text{ T}$. The coercivity fields of the two hysteresis loop branches are $\mu_0 H_{\text{C,l}} = 0.27 \text{ mT}$ and $\mu_0 H_{\text{C,r}} = 0.22 \text{ mT}$, respectively. This only small difference in coercivity could be explained by a slight tilt of the anisotropies of the two layers with respect to each other. Along the hard axis of magnetization no measurable hysteresis is observed. The anisotropy field of this system on ST-cut quartz is found to be $\mu_0 H_k = 1.7 \text{ mT}$ which is only slightly higher than in non-exchange biased FeCoSiB with 1.5 mT [20] and the total anisotropy field, which is the sum of H_k and H_{EB} is $\mu_0 H_{\text{k,tot}} = 2.3 \text{ mT}$.

Structural Characterization

Fig. 2a shows a noise-filtered high-resolution TEM micrograph from a section of a single layer exchange bias stack. The FeCoSiB layer is amorphous as intended, only at the interface to NiFe crystalline regions are observed. However, at the interface a clear distinction between the two layers is not possible. The layers of NiFe and MnIr are polycrystalline containing nanosized grains with poor $\{111\}$ texture along the growth direction. Localized elemental analysis by energy-dispersive X-ray spectroscopy (EDS) mapping in Fig. 2b is conducted for validation of the layer thicknesses and the elemental distribution across the stack, e.g. to examine potential intermixing. Mostly, the average thicknesses of all functional layers matched with the anticipated target thickness, considering that there are no sharp transitions between the layers which limits the resolution. This smearing of the elemental distribution across the interfaces is apparent from the elemental map, showing exemplary Mn, Ni and Fe signals, as well as the quantified profiles of all metallic elements averaged across the mapped region. This feature is especially prominent for the broad and diffuse $(\text{Fe}_{90}\text{Co}_{10})_{78}\text{Si}_{12}\text{B}_{10}/\text{Ni}_{81}\text{Fe}_{19}$ interface, featuring the apparent decrease of Fe content in the NiFe layer. However, as the stoichiometry of the NiFe layer should be 81:19, the observed Fe profile can be interpreted as the overlap of the extended signal scattering background from Fe in the FeCoSiB layer and a Gaussian-profile of Fe in $\text{Ni}_{81}\text{Fe}_{19}$. Noteworthy, a significant degree of roughness at the NiFe/MnIr interface is observed from high-resolution investigations, which could rationalize the overlap of localized X-ray intensities, as well as sample thickness, which leads to X-ray signal delocalization. It was shown that roughness can have an influence on exchange bias and coercivity fields [43].

For sufficient and reliable exchange bias when using MnIr as the antiferromagnetic material a $\{111\}$ texture of the MnIr is beneficial [44]. In order to adjust this texture of MnIr, NiFe is acting as a supporting seed layer. However, the relation between MnIr texture and exchange bias field is complex and even contradicting findings have been reported [45]. The X-ray diffractograms in Fig. 2c reveal that this texture is present with a MnIr 111 reflection at 41.1° . Even using a NiFe thickness of 3 nm the same MnIr 111 reflection intensity is present. In fact, NiFe layers with thicknesses of 3 nm and 6 nm both result in the same exchange bias fields (not shown), but for reproducibility aspects a higher thickness was chosen for this study.

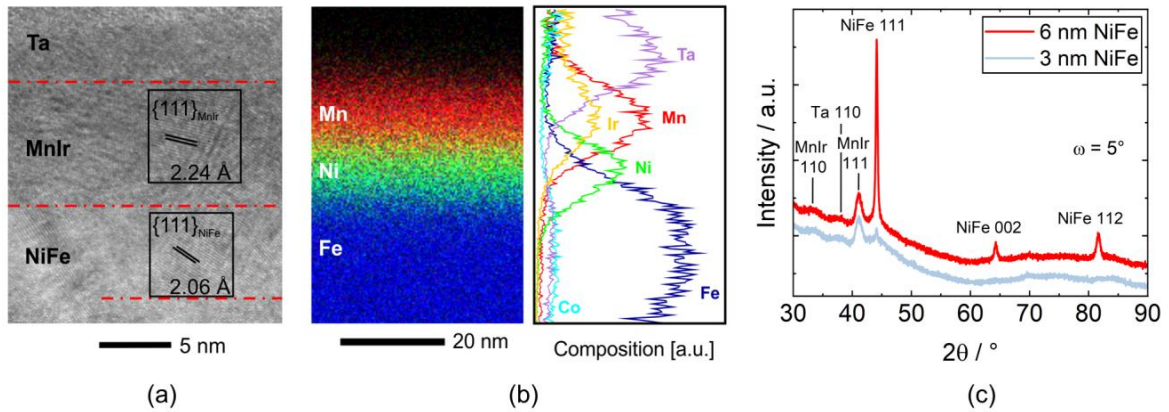


Fig. 2 | TEM investigation and X-ray diffraction of a section of a SL exchange bias stack. a. High resolution TEM image of a single exchange bias stack with 6 nm NiFe. **b.** EDS elemental map and quantified profiles across the functional top layers. **c.** Diffractograms of the SL stack with two different NiFe thicknesses. The incident angle was kept constant at $\omega = 5^\circ$ to only penetrate the thin films and not the single crystal substrate.

Sensor Response

An essential sensor property is its sensitivity to the respective measurand. In the case of delay line SAW magnetic field sensors the sensitivity is the relation of the phase change to the amplitude of an applied magnetic field. In all sensors based on magnetic materials this sensitivity is dependent on the magnetization state of that material which can be altered by an external magnetic DC field. The phase change of a SAW sensor with antiparallel exchange bias as a function of applied DC magnetic field is shown in Fig. 3a. It follows the characteristic change of the shear modulus of a magnetostrictive material under shear SAW excitation where the easy axis magnetization is parallel to the propagation direction and perpendicular to the DC magnetic field [46]. The total phase change between magnetic saturation and the minimum at about -0.05 mT amounts to 770° . Sweeping the magnetic field from -10 mT to $+10$ mT and vice versa results in very little hysteresis, which indicates a remagnetization process governed dominantly by coherent magnetization rotation rather than domain wall motion (see Fig. 4c). The two curves are shifted with respect to each other by only up to $25 \mu\text{T}$. Additionally, the minima of each curve are slightly shifted indicating a small tilt of the magnetic anisotropies with respect to the propagation direction. The SAW sensor's measured sensitivity is shown in Fig 3b. It is obtained by applying a $1 \mu\text{T}$ modulation field of 10 Hz and at each measurement point the phase at 10 Hz is read out and divided by the $1 \mu\text{T}$ AC field. The sensitivity also represents the derivative of the phase change and therefore the sensitivity maxima in Fig. 3b correspond to the points of highest slope in Fig. 3a. These maxima are at -0.4 mT and at 0.28 mT with sensitivities of $2040 \text{ }^\circ/\text{mT}$ and $1920 \text{ }^\circ/\text{mT}$, respectively. Despite that the samples have a lower hard axis magnetic permeability than the comparable SAW devices based on the same magnetostrictive material and same thickness, but without exchange bias, they show similar sensitivities [20].

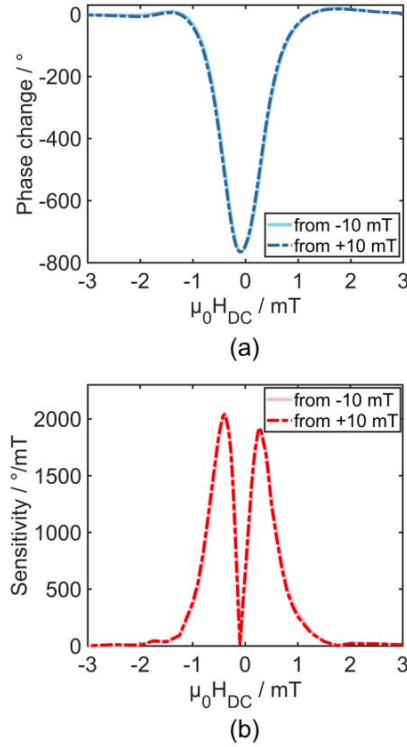


Fig. 3 | Phase response and sensitivity. **a**, Phase change as a function of applied DC bias field $\mu_0 H_{DC}$ of the Love wave sensor with AP exchange bias. **b**, The sensor's measured sensitivity as a function of applied DC bias field. In both measurements the excitation power was 10 dBm (10 mW) and the magnetic field was applied perpendicular to the SAW propagation direction, i.e. the exchange bias axis.

Magneto-optical Imaging

The goal of exchange biasing the FeCoSiB layers is to achieve a single domain state in the magnetic thin film. Stacking two or more magnetic flux compensating exchange biased layers with antiparallel aligned magnetization reduces the total demagnetizing field energy of the sample and therefore suppresses the formation of closure domains [39]. In the case of complete closure of magnetic flux, a single domain state at remanence can be achieved. To verify that single domain state of FeCoSiB in the antiparallel exchange bias stack magneto-optical Kerr effect (MOKE) microscopy imaging has been conducted. Fig. 4 shows a comparison of the magnetic states of 200 nm plain FeCoSiB (Fig. 4a) and a 2×100 nm antiparallel exchange bias sample (Fig. 4b). In Fig. 4b only the top layer is visible, which is additionally covered by the MnIr and NiFe layers leading to less MOKE contrast in this image. Before both images were taken the magnetic film was demagnetized by an AC magnetic field with decaying amplitude of which the initial amplitude was high enough to saturate the films. The demagnetizing field H_{decay} was applied along the hard axis of magnetization to achieve a magnetic ground state. Without exchange bias thin straight domains are formed with a high domain wall density. Additionally, characteristic closure domains form at the edges [47]. In contrast, the top layer in the antiparallel biased system shows a single domain state. This is underlined in Fig. 4c, which shows MOKE contrast images of the same antiparallel exchange biased sensor, but in this $\mu_0 H_{DC}$ was changed from -5 mT to 5 mT (shown are images from -2 mT to 2 mT) along the hard axis of magnetization. This is the same axis as in the hard axis loop in Fig. 1d and in the bias curves in Fig. 3. No magnetic domains form during the remagnetization process without excitation, confirming the anticipated coherent magnetization rotation in the structured sensor.

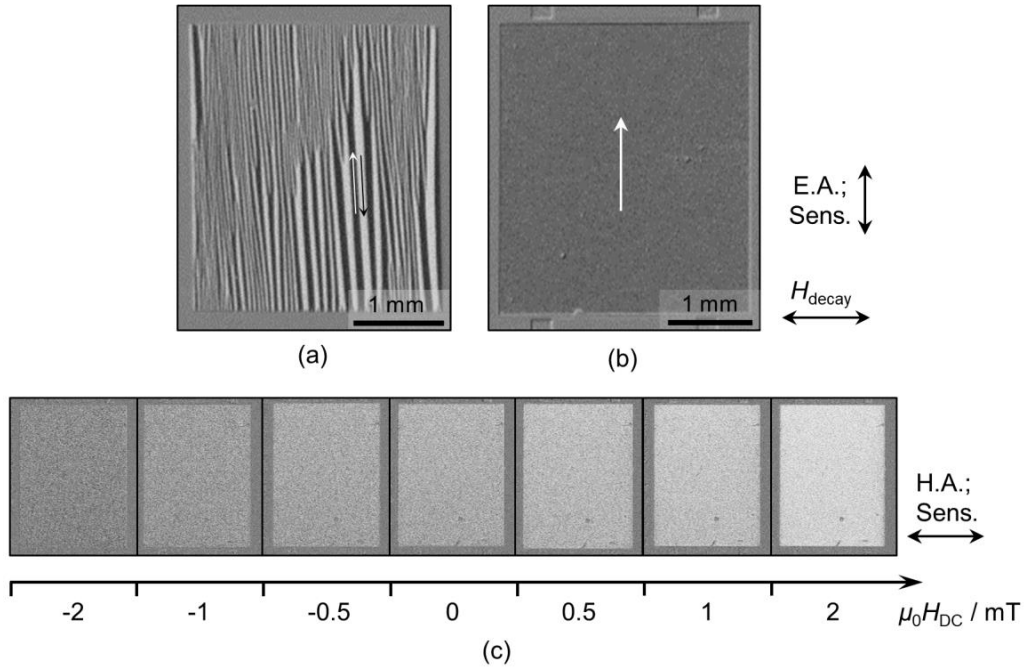


Fig. 4 | Magneto-optical Kerr effect microscopy images. **a**, A 200 nm single layer of FeCoSiB. **b**, The top layer of antiparallel exchange biased 2x100 nm FeCoSiB. Both samples have been demagnetized by an decaying AC magnetic field H_{decay} along the hard axis of magnetization. The sensitivity axis of the MOKE microscope was vertically i.e. along the easy axis of magnetization, which is also the SAW propagation direction. **c**, The top layer of antiparallel exchange biased 2x100 nm FeCoSiB in which the applied field was changed stepwise from -5 mT to 5 mT (shown are only images from -2 mT to 2 mT) along the hard axis of magnetization while also the MOKE sensitivity was set along this axis. The gray area around the FeCoSiB layers is the non-ferromagnetic SiO_2 layer. In **b** also parts of the input and output IDTs can be seen through the SiO_2 layer.

SAW Sensor Performance

For a single magnetic layer SAW device it was shown that, in general, with increasing excitation power the flicker phase noise in SAW magnetic field sensors is decreasing, as also the effective losses, i.e. μ_r'' are decreasing [23]. However, this only holds true up to a certain excitation power. With increasing excitation random Barkhausen domain wall jumps occur, which at high enough excitation power amplitudes become the dominant source of noise, causing so called random walk of phase noise exhibiting $1/f^2$ behavior. Consequently, the SAW sensors' excitation power dependency in a single domain system is investigated. First, Fig. 5a shows the sensitivity of an antiparallel exchange biased sensor as a function of DC bias field for different excitation powers. It shows that even applying powers as high as 15 dBm the magnetic field dependency does not change significantly. Typical excitation powers for SAW magnetic field sensors are around 0 dBm [23]. In fact, with increasing power the sensitivity curves even become more symmetric, i.e. the sensitivity values at the maxima become equal and the peaks of maximum sensitivity slightly shift to higher fields. Both effects can be explained by the additional effective magnetic anisotropy caused by the oscillating shear stress. However, with severely higher excitation powers the shape of the sensitivity curves changes. Apart from the main maxima at small magnetic field values and additional change in shape as small "humps" occur at around -0.4 mT/ 0.4 mT. The drastic increase in sensitivity at smaller magnetic bias fields suggests an altered remagnetization mechanism with higher magnetic permeability which is not present as significantly at lower powers. For visualization the maximum sensitivities are plotted against different excitation powers in Fig. 5d.

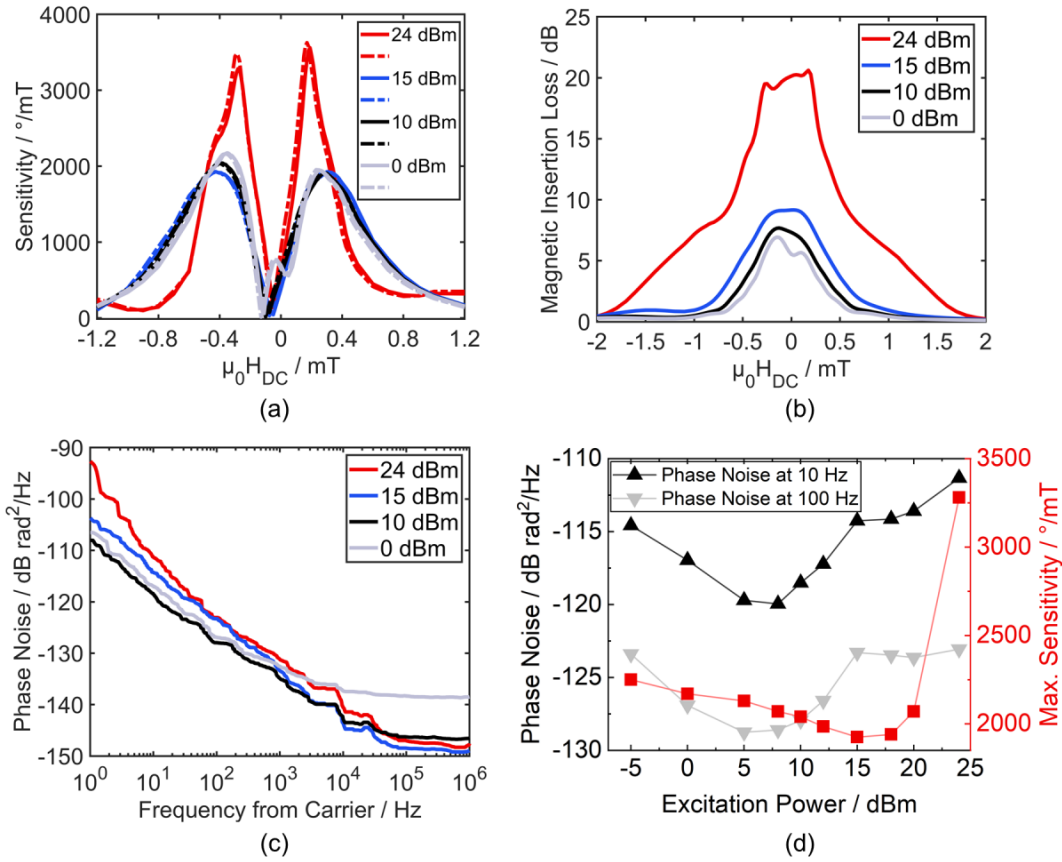


Fig. 5 | Power dependency of the antiparallel exchange biased SAW sensor's performance. **a**, Sensitivity as a function of applied magnetic DC bias field swept from -10 mT to $+10$ mT (full lines) and vice versa (dashed lines) for different excitation powers. Only the region of high sensitivity from -1.2 mT to $+1.2$ mT is shown. **b**, Magnetically induced insertion loss as a function of applied DC magnetic field for different excitation powers measured from -10 mT to $+10$ mT. The losses are normalized to 0 dB, where 0 dB then corresponds the insertion loss in magnetic saturation. **c**, Phase noise spectra of the same sensor at different excitation powers. For every excitation power a DC bias field was applied which corresponds to the point of highest sensitivity. **d**, Phase noise at 10 Hz and 100 Hz and the respective maximum sensitivity as a function of excitation power.

In Fig. 5b magnetically induced additional insertion losses relative to the insertion losses in magnetic saturation at the respective excitation powers are shown as a function of applied DC bias fields for different excitation powers. The additional magnetic insertion losses show a maximum at around zero magnetic field for all excitation powers. Analogous to the sensitivity in Fig. 5a also the losses first become more symmetric around zero magnetic field and strongly increase at high excitation amplitudes. In previous studies magnetic insertion losses have been connected with the increased presence of domain walls [24]. A clear correlation between additional magnetic insertion loss and magnetically induced phase noise has also been observed [23]. There in a simple layer of FeCoSiB phase noise is highest where the insertion loss is maximum at a constant excitation power. Comparing Fig. 5a and Fig. 5b shows that at lower powers the sensitivity maxima are not correlating with high insertion losses. Only at high powers such as 24 dBm the sensitivity maxima correspond to the two minor peaks in magnetic insertion loss at -0.28 mT and 0.19 mT in Fig. 5b. Here, Fig. 5c reveals that the phase noise is only correlating with magnetic insertion losses to a certain degree. It shows the power spectral density of phase fluctuations i.e. the phase noise as a function of frequency next to the excitation carrier for different excitation powers. While the insertion losses increase continuously with excitation power, the phase noise first decreases and then increases again. This is visualized in Fig. 5d showing the phase noise at 10 Hz and 100 Hz as a function of excitation power. It clearly reveals a region where the phase noise is minimized, which is between 5 dBm and 10 dBm.

Compared to non-exchange biased FeCoSiB-based SAW sensors higher excitation powers can be applied before the increases [23]. Additionally, the noise increase is not as drastic with higher powers, suggesting other noise source mechanisms rather than random Barkhausen jumps. Therefore, compared to non-exchange biased SAW sensors the noise is 8 dB lower [20]. One potential noise source is the temperature generated during SAW excitation with elevated power [48,49]. In our devices we found an increase of temperature of 14 °C from room temperature at an excitation power of 24 dBm (not shown). According to Equations (2) this will lead to an increase of $1/f$ phase noise. Additionally, the oscillating shear strain from the acoustic wave can potentially cause magnetization fluctuations in the film leading to noise. In [24] the shear stress generated by the wave amplitude was estimated from the change in MOKE contrast to be $\tau = 3.29$ MPa at 10 dBm excitation. Assuming a shear modulus of FeCoSiB of $G = 28.1$ GPa [50] the acting shear strain at 10 dBm excitation can be estimated as $\gamma_{10\text{dBm}} = 0.06$ ‰. At 24 dBm the excitation amplitude is about 5 times higher leading to estimated shear strains of $\gamma_{24\text{dBm}} = 0.3$ ‰ under the assumption that the strain is increasing linearly with excitation amplitude, which is proportional to the square root of the excitation power. In the case of Love waves the oscillating shear strain is acting 45° with respect to the magnetic easy axis and triggers an oscillation of the magnetization. However, the specific mechanisms require further investigation.

The limit of detection (LOD) which is the ratio of phase noise and sensitivity [13] is shown in Fig. 6a for different excitation power at 10 Hz and 100 Hz. Since the sensitivity is barely changing up to excitation powers of 18 dBm the LOD follows the same trend as the phase noise, with the lowest LODs between 5 dBm and 8 dBm of 28 pT/Hz^{1/2} at 10 Hz and 10 pT/Hz^{1/2} at 100 Hz. This is an improvement by a factor of 2.5 compared to the very best non-exchange biased SAW sensors so far [20]. At higher excitation powers from 15 dBm on the LOD is almost constant as the noise increases in the same amount as the sensitivity. The lowest LOD at 5 dBm excitation is shown Fig. 6b up to a frequency of 10 kHz, as in this range the sensitivity of the sensor is constant [21]. From 1 kHz on the LOD is even below 5 pT/Hz^{1/2}.

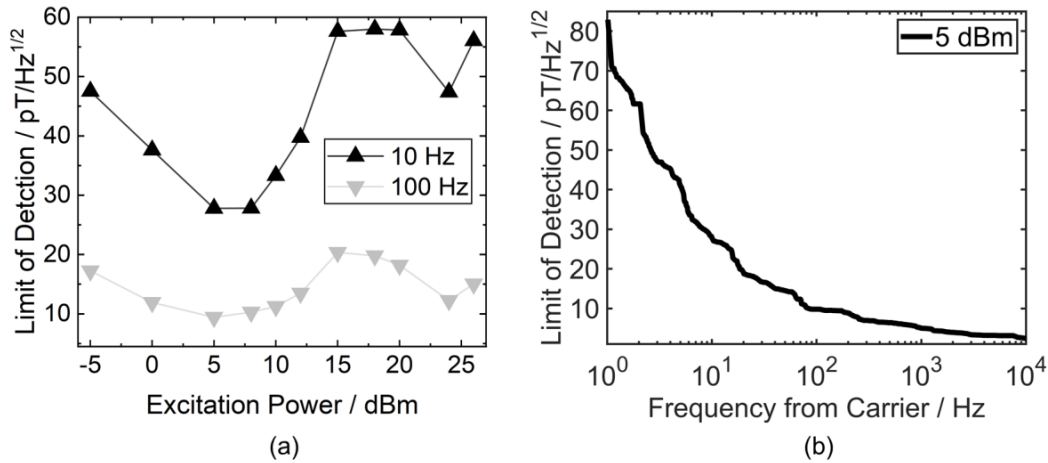


Fig. 6 | Limits of detection (LOD). **a**, LOD as a function of excitation power at 10 Hz and 100 Hz off the carrier frequency. **b**, Frequency spectrum of the lowest LOD at 5 dBm excitation power.

Conclusions

A top pinning exchange bias stack consisting of ferromagnetic layers of Ni₈₁Fe₁₉ and magnetostrictive (Fe₉₀Co₁₀)₇₈Si₁₂B₁₀ and antiferromagnetic Mn₈₀Ir₂₀ on Love wave SAW devices was presented. An antiparallel biasing of two exchange bias stacks was achieved by applying a magnetic field during deposition and by rotating the sample between depositions. The NiFe seed layer provides a 111 texture of the MnIr layer, inducing an exchange bias which is high enough to provide a single domain state over the complete magnetic film. The bias curves of the SAW sensors exhibit small hysteresis and due to the elimination of domain walls the magnetic $1/f$ phase noise was reduced by about 8 dB compared to non-exchange biased sensors. However, it was also shown that despite the likely absence of domain walls, there is an excitation power dependency of the phase noise. At high excitation power amplitudes $1/f$ noise

increases which makes further investigations necessary to distinguish between different noise contributions. Overall, a substantial improvement of the limit of detection of SAW magnetic field sensors by a factor of 2.5 was achieved.

Methods

Sample and device fabrication. Au IDTs of 200 nm thickness with 8 nm Cr adhesion layers on top and bottom are deposited by DC magnetron sputtering and structured by photolithography and ion beam etching. Subsequently, a 4 μm thick SiO_2 layer is deposited by means of plasma-enhanced chemical vapor deposition (PECVD) acting as a guiding layer. Parts of the SiO_2 are removed again by inductively coupled plasma reactive ion etching to provide access to the contact pads for wire bonding of the final sensor to a printed circuit board (PCB). The deposition of the antiparallel top pinning exchange bias stack is performed in two steps. First, layers of Ta (7 nm)/ $(\text{Fe}_{90}\text{Co}_{10})_{78}\text{Si}_{12}\text{B}_{10}$ (100 nm)/ $\text{Ni}_{81}\text{Fe}_{19}$ (6 nm)/ $\text{Mn}_{80}\text{Ir}_{20}$ (8 nm)/Ta (5 nm) are deposited while a magnetic field of ~ 60 mT is present which is applied parallel to the SAW propagation direction. Afterwards, the samples are removed from the vacuum chamber, rotated by 180° with regards to the magnetic field and a second sequence of layers is deposited consisting of Ta (5 nm)/FeCoSiB (100 nm)/NiFe (6 nm)/MnIr (8 nm)/Ta (5 nm). For magnetic and structural characterization single layer (SL) stacks have been fabricated as well with 6 nm and 3 nm thick NiFe. The depositions of FeCoSiB and NiFe are done by RF magnetron sputtering and of Ta and MnIr by DC magnetron sputtering. The geometrical delay line structure of the exchange bias layers is provided via lift-off.

Structural characterization. A cross-section of a single exchange bias stack is prepared by the focused ion-beam (FIB) method and investigated using transmission electron microscopy (TEM). High-resolution micrographs of the NiFe and MnIr crystalline layers are recorded on a Tecnai F30 G² STWIN microscope. Elemental mapping using energy-dispersive X-ray spectroscopy (EDS) of the functional layers is performed in scanning mode on a JEOL NeoARM. X-ray diffractograms are obtained using a Rigaku SmartLab 9 kV X-ray diffractometer with CuK_α ($\lambda = 1.5406 \text{ \AA}$) radiation.

Magnetic characterization and MOKE microscopy. Magnetic domain images are gathered with a large view magneto-optical Kerr effect (MOKE) microscope. Homogeneous illumination of the sample is achieved by a combination of a high-power LED source (520 nm wavelength) with a telecentric lens. A Scheimpflug CCD camera mount is used for getting an even focus across the large sample area. Volumetric magnetic hysteresis loops are recorded with an inductive BH loop tracer.

Sensor characterization. The sensor is wire bonded to a PCB and its impedance is matched to 50Ω on each port. Scattering parameters are measured with a vector network analyzer while the sensor is magnetically saturated perpendicular to the SAW propagation direction. Magnetic sensor characterizations are performed within a zero-gauss-chamber to eliminate influences from earth's magnetic field and surrounding laboratory equipment. DC and AC magnetic fields are provided by two solenoids, respectively, while for dynamic phase detection a $1 \mu\text{T}$ sinusoidal AC signal of 10 Hz is applied. In the experiments all magnetic fields are applied along the hard axis of magnetization, i.e. perpendicular to the SAW propagation direction. For excitation and read out a Zurich Instruments UHFLI lock-in amplifier is used. To apply higher power amplitudes than the 7.5 dBm maximum power provided by the UHFLI a ZFL-2500VH+ power amplifier from Mini Circuits is used which provides a gain of 24 dB and has a noise level of $-138 \text{ dB rad}^2/\text{Hz}$ at 10 Hz and $-152 \text{ dB rad}^2/\text{Hz}$ at 1 kHz when applying 0 dBm. For noise measurements a Rohde&Schwarz FSWP phase noise analyzer is used while the same ZFL-2500VH+ power amplifier provides higher power amplitudes and a step attenuator smaller power step sizes. As a source for the DC bias fields during noise measurements an in-house built battery-based potentiometer-controlled low-noise source is used.

Author contributions

All authors interpreted the data, discussed the results, reviewed, and commented on the manuscript. D.M., E.Q., J.M. and L.K. designed experiments and supervised the research. V.S. wrote the manuscript, fabricated samples, created figures and conducted sensor-related measurements. E.S. performed MOKE imaging and contributed to figures. N.W. performed TEM/EDS measurements, contributed to figures and wrote segments of the manuscript. L.B. conducted XRD measurements.

Declaration of Competing Interests

The authors declare no competing interests.

Acknowledgements

The authors would like to thank the German Research Foundation (Deutsche Forschungsgemeinschaft, DFG) who funded this work through the collaborative research center CRC 1261 "Magnetolectric Sensors: From Composite Materials to Biomagnetic Diagnostics". Also, the authors thank Phillip Durdaut for providing MATLAB readout scripts.

References

- [1] D. Cohen, Magnetic Fields around the Torso: Production by Electrical Activity of the Human Heart, *Science* 156 (1967) 652–654. <https://doi.org/10.1126/science.156.3775.652>.
- [2] D. Cohen, Measurements of the magnetic fields produced by the human heart, brain, and lungs, *IEEE Transactions on Magnetics* 11 (1975) 694–700. <https://doi.org/10.1109/TMAG.1975.1058698>.
- [3] D. Cohen, Magnetic fields of the human body, *Physics Today* 28 (1975) 34–43. <https://doi.org/10.1063/1.3069110>.
- [4] E. Boto, N. Holmes, J. Leggett, G. Roberts, V. Shah, S.S. Meyer, L.D. Muñoz, K.J. Mullinger, T.M. Tierney, S. Bestmann, G.R. Barnes, R. Bowtell, M.J. Brookes, Moving magnetoencephalography towards real-world applications with a wearable system, *Nature* 555 (2018) 657–661. <https://doi.org/10.1038/nature26147>.
- [5] S. Morales, M.C. Corsi, W. Fourcault, F. Bertrand, G. Cauffet, C. Gobbo, F. Alcouffe, F. Lenouvel, M. Le Prado, F. Berger, G. Vanzetto, E. Labyt, Magnetocardiography measurements with ^4He vector optically pumped magnetometers at room temperature, *Phys. Med. Biol.* 62 (2017) 7267–7279. <https://doi.org/10.1088/1361-6560/aa6459>.
- [6] T. Sander, A. Jodko-Władzińska, S. Hartwig, R. Brühl, T. Middelman, Optically pumped magnetometers enable a new level of biomagnetic measurements, *Advanced Optical Technologies* 9 (2020) 247–251. <https://doi.org/10.1515/aot-2020-0027>.
- [7] H. Karo, I. Sasada, Magnetocardiogram measured by fundamental mode orthogonal fluxgate array, *Journal of Applied Physics* 117 (2015) 17B322. <https://doi.org/10.1063/1.4918958>.
- [8] M. Janosek, M. Butta, M. Dressler, E. Saunderson, D. Novotny, C. Fourie, 1-pT Noise Fluxgate Magnetometer for Geomagnetic Measurements and Unshielded Magnetocardiography, *IEEE Trans. Instrum. Meas.* 69 (2020) 2552–2560. <https://doi.org/10.1109/TIM.2019.2949205>.
- [9] M. Pannetier-Lecoer, L. Parkkonen, N. Sergeeva-Chollet, H. Polovy, C. Fermon, C. Fowley, Magnetocardiography with sensors based on giant magnetoresistance, *Appl. Phys. Lett.* 98 (2011) 153705. <https://doi.org/10.1063/1.3575591>.
- [10] Y. Shirai, K. Hirao, T. Shibuya, S. Okawa, Y. Hasegawa, Y. Adachi, K. Sekihara, S. Kawabata, Magnetocardiography Using a Magnetoresistive Sensor Array, *Int. Heart J.* 60 (2019) 50–54. <https://doi.org/10.1536/ihj.18-002>.
- [11] J. Reermann, P. Durdaut, S. Salzer, T. Demming, A. Piorra, E. Quandt, N. Frey, M. Höft, G. Schmidt, Evaluation of magnetoelectric sensor systems for cardiological applications, *Measurement* 116 (2018) 230–238. <https://doi.org/10.1016/j.measurement.2017.09.047>.
- [12] E. Elzenheimer, C. Bald, E. Engelhardt, J. Hoffmann, P. Hayes, J. Arbustini, A. Bahr, E. Quandt, M. Höft, G. Schmidt, Quantitative Evaluation for Magnetoelectric Sensor Systems in Biomagnetic Diagnostics, *Sensors (Basel)* 22 (2022). <https://doi.org/10.3390/s22031018>.
- [13] A. Kittmann, P. Durdaut, S. Zabel, J. Reermann, J. Schmalz, B. Spetzler, D. Meyners, N.X. Sun, J. McCord, M. Gerken, G. Schmidt, M. Höft, R. Knöchel, F. Faupel, E. Quandt, Wide Band Low Noise Love Wave Magnetic Field Sensor System, *Sci. Rep.* 8 (2018) 278. <https://doi.org/10.1038/s41598-017-18441-4>.
- [14] B. Jakoby, M.J. Vellekoop, Properties of Love waves: applications in sensors, *Smart Materials and Structures* 6 (1997) 668–679.
- [15] M.I. Gaso Rocha, Y. Jimenez, F. A., A. Arnau, Love Wave Biosensors: A Review, in: T. Rinken (Ed.), *State of the Art in Biosensors - General Aspects*, InTech, 2013.
- [16] E.W. Lee, Magnetostriction and Magnetomechanical Effects, *Reports on Progress in Physics* 19 (1955) 184–229. <https://doi.org/10.1088/0034-4885/18/1/305>.
- [17] X. Liu, B. Tong, J. Ou-Yang, X. Yang, S. Chen, Y. Zhang, B. Zhu, Self-biased vector magnetic sensor based on a Love-type surface acoustic wave resonator, *Appl. Phys. Lett.* 113 (2018) 82402. <https://doi.org/10.1063/1.5044478>.

- [18] Y. Yang, P. Mengue, H. Mishra, C. Floer, S. Hage-Ali, S. Petit-Watelot, D. Lacour, M. Hehn, T. Han, O. Elmazria, Wireless Multifunctional Surface Acoustic Wave Sensor for Magnetic Field and Temperature Monitoring, *Adv Materials Technologies* 7 (2022) 2100860. <https://doi.org/10.1002/admt.202100860>.
- [19] J.M. Meyer, V. Schell, J. Su, S. Fichtner, E. Yarar, F. Niekiel, T. Giese, A. Kittmann, L. Thormählen, V. Lebedev, S. Moench, A. Žukauskaitė, E. Quandt, F. Lofink, Thin-Film-Based SAW Magnetic Field Sensors, *Sensors (Basel)* 21 (2021). <https://doi.org/10.3390/s21248166>.
- [20] V. Schell, C. Müller, P. Durdaut, A. Kittmann, L. Thormählen, F. Lofink, D. Meyners, M. Höft, J. McCord, E. Quandt, Magnetic anisotropy controlled FeCoSiB thin films for surface acoustic wave magnetic field sensors, *Appl. Phys. Lett.* 116 (2020) 73503. <https://doi.org/10.1063/1.5140562>.
- [21] J. Labrenz, A. Bahr, P. Durdaut, M. Hoft, A. Kittmann, V. Schell, E. Quandt, Frequency Response of SAW Delay Line Magnetic Field/Current Sensor, *IEEE Sens. Lett.* 3 (2019) 1–4. <https://doi.org/10.1109/LESENS.2019.2943129>.
- [22] M. Yalaz, G. Deuschl, M. Butz, A. Schnitzler, A.-K. Helmers, M. Höft, Investigation of Magnetolectric Sensor Requirements for Deep Brain Stimulation Electrode Localization and Rotational Orientation Detection, *Sensors (Basel)* 21 (2021). <https://doi.org/10.3390/s21072527>.
- [23] P. Durdaut, C. Müller, A. Kittmann, V. Schell, A. Bahr, E. Quandt, R. Knöchel, M. Höft, J. McCord, Phase Noise of SAW Delay Line Magnetic Field Sensors, *Sensors (Basel)* 21 (2021). <https://doi.org/10.3390/s21165631>.
- [24] C. Müller, P. Durdaut, R.B. Holländer, A. Kittmann, V. Schell, D. Meyners, M. Höft, E. Quandt, J. McCord, Imaging of Love Waves and Their Interaction with Magnetic Domain Walls in Magnetolectric Magnetic Field Sensors, *Adv Elect Materials* 8 (2022) 2200033. <https://doi.org/10.1002/aelm.202200033>.
- [25] L. Jiang, E.R. Nowak, P.E. Scott, J. Johnson, J.M. Slaughter, J.J. Sun, R.W. Dave, Low-frequency magnetic and resistance noise in magnetic tunnel junctions, *Phys. Rev. B* 69 (2004) 1660. <https://doi.org/10.1103/PhysRevB.69.054407>.
- [26] H. T. Hardner, M. B. Weissman, M. B. Salamon, and S. S. P. Parkin, Fluctuation-dissipation relation for giant magnetoresistive $1/f$ noise, *Physical Review B* 48 (1993).
- [27] A. Wallash, A study of voltage fluctuation, noise and magnetic instability in spin valve GMR recording heads, *IEEE Trans. Magn.* 34 (1998) 1450–1452. <https://doi.org/10.1109/20.706579>.
- [28] U. Queitsch, J. McCord, A. Neudert, R. Schäfer, L. Schultz, K. Rott, H. Brückl, Domain wall induced modes of high-frequency response in ferromagnetic elements, *Journal of Applied Physics* 100 (2006) 93911. <https://doi.org/10.1063/1.2365382>.
- [29] G. Durin, P. Falferi, M. Cerdonio, G.A. Prodi, S. Vitale, Low temperature properties of soft magnetic materials: Magnetic viscosity and $1/f$ thermal noise, *Journal of Applied Physics* 73 (1993) 5363–5365. <https://doi.org/10.1063/1.353732>.
- [30] W.H. Meiklejohn, C.P. Bean, New Magnetic Anisotropy, *Physical Review* 105 (1957) 904–913.
- [31] J. Nogués, I.K. Schuller, Exchange Bias, *Journal of Magnetism and Magnetic Materials* 192 (1999) 203–232.
- [32] W.C. Cain, M.H. Kryder, Improved bias and stability in dual-exchange-biased unshielded magnetoresistive heads, *IEEE Trans. Magn.* 26 (1990) 2412–2414. <https://doi.org/10.1109/20.104748>.
- [33] J. McCord, A. Hubert, J.C.S. Kools, M.-C. de Nooijer, Magnetization Processes in Exchange Biased Giant Magnetoresistive Multilayer Elements, *IEEE Transactions on Magnetics* 32 (1996).
- [34] S. Cardoso, D.C. Leitao, L. Gameiro, F. Cardoso, R. Ferreira, E. Paz, P.P. Freitas, Magnetic tunnel junction sensors with pTesla sensitivity, *Microsyst Technol* 20 (2014) 793–802. <https://doi.org/10.1007/s00542-013-2035-1>.
- [35] H. van den Berg, W. Clemens, G. Gieres, G. Rupp, W. Schelter, M. Vieth, GMR sensor scheme with artificial antiferromagnetic subsystem, *IEEE Trans. Magn.* 32 (1996) 4624–4626. <https://doi.org/10.1109/20.539099>.
- [36] E. Lage, C. Kirchhof, V. Hrkac, L. Kienle, R. Jahns, R. Knöchel, E. Quandt, D. Meyners, Exchange biasing of magnetolectric composites, *Nat. Mater.* 11 (2012) 523–529. <https://doi.org/10.1038/nmat3306>.

- [37] V. Rößisch, E. Yarar, N.O. Urs, I. Teliban, R. Knöchel, J. McCord, E. Quandt, D. Meyners, Exchange biased magnetoelectric composites for magnetic field sensor application by frequency conversion, *Journal of Applied Physics* 117 (2015) 17B513. <https://doi.org/10.1063/1.4913814>.
- [38] B. Spetzler, C. Bald, P. Durdaut, J. Reermann, C. Kirchhof, A. Teplyuk, D. Meyners, E. Quandt, M. Höft, G. Schmidt, F. Faupel, Exchange biased delta-E effect enables the detection of low frequency pT magnetic fields with simultaneous localization, *Sci. Rep.* 11 (2021) 5269. <https://doi.org/10.1038/s41598-021-84415-2>.
- [39] M. Jovičević Klug, L. Thormählen, V. Rößisch, S.D. Toxværd, M. Höft, R. Knöchel, E. Quandt, D. Meyners, J. McCord, Antiparallel exchange biased multilayers for low magnetic noise magnetic field sensors, *Appl. Phys. Lett.* 114 (2019) 192410. <https://doi.org/10.1063/1.5092942>.
- [40] V. Polewczyk, K. Dumesnil, D. Lacour, M. Moutaouekkil, H. Mjahed, N. Tiercelin, S. Petit Watelot, H. Mishra, Y. Dusch, S. Hage-Ali, O. Elmazria, F. Moutaigne, A. Talbi, O. Bou Matar, M. Hehn, Unipolar and Bipolar High-Magnetic-Field Sensors Based on Surface Acoustic Wave Resonators, *Phys. Rev. Applied* 8 (2017). <https://doi.org/10.1103/PhysRevApplied.8.024001>.
- [41] K.M. Seemann, O. Gomony, Y. Mokrousov, A. Hörner, S. Valencia, P. Klamsner, F. Kronast, A. Erb, A.T. Hindmarch, A. Wixforth, C.H. Marrows, P. Fischer, Magnetoelastic resonance as a probe for exchange springs at antiferromagnet-ferromagnet interfaces, *Phys. Rev. B* 105 (2022). <https://doi.org/10.1103/PhysRevB.105.144432>.
- [42] J. McCord, R. Mattheis, D. Elefant, Dynamic magnetic anisotropy at the onset of exchange bias: The NiFe/IrMn ferromagnet/antiferromagnet system, *Phys. Rev. B* 70 (2004) 4865. <https://doi.org/10.1103/PhysRevB.70.094420>.
- [43] C. Liu, C. Yu, H. Jiang, L. Shen, C. Alexander, G.J. Mankey, Effect of interface roughness on the exchange bias for NiFe/FeMn, *Journal of Applied Physics* 87 (2000) 6644–6646. <https://doi.org/10.1063/1.372797>.
- [44] J. van Driel, F.R. de Boer, K.-M.H. Lenssen, R. Coehoorn, Exchange biasing by Ir19Mn81: Dependence on temperature, microstructure and antiferromagnetic layer thickness, *Journal of Applied Physics* 88 (2000) 975–982. <https://doi.org/10.1063/1.373764>.
- [45] A.J. Devasahayam, P.J. Sides, M.H. Kryder, Magnetic, temperature, and corrosion properties of the NiFe/IrMn exchange couple, *Journal of Applied Physics* 83 (1998) 7216–7218. <https://doi.org/10.1063/1.367550>.
- [46] A. Mazzamurro, Y. Dusch, P. Pernod, O. Bou Matar, A. Addad, A. Talbi, N. Tiercelin, Giant Magnetoelastic Coupling in a Love Acoustic Waveguide Based on TbCo₂ / FeCo Nanostructured Film on ST-Cut Quartz, *Phys. Rev. Applied* 13 (2020). <https://doi.org/10.1103/PhysRevApplied.13.044001>.
- [47] N.O. Urs, I. Teliban, A. Piorra, R. Knöchel, E. Quandt, J. McCord, Origin of hysteretic magnetoelastic behavior in magnetoelectric 2-2 composites, *Appl. Phys. Lett.* 105 (2014) 202406. <https://doi.org/10.1063/1.4901948>.
- [48] T. Roux-Marchand, O. Elmazria, F. Sarry, Infra-red Thermography for spatially resolved measurements of the temperature distribution on the Acoustic Wave Devices, *IEEE International Ultrasonics Symposium (IUS) 21-25 July 2013* (2013). <https://doi.org/10.1109/ULTSYM.2013.0494>.
- [49] C. Chen, S. Fu, L. Han, R. Su, P. Liu, R. Chen, W. Zhu, L. Liao, F. Pan, C. Song, Energy Harvest in Ferromagnet-Embedded Surface Acoustic Wave Devices, *Adv Elect Materials* (2022) 2200593. <https://doi.org/10.1002/aelm.202200593>.
- [50] J. Schmalz, A. Kittmann, P. Durdaut, B. Spetzler, F. Faupel, M. Höft, E. Quandt, M. Gerken, Multi-Mode Love-Wave SAW Magnetic-Field Sensors, *Sensors (Basel)* 20 (2020). <https://doi.org/10.3390/s20123421>.

Chapter 4

Summary and Outlook

This chapter provides an final conclusion of the presented results and gives a summarizing discussion and overall view on this thesis' topics as a whole. Also an outlook is given on how to further improve the performance of SAW magnetic field sensors and how they can be incorporated into biomagnetic sensing applications.

4.1 Summary

In this work highly sensitive and low-noise surface acoustic wave magnetic field sensors have been developed. The fabrication of the sensing devices included a broad variety of microfabrication techniques ranging from magnetron sputtering of the interdigital transducers and the magnetostrictive layer and plasma-enhanced chemical vapor deposition of the guiding layer, to the structuring of each layer by photolithography and different plasma etching techniques. A particular focus of this work was the deposition of magnetostrictive films with the composition $(\text{Fe}_{90}\text{Co}_{10})_{78}\text{Si}_{12}\text{B}_{10}$ on ST-cut quartz substrates and ST-cut quartz-based SAW sensors. Herein, it was demonstrated that the piezoelectric ST-cut quartz substrate has a major influence on the magnetic properties of these films and therefore on the overall sensor performance. Due to the anisotropic thermal expansion of the quartz substrate uniaxial stress is acting on the films, if the samples are subjected to temperature changes. This stress increases the anisotropy energy of the 200 nm thick FeCoSiB layers as it is directly proportional to the temperature change. A common technique to induce magnetic anisotropy into a magnetostrictive film is the annealing and subsequent cooling inside a magnetic field. As the required temperatures for the annealing of FeCoSiB are above 250 °C, the films possess high stress-induced anisotropy energies. Consequently, the large anisotropy fields and the reduced magnetoelastic coupling significantly reduce the sensitivity of the SAW sensors. In fact, even without inducing a magnetic anisotropy deliberately the sensitivity is about 20 times higher. Still, a uniaxial anisotropy is required to achieve large magnetoelastic coupling and as a consequence high sensitivities of the SAW sensors. To this end, a magnetic field is applied during the deposition of the FeCoSiB films, which induces an easy axis of magnetization parallel to the SAW propagation direction. As the temperature increase during sputtering is only 13 °C, the contribution of stress to the total anisotropy energy is small compared to the contribution of the magnetic field. Due to the well aligned but small anisotropy, sensitivities as high as 2000 °/mT were achieved. This high sensitivity enables the detection of small magnetic fields in the pT range. The limit of detection was improved to 70 pT/ $\sqrt{\text{Hz}}$ at 10 Hz and 25 pT/ $\sqrt{\text{Hz}}$ at 100 Hz.

In a collaborative work the performance of SAW sensors with DC magnetron sputtered FeCoSiB compared to RF sputtered FeCoSiB was demonstrated in Section 3.2. While the deposition time for 200 nm of FeCoSiB was reduced from 4.5 h (RF) to 1.5 h (DC), the performance of the sensors was similar in both cases with LODs of about 170 pT/ $\sqrt{\text{Hz}}$ at 10 Hz and 50 pT/ $\sqrt{\text{Hz}}$ at 100 Hz. As a consequence of the new

sputtering configuration an increased hysteresis of the bias curves was introduced in all sensors. This hysteresis reduced the sensitivity of the SAW sensors, but at the same time enabled sensor operation without the requirement of an additional bias field by utilizing that magnetic hysteresis.

Thin film AlScN-based SAW magnetic field sensors, which have been developed and fabricated at Fraunhofer ISIT were evaluated in this work. The AlScN was deposited on silicon substrates and used for SAW excitation. On the c-axis grown films several acoustic modes were excited and amongst these a Rayleigh mode at around 295 MHz was used for magnetic field sensing, as it provided the highest sensitivity to magnetic fields. Therefore, LODs of $2 \text{ nT}/\sqrt{\text{Hz}}$ at 10 Hz and $400 \text{ pT}/\sqrt{\text{Hz}}$ at 100 Hz were achieved. This is a first step towards the integration of SAW sensors into MEMS and CMOS technologies as they can potentially be fabricated on a large scale on silicon wafers.

Magnetic domain walls are the main origin of magnetic noise in many magnetic thin film-based sensors, which is also the case for SAW magnetic field sensors. In order to further improve their limit of detection exchange bias magnetic films were applied to SAW sensors. Magnetic field annealing cannot be applied to set the exchange bias, therefore it is set by a magnetic field applied during the deposition. In this work a top pinning exchange bias stack consisting of Ta (7 nm)/FeCoSiB (100 nm)/NiFe (6 nm)/MnIr (8 nm)/Ta (5 nm) was used, wherein MnIr is the antiferromagnetic material, FeCoSiB the magnetostrictive material and NiFe the magnetic seed layer for MnIr. The NiFe layer enabled the growth of (111) textured MnIr layers, which provide improved exchange bias compared to MnIr layers without a preferred crystallographic orientation. By rotating the sample after the deposition of one stack inside the magnetic field by 180° and depositing the same stack again, an antiparallel exchange bias was realized. The antiparallel alignment created a single domain state throughout the full film even for total FeCoSiB thicknesses of 200 nm. Although the anisotropy field is higher in exchange biased layers as for the additional unidirectional anisotropy, the total phase change between magnetic saturation and zero field is significantly higher with in SAW sensors with antiparallel exchange biased layers. Consequently, the sensitivities of these sensors are similar to non-exchange biased SAW sensors. It was shown that the sensitivity and phase noise of exchange biased sensors are not only dependent on the magnetic bias field but also depend on the excitation power of the SAW sensor. The sensitivity increases significantly only at very high excitation powers (above 20 dBm), while the noise exhibits a different power dependency. The phase noise at a defined

bias field below magnetic saturation decreases until it reaches a minimum and starts to increase again. As the sensitivity does not change over a wide excitation power range, the LOD follows this trend. Therefore, limits of detection at an optimum excitation power of $28 \text{ pT}/\sqrt{\text{Hz}}$ at 10 Hz and $10 \text{ pT}/\sqrt{\text{Hz}}$ at 100 Hz were achieved. This is an improvement by a factor of 2.5 compared to the non-exchange biased SAW sensors presented in Section 3.1 and nearly one order of magnitude better compared to the published results before the start of this thesis.

4.2 Outlook

For biomagnetic sensing limits of detection of about $1 \text{ pT}/\sqrt{\text{Hz}}$ and even below that at frequencies below 100 Hz are required. To achieve such low LODs additional measures need to be taken to further improve the performance of SAW sensors. First of all, all additional sources leading to magnetically generated phase noise need to be identified. While noise originating from domain walls was eliminated, there is still magnetically induced noise at a defined bias field which adds upon the $1/f$ noise of the SAW sensor itself. One potential noise source is the increase in temperature upon SAW excitation, which can cause an increase in phase noise via the temperature itself. Additionally, stress is induced from anisotropic thermal expansion, which potentially rotates the anisotropy in the magnetic film and thereby could increase magnetic losses. Further, the interaction of magnetization fluctuations in single domain magnetic layers and the dynamic strain from acoustic waves is not understood, yet. Therefore, time-resolved magneto-optical imaging can potentially reveal these mechanisms. The temperature contribution might be suppressed by moderate active thermoelectric cooling, to keep the SAW sensor at or slightly below room temperature. However, the ratio of these different potential contributions conditions further investigations.

In the context of exchange bias the operation of the SAW sensors without an external bias magnetic field should be pursued. In cantilever-style magnetoelectric composites the operation point, i.e. the point of highest piezomagnetic coefficient, could be shifted to zero fields by tilting the exchange bias direction with respect to the cantilever dimensions [LKH⁺12]. Whether this is also applicable to SAW sensors needs to be investigated. If tilting the exchange bias direction is also applicable to SAW sensors the optimum angle needs to be determined. External bias field free operation is desired for biomedical applications as it reduces the required space needed for the sensor system, which allows for better integration. Additionally, the omission of an external magnetic field makes the operation of the sensors more convenient for end users.

A concept applied successfully to GMR and TMR sensors is magnetic flux concentration [GAC⁺07, AF09], which has never been applied to SAW magnetic field sensors so far. This approach is promising for sensors with small magnetic film dimension. Adding larger and thicker high-permeability films or ribbons along the sensing axis of the sensor increases the magnetic flux density inside the film. Via the increase in flux density, the sensitivity of the sensors increases. In a first attempt two VITROVAC 6025X ribbons from *Vacuumschmelze* were placed along the hard axis of magnetiza-

tion of an exchange biased SAW sensors as shown in Figure 4.1a. In Figure 4.1b it is demonstrated that with this simple approach the sensitivity could be increased by a factor of 4, which leads to an improvement of LOD by a factor of two with $13 \text{ pT}/\sqrt{\text{Hz}}$ at 10 Hz. Further investigations are necessary regarding the dimensions and shape of the flux concentrators, their contribution to magnetic noise, their permeability at higher frequencies, the optimal material and the distance to the magnetic film. The incorporation of thin film flux concentrators into the microfabrication process is also possible.

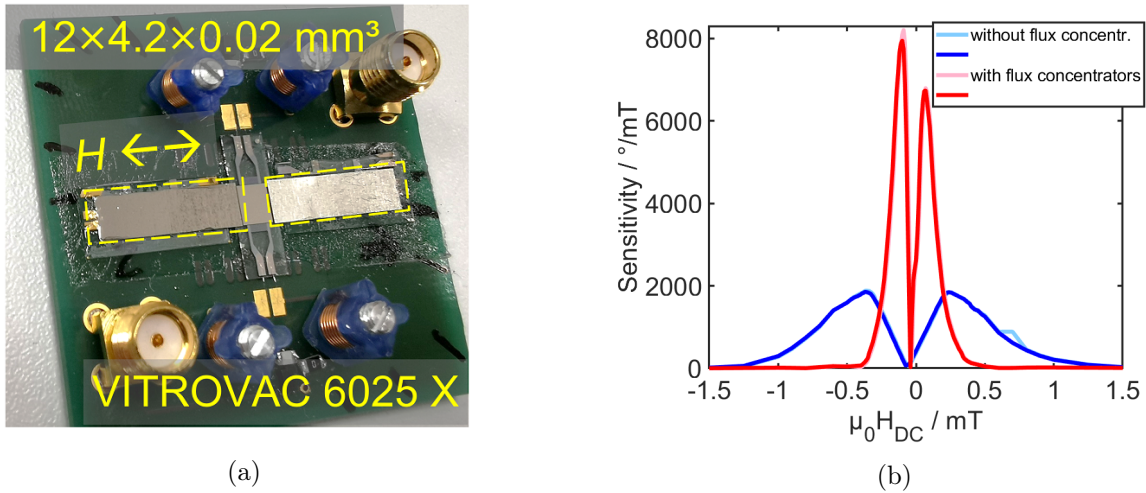
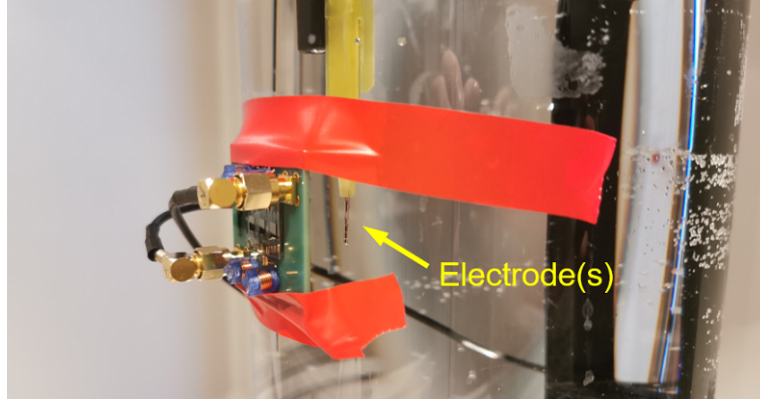


Figure 4.1: First flux concentrator approach on SAW magnetic field sensors. (a) Photograph of magnetic flux concentrators made of VITROVAC 6025 X along the hard axis, which are placed on the right and left hand side of the magnetic film. The flux concentrator ribbons have dimensions of $12 \times 4.2 \text{ mm}^2$ and a thickness of $20 \mu\text{m}$. (b) Resulting sensitivities with and without flux concentration. In both cases the bias field was changed from -10 mT to $+10 \text{ mT}$ (bright) and vice versa (dark).

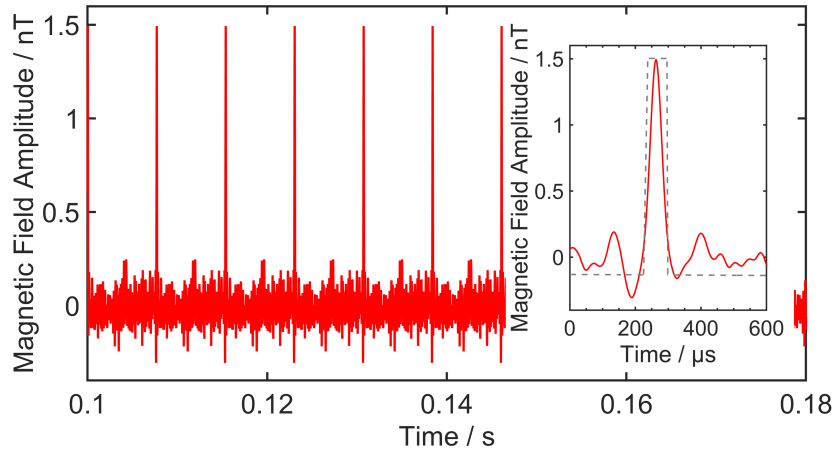
The reduction of the detection limit throughout this work, makes SAW magnetic field sensors a candidate for biomagnetic applications. With the help of converse magneto-electric composites magnetocardiograms of human patients have been recorded after 60 averages [Hay20]. Since the detection limits of these are similar to SAW sensors magnetocardiography with SAW sensors is in reach as well.

In preliminary experiments the stimulation pulses of a deep brain stimulation electrode were measured within a phantom cylinder. Figure 4.2a shows the setup, in which the sensor was fixed onto the saline solution filled phantom cylinder and stimulation pulses were applied in the so-called bipolar configuration. During bipolar stimulation the currents run between specific segments of the electrode rings of the stimulator. Figure 4.2b shows the measured stimulation pulses in the time domain. It is noted, that no external bias field could be applied during these measurements. As a result, the

sensitivity was not as high as it could be potentially. In addition, a lock-in amplifier was used for read-out of the SAW sensor, that exhibited a higher phase noise level than the SAW sensor. Therefore, to utilize the full potential of the SAW sensors bias



(a)



(b)

Figure 4.2: Preliminary measurement of the magnetic fields of deep brain stimulation electrode pulses. (a) Position of the SAW sensor with respect to the DBS electrode inside a phantom filled with a saline solution. The sensor-to-electrode distance was 4 cm. (b) Magnetic DBS pulses from bipolar excitation recorded over time. The inset shows one of the pulses and the original pulse signal, which is drawn schematically (dashed line). The stimulation amplitude was 12.7 mA, the pulse frequency 130 Hz, the pulse width 60 μ s and the signals were averaged 60 times. In cooperation with Mevlüt Yalaz.

free operation should be improved and specifically designed low-noise electronics are required. The final goal of the DBS measurements is the localization of the deep brain stimulation electrode within the human brain. To this end, an entire array of SAW sensors and the corresponding read-out electronics are necessary to be able to perform simultaneous measurements in a time frame which is reasonable for patients.

Full List of Publications

- **Schell, V.**; Spetzler, E.; Wolff, N.; Bumke, L.; Kienle, L.; McCord, J.; Quandt, E.; Meyners, D., Exchange Biased Surface Acoustic Wave Magnetic Field Sensors, *submitted* (2022).
- Wang, H.; Arbustini, J.; Elzenheimer, E.; **Schell, V.**; Höft, M.; Quandt, E.; Schmidt, G.; Heidari, H.; Bahr, A., Study of Chopping Magnetic Flux Modulation on Surface Acoustic Wave Magnetic Sensor, *IEEE Xplore*, *accepted for publication* (2022).
- Wolframm, H.; **Schell, V.**; Quandt, E.; Höft, M.; Bahr, A., High sensitivity magnetoelastic surface acoustic wave (SAW) magnetic field sensors, *Proc. SPIE* 12205, Spintronics XV, 1220505 (2022).
- Müller, C.; Durdaut, P.; Holländer, R.B.; Kittmann, A.; **Schell, V.**; Meyners, D.; Höft, M.; Quandt, E.; McCord, J., Imaging of Love waves and their interaction with magnetic domain walls in magnetoelectric magnetic field sensors, *Advanced Electronic Materials*, 2200033 (2022).
- Thormählen, L.; Seidler, D.; **Schell, V.**; Munnik, F.; McCord, J.; Meyners, D., Sputter Deposited Magnetostrictive Layers for SAW Magnetic Field Sensors, *Sensors* 21, 8386 (2021).
- Meyer, J. M.; **Schell, V.**; Su, J.; Fichtner, S.; Yarar, E.; Niekil, F.; Giese, T.; Kittmann, A.; Thormählen, L.; Lebedev, V.; Mönch, S.; Žukauskaitė, A.; Quandt, E.; Lofink, F., Thin-film-Based SAW Magnetic Field Sensors, *Sensors* 21, 8166 (2021).
- Durdaut, P.; Müller, C.; Kittmann, A.; **Schell, V.**; Bahr, A.; Quandt, E.; Knöchel, R.; Höft, M.; McCord, J., Phase Noise of SAW Delay Line Magnetic Field Sensors, *Sensors* 21, 16 (2021).

- Liang, X.; Matyushov, A.; Hayes P.; **Schell, V.**; Dong, C.; Chen, H.; He, Y.; Will-Cole, A.; Quandt, E.; Martins, P.; McCord, J.; Medarde, M.; Lanceros-Méndez, S.; van Dijken, S.; Sun, N.; Sort, J., Roadmap on Magnetoelectric Materials and Devices, *IEEE Transactions on Magnetics* 57, 8 (2021).
- Bas, D. A.; Shah, P. J.; Matyushov, A.; Popov, M.; **Schell, V.**, Budhani, R. C.; Srinivasan, G.; Quandt, E.; Sun, N.; Page, M. R., Acoustically Driven Ferromagnetic Resonance in Diverse Ferromagnetic Thin Films, *IEEE Transactions on Magnetics* 57, 2 (2020).
- Kittmann, A.; Müller, C.; Durdaut, P.; Thormählen, L.; **Schell, V.**; Niekief, F.; Lofink, F.; Meyners, D.; Knöchel, R.; Höft, M.; McCord, J.; Quandt, E., Sensitivity and Noise Analysis of SAW Magnetic Field Sensors with varied Magnetostrictive Layer Thicknesses, *Sensors and Actuators: A. Physical* 311, 111998 (2020).
- **Schell, V.**; Müller, C.; Durdaut, P.; Kittmann, A.; Thormählen, L.; Lofink, F.; Meyners, D.; Höft, M.; McCord, J.; Quandt, E., Magnetic anisotropy controlled FeCoSiB thin films for surface acoustic wave magnetic field sensors, *Applied Physics Letters* 116, 073503 (2020).
- Hayes, P.; Jovičević Klug, M.; Toxværd, S.; Durdaut, P.; **Schell, V.**; Teplyuk, A.; Burdin, D.; Winkler, A.; Weser, R.; Fetisov, Y.; Höft, M.; Knöchel, R.; McCord, J.; Quandt, E., Converse Magnetoelectric Composite Resonator for Sensing Small Magnetic Fields, *Scientific Reports* 9(1), 16355 (2019).
- Labrenz, J.; Bahr, A.; Durdaut, P.; Hoft, M.; Kittmann, A.; **Schell, V.**; Quandt, E., Frequency Response of SAW Delay Line Magnetic Field/Current Sensor. *IEEE Sensors Letters*, 1–1 (2019).
- Hayes, P.; **Schell, V.**; Salzer, S.; Burdin, D.; Yarar, E.; Piorra, A.; Knöchel, R.; Fetisov, Y. K.; Quandt, E., Electrically modulated magnetoelectric AlN/FeCoSiB film composites for DC magnetic field sensing, *Journal of Physics D: Applied Physics* 51(35), 354002 (2018).

Conference Presentations

- V. Schell, E. Golubeva, C. Müller, L. Bumke, L. Thormählen, A. Bahr, J. McCord, D. Meyners and E. Quandt, Exchange Biasing of Surface Acoustic Wave Magnetic Field Sensors in International Intelligent Materials 2022, Kiel, Germany, June 29th – July 1st, 2022.

- V. Schell, E. Golubeva, L. Thormählen, A. Kittmann, J. McCord, D. Meyners and E. Quandt, Exchange Biased Multilayers for SAW Magnetic Field Sensors in 2021 MRS Fall Meeting & Exhibit, Boston, USA, November 29th - December 2nd, 2021.
- V. Schell, P. Durdaut, C. Müller, A. Kittmann, M. Yalaz, A. Bahr, D. Meyners, M. Höft, J. McCord and E. Quandt, Sensing Small Magnetic Fields with Surface Acoustic Waves in SAW Symposium 2021, Dresden, Germany, October 14th - 15th, 2021.
- V. Schell, C. Müller, P. Durdaut, M. Yalaz, A. Kittmann, M. Höft, J. McCord and E. Quandt, Love Wave Magnetic Field Sensors - Fabrication, Characterization, Application in 2019 MRS Fall Meeting & Exhibit, Boston, USA, December 1st - 6th, 2019.
- V. Schell, P. Durdaut, C. Müller, A. Kittmann, J. McCord, M. Höft and E. Quandt, Substrate Materials for High Sensitivity SAW Magnetic Field Sensors in 4th Euro Intelligent Materials 2019, Kiel, Germany, June 17th - 19th, 2019.

Bibliography

- [AF09] JM Almeida and PP Freitas. Field detection in mgo magnetic tunnel junctions with superparamagnetic free layer and magnetic flux concentrators. *Journal of Applied Physics*, 105(7):07E722, 2009.
- [AL12] Majd AlGhatrif and Joseph Lindsay. A brief review: History to understand fundamentals of electrocardiography. *Journal of Community Hospital Internal Medicine Perspectives*, 2(1), 2012.
- [AM19] Seppo P. Ahlfors and Maria Mody. Overview of MEG. *Organizational research methods*, 22(1):95–115, 2019.
- [BBK⁺16] Elena Boto, Richard Bowtell, Peter Krüger, T. Mark Fromhold, Peter G. Morris, Sofie S. Meyer, Gareth R. Barnes, and Matthew J. Brookes. On the potential of a new generation of magnetometers for MEG: A beamformer simulation study. *PloS one*, 11(8):e0157655, 2016.
- [BCM⁺07] Tobias Breidthardt, Michael Christ, Miriam Matti, Delia Schrafl, Kirsten Laule, Markus Noveanu, Tujana Boldanova, Theresia Klima, Willibald Hochholzer, André P. Perruchoud, and Christian Mueller. QRS and QTc interval prolongation in the prediction of long-term mortality of patients with acute destabilised heart failure. *Heart*, 93(9):1093–1097, 2007.
- [Ber98] Giorgio Bertotti. *Hysteresis in magnetism: For physicists, materials scientists, and engineers / Giorgio Bertotti*. Electromagnetism. Academic Press, San Diego, Calif. and London, 1998.
- [BHL⁺18] Elena Boto, Niall Holmes, James Leggett, Gillian Roberts, Vishal Shah, Sofie S. Meyer, Leonardo Duque Muñoz, Karen J. Mullinger, Tim M. Tierney, Sven Bestmann, Gareth R. Barnes, Richard Bowtell, and Matthew J.

- Brookes. Moving magnetoencephalography towards real-world applications with a wearable system. *Nature*, 555(7698):657–661, 2018.
- [BM63] Gerhard Baule and Richard McFee. Detection of the magnetic field of the heart. *American Heart Journal*, 66(1):95–96, 1963.
- [Bot82] Virgil E. Bottom. *Introduction to quartz crystal unit design*. Van Nostrand Reinhold electrical-computer science and engineering series. Van Nostrand Reinhold, New York and London, 1982.
- [BT99] AE Berkowitz and Kentaro Takano. Exchange anisotropy—a review. *Journal of Magnetism and Magnetic materials*, 200(1-3):552–570, 1999.
- [Cam89] Colin Campbell. *Surface acoustic wave devices and their signal processing applications*. Academic Press, Boston, 1989.
- [CG09] B. D. Cullity and C. D. Graham. *Introduction to magnetic materials*. Wiley, Hoboken, N.J. and Chichester, 2nd ed. edition, 2009.
- [Coe10] J. M. D. Coey. *Magnetism and magnetic materials*. Cambridge University Press, Cambridge, 2010.
- [Coh67] David Cohen. Magnetic fields around the torso: Production by electrical activity of the human heart. *Science*, 156(3775):652–654, 1967.
- [Coh75a] David Cohen. Magnetic fields of the human body. *Physics Today*, 28(8):34–43, 1975.
- [Coh75b] David Cohen. Measurements of the magnetic fields produced by the human heart, brain, and lungs. *IEEE Transactions on Magnetics*, 11(2):694–700, 1975.
- [DJB21] Michal Dressler, Michal Janosek, and Mattia Butta. Reduction of magnetic noise limits of orthogonal fluxgate sensor. *AIP Advances*, 11(1):015347, 2021.
- [DKR⁺19] Phillip Durdaut, Anne Kittmann, Enrico Rubiola, Jean-Michel Friedt, Eckhard Quandt, Reinhard Knochel, and Michael Hoft. Noise analysis and comparison of phase- and frequency-detecting readout systems: Application to saw delay line magnetic field sensor. *IEEE Sensors Journal*, 19(18):8000–8008, 2019.

- [DMK⁺21] Phillip Durdaut, Cai Müller, Anne Kittmann, Viktor Schell, Andreas Bahr, Eckhard Quandt, Reinhard Knöchel, Michael Höft, and Jeffrey McCord. Phase noise of SAW delay line magnetic field sensors. *Sensors (Basel, Switzerland)*, 21(16), 2021.
- [DSBK⁺06] Günther Deuschl, Carmen Schade-Brittinger, Paul Krack, Jens Volkmann, Helmut Schäfer, Kai Bötzel, Christine Daniels, Angela Deutschländer, Ulrich Dillmann, Wilhelm Eisner, Doreen Gruber, Wolfgang Hamel, Jan Herzog, Rüdiger Hilker, Stephan Klebe, Manja Kloss, Jan Koy, Martin Krause, Andreas Kupsch, Delia Lorenz, Stefan Lorenzl, H. Maximilian Mehdorn, Jean Richard Moringlane, Wolfgang Oertel, Marcus O. Pinsker, Heinz Reichmann, Alexander Reuss, Gerd-Helge Schneider, Alfons Schnitzler, Ulrich Steude, Volker Sturm, Lars Timmermann, Volker Tronnier, Thomas Trottenberg, Lars Wojtecki, Elisabeth Wolf, Werner Poewe, and Jürgen Voges. A randomized trial of deep-brain stimulation for parkinson’s disease. *The New England journal of medicine*, 355(9):896–908, 2006.
- [Dur19] Phillip Durdaut. *Ausleseverfahren und Rauschmodellierung für magnetoelektrische und magnetoelastische Sensorsysteme*. PhD thesis, Kiel University, Kiel, 2019.
- [EEPW⁺16] Meriem Elhosni, Omar Elmazria, Sébastien Petit-Watelot, Laurent Bouvot, Sergei Zhgoon, Abdelkrim Talbi, Michel Hehn, Keltouma Ait Aissa, Sami Hage-Ali, Daniel Lacour, Frederic Sarry, and Olivier Boumatar. Magnetic field SAW sensors based on magnetostrictive-piezoelectric layered structures: FEM modeling and experimental validation. *Sensors and Actuators A: Physical*, 240:41–49, 2016.
- [ETA18] Jonathan R. Ellenbogen, Ruth Tuura, and Keyoumars Ashkan. Localisation of DBS electrodes post-implantation, to CT or MRI? which is the best option? *Stereotactic and functional neurosurgery*, 96(5):347–348, 2018.
- [Fag06] R. L. Fagaly. Superconducting quantum interference device instruments and applications. *Review of Scientific Instruments*, 77(10):101101, 2006.
- [FC99] T Feng and JR Childress. Fabrication of exchange-biased spin valves with cofeb amorphous layers. *Journal of applied physics*, 85(8):4937–4939, 1999.

- [FFCC07] P. P. Freitas, R. Ferreira, S. Cardoso, and F. Cardoso. Magnetoresistive sensors. *Journal of Physics: Condensed Matter*, 19(16):165221, 2007.
- [Fie05] Manfred Fiebig. Revival of the magnetoelectric effect. *Journal of Physics D: Applied Physics*, 38(8):R123–R152, 2005.
- [FMM95] Gerhard Fischerauer, A. Mauder, and R. Müller. Acoustic wave devices. In H. Meixner, R. Jones, Hans Meixner, and Robert Jones, editors, *Sensors*, pages 135–180. VCH, Weinheim and Cambridge, 1995.
- [FOK⁺18] Kosuke Fujiwara, Mikihiro Oogane, Akitake Kanno, Masahiro Imada, Junichi Jono, Takashi Terauchi, Tetsuo Okuno, Yuuji Aritomi, Masahiro Morikawa, Masaaki Tsuchida, Nobukazu Nakasato, and Yasuo Ando. Magnetocardiography and magnetoencephalography measurements at room temperature using tunnel magneto-resistance sensors. *Applied Physics Express*, 11(2):023001, 2018.
- [FVWD78] D. W. Forester, C. Vittoria, D. C. Webb, and K. L. Davis. Variable delay lines using magnetostrictive metallic–glass film overlays. *Journal of Applied Physics*, 49(3):1794–1796, 1978.
- [Fye94] W. Bruce Fye. A history of the origin, evolution, and impact of electrocardiography. *The American Journal of Cardiology*, 73(13):937–949, 1994.
- [GAC⁺07] A Guedes, JM Almeida, S Cardoso, R Ferreira, and PP Freitas. Improving magnetic field detection limits of spin valve sensors using magnetic flux guide concentrators. *IEEE transactions on magnetics*, 43(6):2376–2378, 2007.
- [GDW⁺75] A. K. Ganguly, K. L. Davis, D. C. Webb, C. Vittoria, and D. W. Forester. Magnetically tuned surface-acoustic-wave phase shifter. *Electronics Letters*, 11(25/26):610–611, 1975.
- [GKK⁺14] Onno Gabriel, Simon Kirner, Michael Klick, Bernd Stannowski, and Rutger Schlatmann. Plasma monitoring and PECVD process control in thin film silicon-based solar cell manufacturing. *EPJ Photovoltaics*, 5:55202, 2014.
- [Han87] S. M. Hanna. Magnetic field sensors based on SAW propagation in magnetic films. *IEEE transactions on ultrasonics, ferroelectrics, and frequency control*, 34(2):191–194, 1987.

- [Has00] Ken-ya Hashimoto. *Surface Acoustic Wave Devices in Telecommunications: Modelling and Simulation*. Springer Berlin Heidelberg, Berlin, Heidelberg, 2000.
- [Hay20] Patrick Hayes. *Converse Magnetolectric Resonators for Biomagnetic Field Sensing*. PhD thesis, Kiel University, Kiel, 2020.
- [HD97] Geoffrey L Harding and Jia Du. Design and properties of quartz-based love wave acoustic sensors incorporating silicon dioxide and PMMA guiding layers. *Smart materials and structures*, 6(6):716, 1997.
- [HJT⁺19] P. Hayes, M. Jovičević Klug, S. Toxværd, P. Durdaut, V. Schell, A. Teplyuk, D. Burdin, A. Winkler, R. Weser, Y. Fetisov, M. Höft, R. Knöchel, J. McCord, and E. Quandt. Converse magnetolectric composite resonator for sensing small magnetic fields. *Scientific reports*, 9(1):16355, 2019.
- [HMW⁺94] Chun Hu, Scott T. Martin, Eugene Worley, Joe White, Ray Kjar, and Guann-pyng Li. Effects of plasma-etching-induced gate oxide degradation on MOSFET's 1/f noise. In Barbara Vasquez and Hisao Kawasaki, editors, *Microelectronics Manufacturability, Yield, and Reliability*, SPIE Proceedings, pages 128–136. SPIE, 1994.
- [Höl12] Iris Hölken. *Si-rich oxide by plasma enhanced chemical vapor deposition*. Master's thesis, Kiel University, Kiel, 2012.
- [JBD⁺20] Michal Janosek, Mattia Butta, Michal Dressler, Elda Saunderson, David Novotny, and Coenrad Fourie. 1-pT noise fluxgate magnetometer for geomagnetic measurements and unshielded magnetocardiography. *IEEE Transactions on Instrumentation and Measurement*, 69(5):2552–2560, 2020.
- [JTR⁺19] M. Jovičević Klug, L. Thormählen, V. Röbisch, S. D. Toxværd, M. Höft, R. Knöchel, E. Quandt, D. Meyners, and J. McCord. Antiparallel exchange biased multilayers for low magnetic noise magnetic field sensors. *Applied Physics Letters*, 114(19):192410, 2019.
- [JV97] Bernhard Jakoby and Michael J. Vellekoop. Properties of love waves: applications in sensors. *Smart Materials and Structures*, 6:668–679, 1997.

- [KB05] Amir Kashani and S. Serge Barold. Significance of QRS complex duration in patients with heart failure. *Journal of the American College of Cardiology*, 46(12):2183–2192, 2005.
- [KDZ⁺18] Anne Kittmann, Phillip Durdaut, Sebastian Zabel, Jens Reermann, Julius Schmalz, Benjamin Spetzler, Dirk Meyners, Nian X. Sun, Jeffrey McCord, Martina Gerken, Gerhard Schmidt, Michael Höft, Reinhard Knöchel, Franz Faupel, and Eckhard Quandt. Wide band low noise Love wave magnetic field sensor system. *Scientific reports*, 8(1):278, 2018.
- [KII⁺11] Michio Kadota, Shigeo Ito, Yoshihiro Ito, Takuo Hada, and Kenjiro Okaguchi. Magnetic sensor based on surface acoustic wave resonators. *Japanese Journal of Applied Physics*, 50(7):07HD07, 2011.
- [Kin87] Gordon S Kino. *Acoustic waves: devices, imaging, and analog signal processing*, volume 107. Prentice-hall Englewood Cliffs, NJ, 1987.
- [Kit20] Anne Kittmann. *Love-mode Surface Acoustic Wave Sensors for Magnetic Field Sensing*. PhD thesis, Kiel University, Kiel, 2020.
- [KK07] Drew S. Kern and Rajeev Kumar. Deep brain stimulation. *The neurologist*, 13(5):237–252, 2007.
- [KKAR03] I. K. Kominis, T. W. Kornack, J. C. Allred, and M. V. Romalis. A subfemtotesla multichannel atomic magnetometer. *Nature*, 422(6932):596–599, 2003.
- [KLPY13] Joey S. W. Kwong, Boris Leithäuser, Jai-Wun Park, and Cheuk-Man Yu. Diagnostic value of magnetocardiography in coronary artery disease and cardiac arrhythmias: a review of clinical data. *International journal of cardiology*, 167(5):1835–1842, 2013.
- [KMBJ19] Jan G. Korvink, Neil MacKinnon, Vlad Badilita, and Mazin Jouda. "small is beautiful" in NMR. *Journal of magnetic resonance (San Diego, Calif. : 1997)*, 306:112–117, 2019.
- [KMD⁺20] Anne Kittmann, Cai Müller, Phillip Durdaut, Lars Thormählen, Viktor Schell, Florian Niekiel, Fabian Lofink, Dirk Meyners, Reinhard Knöchel, Michael Höft, Jeffrey McCord, and Eckhard Quandt. Sensitivity and noise analysis of saw magnetic field sensors with varied magnetostrictive layer thicknesses. *Sensors and Actuators A: Physical*, 311(1):111998, 2020.

- [KS15] Hikaru Karo and Ichiro Sasada. Magnetocardiogram measured by fundamental mode orthogonal fluxgate array. *Journal of Applied Physics*, 117(17):17B322, 2015.
- [KST19] Svenja Knappe, Tilmann Sander, and Lutz Trahms. Optically pumped magnetometers for MEG. In Selma Supek and Cheryl J. Aine, editors, *Magnetoencephalography*, Springer Reference, pages 1301–1312. Springer Nature, Cham, 2019.
- [KVH⁺94] Günter Kovacs, MJ Vellekoop, R Haueis, GW Lubking, and A Venema. A love wave sensor for (bio) chemical sensing in liquids. *Sensors and Actuators A: Physical*, 43(1-3):38–43, 1994.
- [LBD⁺19] Johannes Labrenz, Andreas Bahr, Phillip Durdaut, Michael Höft, Anne Kittmann, Viktor Schell, and Eckhardt Quandt. Frequency response of saw delay line magnetic field/current sensor. *IEEE Sensors Letters*, 3(10):1–4, 2019.
- [LFK⁺20] M. E. Limes, E. L. Foley, T. W. Kornack, S. Caliga, S. McBride, A. Braun, W. Lee, V. G. Lucivero, and M. V. Romalis. Portable magnetometry for detection of biomagnetism in ambient environments. *Physical Review Applied*, 14(1), 2020.
- [Liv82] James D Livingston. Magnetomechanical properties of amorphous metals. *physica status solidi (a)*, 70(2):591–596, 1982.
- [LKH⁺12] Enno Lage, Christine Kirchhof, Viktor Hrkac, Lorenz Kienle, Robert Jahns, Reinhard Knöchel, Eckhard Quandt, and Dirk Meyners. Exchange biasing of magnetoelectric composites. *Nature materials*, 11(6):523–529, 2012.
- [LKP07] Yong Gyu Lim, Ko Keun Kim, and Kwang Suk Park. Ecg recording on a bed during sleep without direct skin-contact. *IEEE Transactions on Biomedical Engineering*, 54(4):718–725, 2007.
- [LQ00] Alfred Ludwig and Eckhard Quandt. Giant magnetostrictive thin films for applications in microelectromechanical systems. *Journal of Applied Physics*, 87(9):4691–4695, 2000.
- [LTOY⁺18] Xiangli Liu, Bei Tong, Jun Ou-Yang, Xiaofei Yang, Shi Chen, Yue Zhang, and Benpeng Zhu. Self-biased vector magnetic sensor based on a love-type

- surface acoustic wave resonator. *Applied Physics Letters*, 113(8):082402, 2018.
- [LYJ⁺00] Congxiao Liu, Chengtao Yu, Huaming Jiang, Liyong Shen, C Alexander, and GJ Mankey. Effect of interface roughness on the exchange bias for nife/femn. *Journal of Applied Physics*, 87(9):6644–6646, 2000.
- [LYK15] Bodong Li, Omar Yassine, and Jurgen Kosel. A surface acoustic wave passive and wireless sensor for magnetic fields, temperature, and humidity. *IEEE Sensors Journal*, 15(1):453–462, 2015.
- [Mat42] Carlo Matteucci. Sur un phenomene physiologique produit par les muscles en contraction. *Ann Chim Phys.*, 6:339–341, 1842.
- [MB56] William H Meiklejohn and Charles P Bean. New magnetic anisotropy. *Physical review*, 102(5):1413, 1956.
- [MCF⁺17] S. Morales, M. C. Corsi, W. Fourcault, F. Bertrand, G. Cauffet, C. Gobbo, F. Alcouffe, F. Lenouvel, M. Le Prado, F. Berger, G. Vanzetto, and E. Labyt. Magnetocardiography measurements with 4He vector optically pumped magnetometers at room temperature. *Physics in medicine and biology*, 62(18):7267–7279, 2017.
- [MDH⁺22] Cai Müller, Phillip Durdaut, Rasmus B. Holländer, Anne Kittmann, Viktor Schell, Dirk Meyners, Michael Höft, Eckhard Quandt, and Jeffrey McCord. Imaging of love waves and their interaction with magnetic domain walls in magnetoelectric magnetic field sensors. *Advanced Electronic Materials*, 8(6):2200033, 2022.
- [MDP⁺20] Aurélien Mazzamurro, Yannick Dusch, Philippe Pernod, Olivier Bou Matar, Ahmed Addad, Abdelkrim Talbi, and Nicolas Tiercelin. Giant magnetoelastic coupling in a love acoustic waveguide based on tbco2 / feco nanostructured film on st-cut quartz. *Physical Review Applied*, 13(4), 2020.
- [MML⁺20] Dmitry Murzin, Desmond J Mapps, Kateryna Levada, Victor Belyaev, Alexander Omelyanchik, Larissa Panina, and Valeria Rodionova. Ultrasensitive magnetic field sensors for biomedical applications. *Sensors*, 20(6):1569, 2020.

- [Mor07] David P. Morgan. *Surface acoustic wave filters: With applications to electronic communications and signal processing*. Academic Press, Amsterdam and London, 2nd ed. edition, 2007.
- [MP75] T. McGuire and R. Potter. Anisotropic magnetoresistance in ferromagnetic 3d alloys. *IEEE Transactions on Magnetism*, 11(4):1018–1038, 1975.
- [MSH⁺20] Harshad Mishra, Jérémy Streque, Michel Hehn, Prince Mengue, Hamid M’Jahed, Daniel Lacour, Karine Dumesnil, Sébastien Petit-Watelot, Sergei Zhgoon, Vincent Polewczyk, Aurélien Mazzamurro, Abdelkrim Talbi, Sami Hage-Ali, and Omar Elmazria. Temperature compensated magnetic field sensor based on love waves. *Smart Materials and Structures*, 29(4):045036, 2020.
- [Mv69] H. Matthews and H. van de Vaart. Magnetoelastic love waves. *Applied Physics Letters*, 15(11):373–375, 1969.
- [ND02] M. Nalbach and O. Dössel. Comparison of sensor arrangements of MCG and ECG with respect to information content. *Physica C: Superconductivity*, 372-376:254–258, 2002.
- [Nob22] NobelPrize.org. The nobel prize in physics 2007. nobel prize outreach AB 2022. <https://www.nobelprize.org/prizes/physics/2007/summary/>, 2022. Accessed: 02.09.2022.
- [NS99] Josep Nogués and Ivan K Schuller. Exchange bias. *Journal of Magnetism and Magnetic Materials*, 192(2):203–232, 1999.
- [OFK⁺21] Mikihiro Oogane, Kosuke Fujiwara, Akitake Kanno, Takafumi Nakano, Hiroshi Wagatsuma, Tadashi Arimoto, Shigemi Mizukami, Seiji Kumagai, Hitoshi Matsuzaki, Nobukazu Nakasato, and Yasuo Ando. Sub-pt magnetic field detection by tunnel magneto-resistive sensors. *Applied Physics Express*, 14(12):123002, 2021.
- [PDL⁺17] V. Polewczyk, K. Dumesnil, D. Lacour, M. Moutaouekkil, H. Mjahed, N. Tiercelin, S. Petit Watelot, H. Mishra, Y. Dusch, S. Hage-Ali, O. Elmazria, F. Moutaigne, A. Talbi, O. Bou Matar, and M. Hehn. Unipolar and bipolar high-magnetic-field sensors based on surface acoustic wave resonators. *Physical Review Applied*, 8(2), 2017.
- [Pri98] Gary Prinz. Magnetolectronics. *Science (New York, N.Y.)*, 282(5394):1660–1663, 1998.

- [QuS22a] QuSpin. Information on QTFM. <https://quspin.com/qtfm/>, 2022. Accessed: 06.09.2022.
- [QuS22b] QuSpin. Information on QZFM Gen-3. <https://quspin.com/products-qzfm/>, 2022. Accessed: 31.08.2022.
- [Ray85] Lord Rayleigh. On waves propagated along the plane surface of an elastic solid. *Proceedings of the London Mathematical Society*, s1-17(1):4–11, 1885.
- [RD99] Daniel Royer and Eugene Dieulesaint. *Elastic waves in solids I: Free and guided propagation*. Springer Science & Business Media, 1999.
- [Rip03] Pavel Ripka. Advances in fluxgate sensors. *Sensors and Actuators A: Physical*, 106(1-3):8–14, 2003.
- [RJAA13] Maria Isabel Rocha Gaso, Yolanda Jimenez, Francis A., and Antonio Arnau. Love wave biosensors: A review. In Toonika Rinken, editor, *State of the Art in Biosensors - General Aspects*. InTech, 2013.
- [Rub09] Enrico Rubiola. *Phase noise and frequency stability in oscillators*. The Cambridge RF and microwave engineering series. Cambridge University Press, Cambridge, 2009.
- [RYU⁺15] V. Röbisch, E. Yarar, N. O. Urs, I. Teliban, R. Knöchel, J. McCord, E. Quandt, and D. Meyners. Exchange biased magnetoelectric composites for magnetic field sensor application by frequency conversion. *Journal of Applied Physics*, 117(17):17B513, 2015.
- [SAA95] Patrick T Squire, Derek Atkinson, and S Atalay. Magnetostrictive and magnetoelastic properties of rapidly quenched wire. *IEEE transactions on magnetics*, 31(2):1239–1248, 1995.
- [SB06] Karsten Sternickel and Alex I. Braginski. Biomagnetism using SQUIDs: status and perspectives. *Superconductor Science and Technology*, 19(3):S160–S171, 2006.
- [Sch03] Marc Dominic Schlenzog. *Entwicklung und Charakterisierung eines Love-Wellen Biosensors*. PhD thesis, Universität Karlsruhe, Karlsruhe, 2003.
- [SF05] Nicola A Spaldin and Manfred Fiebig. The renaissance of magnetoelectric multiferroics. *Science*, 309(5733):391–392, 2005.

- [SGT⁺04] Marc D. Schlensog, Thomas M.A. Gronewold, Michael Tewes, Michael Famulok, and Eckhard Quandt. A Love-wave biosensor using nucleic acids as ligands. *Sensors and Actuators B: Chemical*, 101(3):308–315, 2004.
- [SHHK19] J-H Storm, P. Hömmen, N. Höfner, and R. Körber. Detection of body noise with an ultra-sensitive SQUID system. *Measurement Science and Technology*, 30(12):125103, 2019.
- [SHS⁺19] Yasuhiro Shirai, Kenzo Hirao, Tomohiko Shibuya, Shuichi Okawa, Yuki Hasegawa, Yoshiaki Adachi, Kensuke Sekihara, and Shigenori Kawabata. Magnetocardiography using a magnetoresistive sensor array. *International heart journal*, 60(1):50–54, 2019.
- [SJWH⁺20] Tilmann Sander, Anna Jodko-Władzińska, Stefan Hartwig, Rüdiger Brühl, and Thomas Middelman. Optically pumped magnetometers enable a new level of biomagnetic measurements. *Advanced Optical Technologies*, 9(5):247–251, 2020.
- [SKD⁺20] Julius Schmalz, Anne Kittmann, Phillip Durdaut, Benjamin Spetzler, Franz Faupel, Michael Höft, Eckhard Quandt, and Martina Gerken. Multi-mode love-wave saw magnetic-field sensors. *Sensors (Basel, Switzerland)*, 20(12), 2020.
- [SSB91] G Suran, J Sztern, and B Barbara. Well-defined in-plane uniaxial anisotropy in amorphous codyzr films. *Applied physics letters*, 58(12):1338–1340, 1991.
- [SSL⁺15] V. Sindhuri, Dong-Hyeok Son, Dong-Gi Lee, SungHwan Sakong, Yoon-Ha Jeong, In-Tak Cho, Jong-Ho Lee, Yong-Tae Kim, Sorin Cristoloveanu, Youngho Bae, Ki-Sik Im, and Jung-Hee Lee. 1/f noise characteristics of AlGa_N/Ga_N finFETs with and without TMAH surface treatment. *Microelectronic Engineering*, 147:134–136, 2015.
- [SYH⁺22] Changxing Sun, Wenrong Yang, Yifan He, Cunzheng Dong, Lei Chen, Zhaoqiang Chu, Xianfeng Liang, Huaihao Chen, and Nian-Xiang Sun. Low-frequency magnetic field detection using magnetoelectric sensor with optimized metglas layers by frequency modulation. *IEEE Sensors Journal*, 22(5):4028–4035, 2022.

- [Tho17] L. Thormählen. *Abscheidung weichmagnetischer, magnetostriktiver Schichten auf Quarzsubstraten für die Magnetfeldsensorik*. Master's thesis, Kiel University, Kiel, 2017.
- [Tum11] Slawomir Tumanski. *Handbook of Magnetic Measurements*. CRC Press, Taylor & Francis Group, 6000 Broken Sound Parkway NW, Boca Raton, FL 33487-2742, 2011.
- [TVK⁺18] Andrei V. Turutin, João V. Vidal, Ilya V. Kubasov, Alexander M. Kislyuk, Mikhail D. Malinkovich, Yuriy N. Parkhomenko, Svetlana P. Kobeleva, Oleg V. Pakhomov, Andrei L. Kholkin, and Nikolai A. Sobolev. Magnetolectric metglas/bidomain $y + 140^\circ$ -cut lithium niobate composite for sensing ft magnetic fields. *Applied Physics Letters*, 112(26):262906, 2018.
- [UGR⁺20] Necdet Onur Urs, Elizaveta Golubeva, Volker Röbisch, Sebastian Toxvaerd, Shayan Deldar, Reinhard Knöchel, Michael Höft, Eckhard Quandt, Dirk Meyners, and Jeffrey McCord. Direct link between specific magnetic domain activities and magnetic noise in modulated magnetoelectric sensors. *Physical Review Applied*, 13(2), 2020.
- [VWMQ18] Dwight Viehland, Manfred Wuttig, Jeffrey McCord, and Eckhard Quandt. Magnetolectric magnetic field sensors. *MRS Bulletin*, 43(11):834–840, 2018.
- [WFGV79] D. Webb, D. Forester, A. Ganguly, and C. Vittoria. Applications of amorphous magnetic-layers in surface-acoustic-wave devices. *IEEE Transactions on Magnetics*, 15(6):1410–1415, 1979.
- [WJX⁺18] Wen Wang, Yana Jia, Xufeng Xue, Yong Liang, and Zhaofu Du. Magnetostrictive effect in micro-dotted FeCo film coated surface acoustic wave devices. *Smart Materials and Structures*, 27(10):105040, 2018.
- [WV65] R. M. White and F. W. Voltmer. Direct piezoelectric coupling to surface elastic waves. *Applied Physics Letters*, 7(12):314–316, 1965.
- [WXC⁺15] Wen Wang, Xiao Xie, Gui Chen, Jiuling Liu, and Shitang He. Temperature-compensated love wave based gas sensor on waveguide structure of $\text{SiO}_2/\text{36 yx LiTaO}_3$. *Smart Materials and Structures*, 24(6):065019, 2015.

- [YSH⁺16] E. Yarar, S. Salzer, V. Hrkac, A. Piorra, M. Höft, R. Knöchel, L. Kienle, and E. Quandt. Inverse bilayer magnetoelectric thin film sensor. *Applied Physics Letters*, 109(2):022901, 2016.
- [YSM⁺21] Mevlüt Yalaz, M. Sohail Noor, Cameron C. McIntyre, Markus Butz, Alfons Schnitzler, Günther Deuschl, and Michael Höft. DBS electrode localization and rotational orientation detection using SQUID-based magnetoencephalography. *Journal of neural engineering*, 18(2), 2021.
- [YTFI92] Narutoshi Yokokawa, Shin'ichi Tanaka, Toshitaka Fujii, and Mitsuteru Inoue. Love-type surface-acoustic waves propagating in amorphous iron-boron films with multilayer structure. *Journal of Applied Physics*, 72(2):360–366, 1992.
- [YTM⁺20] Mevlüt Yalaz, Alexander Teplyuk, Muthuraman Muthuraman, Günther Deuschl, and Michael Höft. The magnetic properties of electrical pulses delivered by deep-brain stimulation systems. *IEEE Transactions on Instrumentation and Measurement*, 69(7):4303–4313, 2020.
- [YXZ⁺12] Xueyong Yuan, Xiaobo Xue, Xiaona Zhang, Zheng Wen, Mao Yang, Jun Du, Di Wu, and Qingyu Xu. The exchange bias in polycrystalline bifeo₃/ni₈₁fe₁₉ bilayers on si substrate with lanio₃ buffer layer. *Solid state communications*, 152(4):241–243, 2012.
- [Zab19] Sebastian Zabel. *Vom ΔE -Effekt zum Sensorsystem*. PhD thesis, Christian-Albrechts-Universität zu Kiel, Kiel, 2019.
- [ZHFN20] Siming Zuo, Hadi Heidari, Dario Farina, and Kianoush Nazarpour. Miniaturized magnetic sensors for implantable magnetomyography. *Advanced Materials Technologies*, 5(6):2000185, 2020.
- [ZRD⁺02] C. Zimmermann, D. Rebiere, C. Dejous, J. Pistre, and R. Planade. Love-waves to improve chemical sensors sensitivity: theoretical and experimental comparison of acoustic modes. In *Proceedings of the 2002 IEEE international frequency control symposium & PDA exhibition*, pages 281–288. IEEE, 2002.

Acknowledgments

First of all, I would like to express my sincere gratitude towards Prof. Dr. Eckhard Quandt for giving me the opportunity to work on this exciting topic in his group and giving me the freedom to pursue my own ideas, while always steering me into the right direction when necessary. For co-supervising this thesis and always providing valuable input I thank Dr. Dirk Meyners.

It was a great pleasure for me to have spend the last 4 years at the chair for inorganic functional materials working with a group of kind and helpful people. I would have not went this path, if it were not for Dr. Patrick Hayes who opened the wide world of magnetoelectrics and magnetic field sensing to me and became an awesome friend along the way. For this I thank him a lot.

A lot of thanks go also to Dr. Patricia Pop-Ghe and Lars Bumke for sharing an office, lots of laughs, knowledge and more lifetime than we sometimes wished to.

Further, for providing a pleasant and fruitful working environment and many helpful discussions I thank Lars Thormählen, Dr. Anne Kittmann, Hanna Lewitz, Lea Jessen, Jascha Rohmer, Dr. Prasanth Velvaluri, Dr. Till Jurgeleit, Dr. Erdem Yarar, Dr. Christiane Zamponi, Justin Jetter, Maike Wegner, Dr. Christine Kirchhof, Lisa Hanke, Sabrina Curtis, Duygu Dengiz, Thomas Metzger, Marc Alexander Nowak and David Kunath.

Dr. Antonio Malavé I thank for his tireless efforts to keep the clean room running and our shared passion for filter coffee. Our group's secretaries Carola Block and Gislinde Schröder I thank for being the tamers of chaos.

For the unlimited hospitality and for teaching me about ion beam deposition I thank Prof. Dr. Susana Cardoso and here wonderful group at INESC-MN in Lisbon, Portugal. Prof. Dr. Jan Korvink and Dr. Mazin Jouada I thank for our short but interesting collaboration and for welcoming me at KIT.

This thesis was developed within the Sonderforschungsbereich 1261 wherein I had the privilege to work with many bright people from different scientific areas. From those my biggest gratitude goes towards Dr. Phillip Durdaut who developed and established all the readout electronics I used for measuring my sensors and from whom I learned a lot about the electrical engineering aspect of my work. Dr. Mevlüt Yalaz I thank for the collaboration on deep brain stimulation, from which I learned a lot about the real world requirements for magnetic field sensing.

For many valuable discussions on magnetism and performing MOKE imaging I thank Prof. Dr. Jeffrey McCord and his group members Cai Müller and Elizaveta Spetzler. My project partners from Fraunhofer ISIT Dr. Jingxiang Su, Jana Meyer and Dr. Fabian Lofink I thank for a fruitful collaboration.

Further thanks go to Prof. Dr. Andreas Bahr, Dr. Johannes Labrenz, Henrik Wolfram, Dr. Niklas Wolff, Dr. Julius Schmalz, Dr. Stefan Schröder, Huxi Wang and Johan Arbustini.

In the end, I thank my parents Rosa and Johann for being brave and leaving everything behind to enable me all these opportunities and my siblings Lena, Wowa, Natascha and Dennis for not knowing the first thing about science.